5-2019

The Role of Heterogeneous Constitutive Properties on Mechanical Behavior of Advanced High Strength Steel Spot Welds

Hassan Rezayat
University of Tennessee, hrezayat@vols.utk.edu

To the Graduate Council:

I am submitting herewith a dissertation written by Hassan Rezayat entitled "The Role of Heterogeneous Constitutive Properties on Mechanical Behavior of Advanced High Strength Steel Spot Welds." I have examined the final electronic copy of this dissertation for form and content and recommend that it be accepted in partial fulfillment of the requirements for the degree of Doctor of Philosophy, with a major in Mechanical Engineering.

Sudarsanam Suresh Babu, Major Professor

We have read this dissertation and recommend its acceptance:

Zhili Feng, Yangfei Gao, Timothy Truster

Accepted for the Council:

Dixie L. Thompson

Vice Provost and Dean of the Graduate School

(Original signatures are on file with official student records.)

The Role of Heterogeneous Constitutive Properties on Mechanical Behavior of Advanced High Strength Steel Spot Welds

A Dissertation Presented for the

Doctor of Philosophy

Degree

The University of Tennessee, Knoxville

Hassan Rezayat

May 2019

Dedication

This dissertation is dedicated to my beloved family who have always been a source of inspiration, encouragement, and comprehensive support.

Acknowledgements

I am grateful to my supervisor, mentor, and committee chair Prof. Sudarsanam Suresh Babu whose expertise, understanding, generous guidance, and support made it possible for me to work on this topic that was of great interest to me. It was a pleasure working with him.

I am truly thankful to ArcelorMittal Global R&D East Chicago for the financial support for this project. I would like to express my deepest gratitude to Dr. Hassan Ghassemi-Armaki, Dr. Sriram Sadagopan, and Dr. Shrikant Bhat from ArcelorMittal R&D East Chicago for their support. The mentorship and helpful discussions from Dr. Ghassemi-Armaki are much appreciated.

I would like to express my deepest appreciation to my PhD committee members Dr. Zhili Feng, Dr. Yanfei Gao, and Dr. Timothy Truster for their technical support and guidance throughout the preparation, review of dissertation document, and discussions in the proposal and the final dissertation defense sessions.

I would like to thank all of Dr. Babu's students in the Advanced Manufacturing and Materials Group (AMMG) at The University of Tennessee at Knoxville and Dr. Julian D. Escobar for the helpful discussions and collaborations across several projects including this work.

I am thankful to Dr. John Dunlap for the training on the scanning electron microscope and John Bohling for the help on setting up the Gleeble® thermo-physical simulator and helps in the welding laboratory.

Special thanks to Mrs. Anita Monroe, assistant to Dr. Babu, and the staffs in the Business Office of the Mechanical Engineering Department for their assistance on arranging the meetings, conference travels, and laboratory purchases relevant to this project.

Abstract

Recent publications have shown that the load bearing capability of resistance spot welds (RSW) made from dual-phase (DP) and martensitic (MS) Advanced High Strength Steels (AHSS) does not scale linearly with the tensile strength of their base metals. Although this degradation of welds strength has been linked by researchers to a phenomenon known as heat affected zone (HAZ) softening, the individual role of HAZ softening in different grades of AHSS has not yet fully understood. This work attempts to explain the above nonlinearity in spot welds performance by using a local to global approach to understand the role of HAZ softening on the strength of DP and MS spot welded samples. Material heterogeneity in Tension-Shear (TS) and Cross-Tension (CT) samples made from six grades of AHSS is studied by using microhardness measurements on spot welds and mechanical testing and digital image correlation (DIC) on thermally simulated samples in Gleeble machine. Results showed that the HAZ softening occurs in both subcritical and intercritical HAZ and the lowest yield stress exists in the ICHAZ making this region a candidate for plastic strain concentrating and failure initiation site.

Results from FE simulations showed that both the spot weld's nugget diameter and the HAZ softening play role in the performance of TS and CT samples. Nugget diameter showed to have a dominant effect on the strength of spot welds, and it is shown that the nonlinearity between the strength of spot welds and base metal tensile strength is related to the change in failure type in sample, as the nugget diameter increases. Results also showed that the HAZ softening have a complex and different role in performance of the welds. While it reduced the peak load and extension at peak load in DP spot welds, it played an opposite role and improved the same metrics in MS spot welds. The results also suggest that the lower strength (peak load) of MS spot welds compared to DP steels, is related to

the intrinsic brittle behavior of their base metal as the HAZ softening showed to increase the peak load in MS spot welds.

Table of Contents

1 Introduction....1

1.1 Background....1

1.2 Specific aims....2

1.3 Dissertation outline....4

2 Literature Review....5

3 Prediction of Local Elastic-Plastic Properties in AHSS Spot Welds Using Hardness Scaling Method....16

3.1 Introduction....16

3.2 Experimental Approach....17

3.3 Computational Approach....18

3.4 Results and Discussion....19

3.4.1 Softening extent in SCHAZ of spot welds....19

3.4.2 Effects of SCHAZ softening on Tension-Shear global response....22

3.5 Summary....26

4 Constitutive Properties and Plastic Instabilities in the Heat Affected Zones of Advanced High Strength Steel Spot Welds....27

4.1 Introduction....27

4.2 Experimental procedure....31

4.2.1 Materials....31

4.2.2 Spot welding equipment and parameters....31

4.2.3 Prediction of thermal cycles and Gleeble thermal simulations 33
4.2.4 Microstructural characterization and hardness measurements 35
4.2.5 Calibration of Gleeble thermal cycles using hardness values 35
4.2.6 Tensile testing and digital image correlation technique 37
4.3 Experimental results 38
4.3.1 Plastic flows 38
4.3.2 Results from Tension-Shear testing 38
4.3.3 Typical local microstructure of spot welds 38
4.3.4 Microhardness examination of spot welded samples 43
4.3.5 Comparison of YS, UTS and strain hardening exponent of Gleeble simulated HAZ samples 43
4.3.6 Observation of yield point phenomena 46
4.4 Discussion 46
4.4.1 Heterogeneous plastic flow properties 49
4.4.2 Spatial and Temporal Variations of Plastic instabilities 50
4.4.3 Overview of Microstructural Changes and Rationalization of Plastic Instabilities 52
4.5 Summary 59
5 Uncertainties in Finite Element Simulation of Yield Point Phenomena in Advanced High Strength Steel Spot Weld 60
5.1 Introduction 60
5.2 Simulation Methodology and Validation Experiments 62
5.2.1 Development of Local Constitutive Material Models 62

5.2.2 Finite Element Analysis 65
5.2.3 Overview of Validation Experiments 69
5.3 Results 69
5.3.1 Simulation Results for Uniaxial Tensile Testing 69
5.3.2 Simulation Results for Tension-Shear Test 70
5.4 Discussions 76
5.4.1 Oscillations in Global Loading Response 76
5.4.2 Uncertainties in FE Simulations of YPP 77
5.5 Summary 82
6 The Individual Role of Weld Geometry and HAZ Softening on Mechanical Performance of AHSS Spot Welds 84
6.1 Introduction 84
6.2 Experimental procedure 86
6.2.1 Materials 86
6.2.2 Local constitutive properties and damage model 86
6.2.3 Overview of Validation Experiments 89
6.3 Finite element simulations 89
6.4 Results 90
6.5 Discussion 95
6.5.1 Plastic strain evolution and failure path 95
6.5.2 The role of HAZ softening on spot welds performance 99
6.5.3 Uncertainties in FE simulation of AHSS Spot Welds 103

6.6 Summary 109

7 Conclusions and Recommendations for Future Work 111

7.1 Conclusions 111

7.2 Recommendations for Future Work 115

Bibliography 117

Vita 127

List of Tables

Table 4-1: Chemical composition, martensite fraction, and phase transformation temperature of the investigated steels. 32

Table 4-2: Tensile properties and hardness of the as-received AHSS used in this study. 32

Table 6-1: Chemical composition, martensite fraction, and phase transformation temperature of the investigated steels. 86

Table 6-2: As-received tensile properties for the AHSS used in this study. 87

Table 6-3: Equivalent plastic strain at failure for different regions of the spot welds made from three AHSS steels obtained from the uniaxial tensile testing. 87

Table 6-4: Material assignment to different regions of the spot weld for studying the role of HAZ softening on spot weld performance. 100

List of Figures

Figure 1-1: A comparison between the mechanical properties of several grades of Advanced Hight Strength Steels [6]. 3

Figure 1-2: Summary of the results from Tension-Shear (left) and Cross-Tension (right) tests as a function of base metal strength performed on DP and MS AHSS with nugget diameters in range of 6 to 9 mm [5]. 3

Figure 2-1: Schematic showing the typical thermal cycles used in manufacturing of DP and MS AHSS. 5

Figure 2-2: (a) Effect of carbon content on the tensile strength of martensite for steels that were super-critically annealed and quenched by water, and (b) tensile strength of DP steels as a function of martensite fraction [16]. 6

Figure 2- 3: Typical engineering stress vs. strain curves of different grades of DP steels [17]. The martensite volume fraction increases in higher grades from DP590 to DP780 and DP980. 7

Figure 2-4: A schematic diagram of the various regions of the heat affected zone and equilibrium phase transformation temperatures for a 0.15 wt.% carbon steel [89]. 8

Figure 2-5: Micrographs from scanning electron microscopy showing decomposed martensite in the SCHAZ of a DP AHSS. A combination of ferrite and tempered martensite in (a) and magnified view of tempered martensite island with carbide precipitates on a ferrite matrix in (b) from the work by Saha et al. [30]. 10

Figure 2-6: Integrated process modeling framework for predicting load response function of spot welds [43]. 13

Figure 2-7: Hardness measurements for DP590 and local hardness ratios were used to scale the base metal stress-strain curves in work by Yang et al. [43]. The HAZ softening was not observed in the DP590 steel. 14

Figure 2-8: Spot weld cross section and potential failure zones for Tension-Shear and Cross-Tension samples. Adopted from the work by Dancette et al. [40]. 15

Figure 3-1: Hardness values in three regions of spot weld for steels used in this study (a), Correlation between hardness drop and MVF and carbon content (b). 20

Figure 3-2: Hardness map, partitioned HAZ with local hardness ratio plot, and mesh design shown on the cross section of DP9650 (a and b) and M1700 (c and d) Tension-Shear samples. 21

Figure 3-3: Results from FE simulation and experiments for DP590, DP980LC, and M1700 ND of 6 mm (a) and M1700 with ND of 6 and 8 mm (b). 24

Figure 3-4: Equivalent plastic strain as a function of applied load at the notch tip and SCHAZ of M1700 Tension-Shear sample with nugget diameters of 6 and 8 mm. 25

Figure 3-5: In-plane shear stress at the center of nugget on the cross section of M1700 Tensile-Shear samples with nugget diameters of 6 and 8 mm as a function of global extension. 25

Figure 4-1: Comparison of measured Tension-Shear performance from spot welds made with DP and martensitic AHSS has shown a nonlinear relationship between the spot weld strength and base metal strength. 30

Figure 4-2: Dimensions for the samples used in Gleeble simulations with the outline for the sample used in tensile testing. Tensile sample dimensions are according to ASTM E8 sub-size standard specimen. 34

Figure 4-3: Overview of the programmed and measured thermal cycles used for simulating different regions of heat affected zone in Gleeble® thermo-mechanical simulator. The dashed lines show the programmed thermal cycles and the solid lines show the measured ones from thermocouples. Note that we are not able to achieve rapid cooling rate in the experimental sample due to inherent thermal mass in the system. 34

Figure 4-4: Comparison between hardness values from Gleeble thermal simulation for 650 °C peak temperature (as an instance) and softest region of HAZ in all the steels show only slight differences that are within the uncertainty of indenter locations (±200 μm) and hardness measurements (±10 HV). 36

Figure 4-5: Measured hardness distribution in M1700 sample subjected to thermal simulation with 350°C and 650 °C peak temperature along two different directions confirm the validity of our approach to use Gleeble samples as a surrogate to extract constitutive properties of HAZ regions. ..36

Figure 4-6: Engineering stress-strain curves obtained from tensile testing of base metal and Gleeble simulated HAZ samples for all six grades of DP and martensitic AHSS used in this study.....39

Figure 4-7: (a) Global deformation behaviors and failure in DP590 and M1700 Tension-Shear samples. Different extents of nugget rotation and global deformation can be observed (a). Localized plastic deformation in M1700 steels are marked in locations and are shown in high-magnifications (b) and (c). Failures in both steels are correlated to regions with peak temperature below Ae3 based on comparing the location of failures with predicted thermal distributions from the FE simulations and hardness measurements and are schematically illustrated in (d). 40

Figure 4-8: Overview of microstructural heterogeneity within the spot welded sample made from M1700 AHSS steel obtained using scanning electron microscopy. The annotations are explained as following: M-Martensite; F-Ferrite; and TM-Tempered Martensite. Note that the identification of carbides is based on the contrast observed in the SEM images. 41

Figure 4-9: Hardness ratios along the diagonal line across spot welds showing the hardness heterogeneity. Results show softening in SCHAZ and ICHAZ regions and hardening in UCHAZ and nugget. The base metal hardness for each steel is measured as: DP590: 199, DP980LC: 324, DP980MC: 311, M1300: 452, and M1700: 585 Vickers. Dash lines show the approximate boundaries between regions of the spot welds. 45

Figure 4-10: Variation of yield stress and ultimate tensile stress as a function of peak temperature obtained from Gleeble thermally simulated HAZ samples. 47

Figure 4-11: Variation of strain hardening exponent as a function of peak temperature obtained from Gleeble thermally simulated samples. 47

Figure 4-12: Schematic representation of stress-strain curve for material with discontinuous yielding (a) and DIC images from Lüders band initiation and propagation in the gauge length and strain along the path in the loading direction for DP1180 Gleeble simulated HAZ sample tempered to 650 °C (b). 48

Figure 4-13: Plastic flow heterogeneity in HAZ of AHSS spot welds based on results from tensile testing on thermally simulated samples. This heterogeneity increases in higher grades of these steels. 51

Figure 4-14: Lüders strain measured from Gleeble simulated SCHAZ samples. In all steels Lüders strain in SCHAZ increased with the thermal cycle peak temperature. 53

Figure 4-15: Lüders strain as a function of martensite carbon content and peak temperature in SCHAZ. Lüders strain showed an inverse correlation with martensite carbon content and increased with thermal cycle peak temperature. 53

Figure 4-16: Contour of localized strain trajectories for DP590, DP980LC, and M1700 samples, subjected to thermal cycles with a peak temperature of 650 °C, at strain of 0.01 and as a function of time. The Lüders band motion and numbers of initiation sites increase from DP590 to M1700. The rapid motion, multiple Lüders band initiation sites, and cross-width band motion are remarkably higher in M1700. Frames correspond to time intervals of 0.1 second. 56

Figure 4-17: Schematic illustration of microstructural evolutions occurring during thermal cycles of spot welding of DP AHSS steels with peak temperatures of 650 and 760 °C, corresponding to SCHAZ and ICHAZ, respectively. For the fully martensitic steels, events in martensite phase can be adopted and therefore, no separate schematics are needed. 56

Figure 4-18: The amount of carbon that can dissolve in ferrite in equilibrium as a function of peak temperatures. Carbon solubility in ferrite increases with an increase in peak temperatures. Slight reduction above a maximum value at high temperatures above 700°C is indeed expected due to the on-set of the austenite formation. 57

Figure 4-19: Variation of dislocation density based on fitting a phenomenological model proposed by Hahn [92]. In this model: $\boldsymbol{\sigma}$ is the plastic stress, $\boldsymbol{q}$ is the macroscopic work hardening coefficient, $\boldsymbol{\tau o}$ is the resolved shear stress, $\boldsymbol{b}$ is the burger's vector, $\boldsymbol{\varepsilon}$ is the strain rate, $\boldsymbol{\rho o}$ is the initial mobile dislocation density, $\boldsymbol{f}$ is the fraction of initially mobile dislocations, $\boldsymbol{\varepsilon p}$ is the plastic

strain, and a, C and n are dislocation density parameters from experiments. A wide range of mobile dislocation density was used in the fittings. 58

Figure 5-1: Local elastic-plastic properties obtained from thermally simulated samples representing the local properties of M1700 spot weld used in FE simulation of uniaxial tensile testing and TS and CT tests. 63

Figure 5-2: Three element-scale material models including NYPP, CYPP, and EYPP for M1700 at 500 °C (and 650 °C peak temperatures obtained from the method introduced by Schwab and Ruff [99]. Material models for CYPP and EYPP were calculated based on observed YS and variation of the Lüders angle in gauge length of UT sample. 64

Figure 5-3: Three-dimensional FE models prepared in Abaqus for uniaxial tensile (a) and Tension-Shear (b) samples. The TS sample was partitioned into sections representing different regions of the spot welded sample. A closer look at partitioning, mesh, and material assignment can be seen in Figure 5-4.....66

Figure 5-4: Image from optical microscopy of cross-section of M1700 spot weld. A 2% Nital etchant was used to reveal the microstructure. Results from hardness mapping are also shown in addition to FE model partitioned for material assignment. 67

Figure 5-5: Results from the FE simulation of uniaxial tensile testing was used to calibrate the material models with YPP for peak temperatures of 500 and 650°C. Results shown for 650 °C uniaxial tensile sample. 71

Figure 5-6: Results from FE simulation of TS sample with 8 mm nugget diameter for material models including: NYPP, CYPP, and EYPP. For CYPP FE simulations with and without a Tensile Failure criterion were performed. 72

Figure 5-7: Evolution of equivalent plastic strain in TS sample: (a) initiation of plastic strain and instability from ICHAZ, (b) strain hardening initiation in the

same region, (c) growth of plastic strain and instabilities into SCHAZ, (d) crack initiation in ICHAZ, (e) crack propagation in through the sheet thickness in ICHA, and (f) failure of TS sample from ICHAZ. The deformation scale is set to zero in above figures. 74

Figure 5-8: Heterogeneous stress distribution in the HAZ of TS sample obtained from FE simulations show the oscillation and alteration of stress in SCHAZ region of the weld. Three material models for SCHAZ were used in FE simulations.....75

Figure 5-9: Results from FE simulations and experiments for TS sample with 4 mm nugget diameter show that the use of tensile failure criteria can lead into incorrect results. The failure mode from experiments and FE simulations with only strain-based damage model resulted in FIF failure (b and c) while the FE model with TFC resulted in PF-ICHAZ failure (a).....78

Figure 5-10: Results from FE simulations and experiments for TS sample with 8 mm nugget diameter also show that the use of TFC can lead into incorrect results. Although the failure mode is similarly occurring in ICHAZ, however, the local and global deformations are significantly different. The model without TFC, shows results similar to those from experiments with comparable necking and local deformations, as shown in (a, b, d, e, and f). 79

Figure 5-11: The initiation and growth of equivalent stress from front side to the other side of the spot weld. The element size in loading direction changes from 0.03 to 0.2 μm affecting the deformation behavior observed at peak load in deformation curves from FE simulations.....79

Figure 5-12: Uncertainties in the study of yield point phenomena and its effects in deformation behavior of welded samples. 81

Figure 5-13: Mesh sensitivity analysis revealed the effect of element size on the oscillations observed in loading response. Results are presented for TS FE model with EYPP material input. 81

Figure 6-1: Engineering stress-strain curves obtained from tensile tests performed on base metal and Gleeble thermally simulated HAZ samples made from the three DP and MS AHSS used in this study. 88

Figure 6-2: Finite element models for TS and CT samples with partitioned HAZ, material assignment, and mesh design. Due to the symmetrical geometry and for the sake of computational time.....91

Figure 6-3: HAZ was partitioned into several regions based on the number of the tempering peak temperatures used in Gleeble thermal simulations. Results from hardness mapping are shown in addition to the mesh design and typical failure modes in AHSS spot welds. 91

Figure 6-4: Results from experiments and FE simulations for DP590, DP980LC, and M1700 TS samples with 4, 6, and 8 mm nugget diameters. Failure modes are also shown in the legend of each plot. 92

Figure 6-5: Experimental results from TS (a and b) and CT (c and d) samples made from DP590, DP980LC, and M1700 with three nugget diameters of 4, 6, and 8 mm. The initial martensite volume fraction for these steels are 16, 59, and 100 percent, respectively. Failure mode for each sample is also shown. 94

Figure 6-6: Results from FE simulation of TS test for M1700 spot welds with 4, 6, and 8 mm nugget diameters. The evolution and localization of the equivalent plastic strain on the cross section of samples show M1700 TS samples. Three failure modes were observed: FIF for ND=4 mm, RB-FGHAZ for ND=6 mm, and RB-ICHAZ for ND=8 mm. The main competition was

observed between the ICHAZ and FGHAZ based on the strain localization, crack initiation, propagation, and failure. 96

Figure 6-7: Equivalent plastic strain evolution in different regions of TS samples made from with 4, 6, and 8 mm nugget diameters. Note that in each plot, only one region reaches the failure plastic strain and failure and other curves never reach their failure strain levels. 97

Figure 6-8: Results from the FE simulations of M1700 CT sample with 4, 6, and 8 mm nugget dimeters showing the evolution of the PEEQ in different regions of the HAZ on the cross section of CT sample. 98

Figure 6-9: The change in the TSS and CTS when the SCHAZ and/or ICHAZ were not included in the FE simulations. Results show that exclusion of only ICHAZ has minimal impact on both TSS and CTS while the exclusion of either or both SCHAZ and ICHAZ can have up to 15.5% change (increase) in TSS and CTS. 101

Figure 6-10: The effect on HAZ softening on TS and CT strength and extension for DP980LC and M1700 steels showed that the role of HAZ softening is complex and different in different grades of AHSS. While it deteriorates the performance of DP980LC spot welds it improves the performance of M1700 ones. 102

Figure 6-11: Equivalent plastic strain localization, crack initiation, and path on the cross section of CT sample made from DP980LC in (a) and (b), and M1700 in (c) and (d), with and without HAZ softening obtained from FE simulations. In DP980LC HAZ softening resulted in premature failure and in M1700 improved the weld strength. Local and global deformations and failure type and mechanisms were affected by existence of HAZ softening in this sample. 104

Figure 6-12: The complex role of HAZ softening on the strength of Tension-Shear samples made from DP and MS AHSS. While HAZ softening plays a strong role in strength of DP steels and can significantly reduce welds strength, for example by 44% in DP980LC sample, depending on the martensite volume fraction in initial microstructure, it has a minor role in strength of MS steels and improves welds strength by 16% in M1700 TS sample, as an example. 105

Figure 6-13: Difference between the peak loads measured from experiments and FE simulations for TS and CT samples with 4, 6, and 8 mm nugget diameter. The difference increases from DP590 to DP980LC and M1700 as the material heterogeneity and nugget diameter increase. 106

Figure 6-14: Results from scanning electron microscopy revealed pre-existence of micro-cracks and voids at the notch tip and on faying surface of the spot welds (a). FE model with and without crack at faying surface for M1700 CT with 4 mm nugget diameter (b). 108

Figure 6-15: Results from FE simulation of M1700 CT sample with nugget diameter of 4 mm for the sample with and without micro-crack at the notch tip. Including the micro-crack to model resulted into 28% and 43% decrease in PL and PLE (a). This also affected the crack path to regions closer to the nugget for the sample with micro-crack (b). 108

1 Introduction

1.1 Background

Advanced High Strength Steels (AHSS) are a new generation of high-strength steels produced with carefully selected chemical composition and precisely controlled heating and cooling process parameters. Their typical tensile strength ranges from 550 MPa and exceeds 2000 MPa in their third generation. Having a complex microstructure, they achieve a combination of strength, ductility, formability, and fatigue properties making them suitable for applications in automotive and transportation industries to improve the fuel economy, safety, and, and performance of the cars, while reducing the emission [1, 2].

Based on the final microstructure and thermomechanical processing AHSS are divided into several grades; Dual-Phase (DP), Complex-Phase (CP), Transformation-Induced Plasticity (TRIP), Ferritic-Bainitic (FB), and Martensitic (MS) are of the most widely used members of AHSS family. Figure 1-1: A comparison between the mechanical properties of several grades of Advanced Hight Strength Steels [6]. compares different type of AHSS by their elongation and tensile strength.

The automotive industry has been interested to apply these new AHSS steels in the modern designs and adopted the Resistance Spot Welding (RSW) as the predominant technique for joining the steel sheets. Since these steels are relatively new to the automotive industry and new generations of AHSS grades are emerging to the users, appropriate welding techniques, parameters, and standards need to be provided. The behavior of these and emerging steels during the spot welding and final mechanical properties need to be fully investigated and necessary information regarding specific manufacturing techniques leading to quality joint need to be provided to the industrial users.

The users of these steels also have experienced a phenomenon known as the HAZ softening that occur during resistance spot welding process. This phenomenon is ascribed to the effects of the thermal cycles experienced by the local material in spot welds during welding, causing the welds to show TS and CT strength below the expected strength. The magnitude of this strength reduction is tentatively attributed to the magnitude of the HAZ softening [3-5].

Results from the spot welds made from DP and MS AHSS with base metal tensile strengths in range of 300 to 1800 MPa demonstrated in Figure 1-2 show that there is a nonlinear relationship between TS and CT strength with the base metal tensile strength [5]. As this figure shows, this nonlinearity happens for those steels that have base metal tensile strengths above 1000 MPa. Therefore, the objective of this study is to rationalize the deformation behavior and failure of above steels with a focus on the nonlinearity in performance of the spot welds shown as shown in Figure 1-2 by means of experimental and computational techniques.

1.2 Specific aims

This dissertation aims to address the following scientific questions, which will eventually provide fundamental knowledge in the field of deformation behavior of AHSS spot welds used in parts made for industrial applications especially automotive industry where spot welding is the main technique to join body and chassis parts together:

- To reveal the effect of thermal cycles due to RSW process on local microstructure and mechanical properties in different regions of HAZ
- To investigate the softening and hardening extents in the HAZ of DP and MS steels and find their correlation to the steels initial microstructure and chemical composition

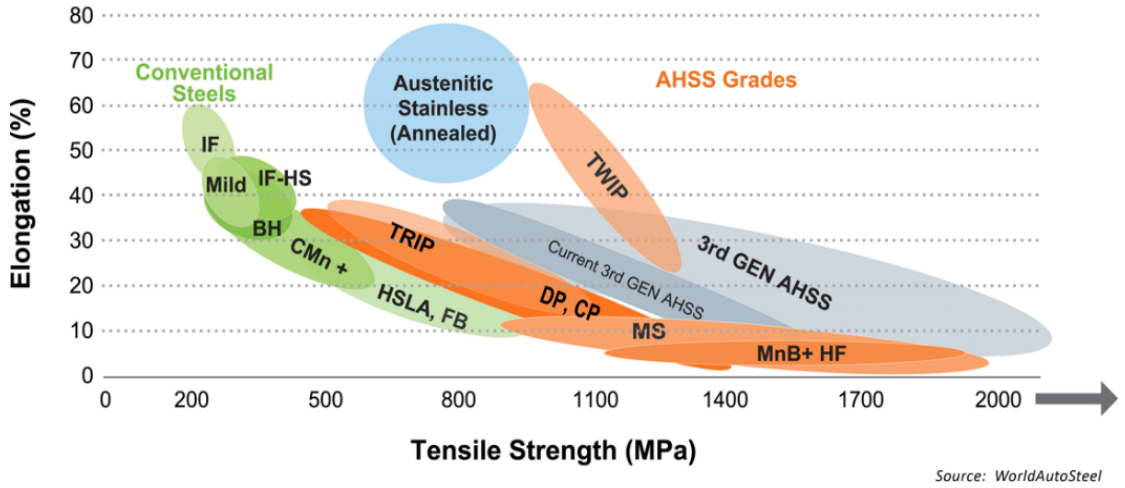

Figure 1-1: A comparison between the mechanical properties of several grades of Advanced Hight Strength Steels [6].

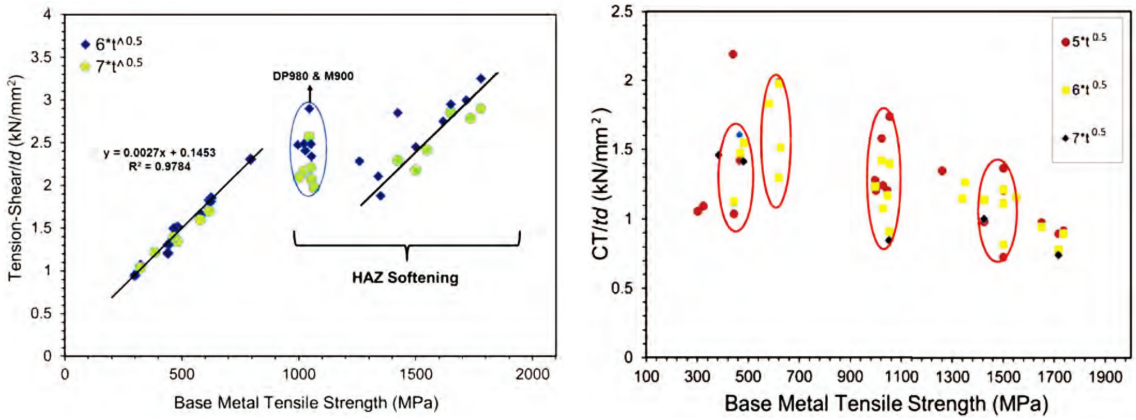

Figure 1-2: Summary of the results from Tension-Shear (left) and Cross-Tension (right) tests as a function of base metal strength performed on DP and MS AHSS with nugget diameters in range of 6 to 9 mm [5].

- To investigate if the softening in AHSS related to the martensite tempering in the SCHAZ or the formation of ferrite from reheated martensite in ICHAZ
- To reveal the influence of softening and hardening phenomena on the mechanical performance of AHSS spot welds based on the chemistry and initial microstructure, and welding parameters.
- To provide an computational model that integrates the material model and weld geometry and predicts the deformation behavior and failure for AHSS TS and CT samples and explains the nonlinearity seen in Figure 1-2.

1.3 Dissertation outline

The content of this dissertation has been divided into seven chapters as follows. In Chapter 1 a brief introduction to the background, problem statement, and aims of the research work are presented. Chapter 2 includes a literature review followed by Chapter 3 that presents the results from FE simulation of TS samples with material properties obtained from hardness scaling method. Chapter 4 includes the results from the microstructural and mechanical evaluations of the Gleeble thermally simulated HAZ samples and discusses the constitutive properties and plastic instabilities in the HAZ of AHSS spot welds. The effects of discontinuous yielding in form of yield point phenomena are investigated in Chapter 5 by using experimental methods and FE simulations. Chapter 6 presents the results from FE simulations and experiments on TS and CT samples and investigates the role of geometry of the spot weld and heterogeneous constitutive properties in the HAZ on the deformation behavior and failure of AHSS spot welds. The underlying reasons for the nonlinearity in the strength of the AHSS spot welds are also explains in this chapter. Finally, the general conclusions and recommendations for the future work are brought in Chapter 7.

2 Literature Review

As the application of Advanced High Strength Steel (AHSS) is thriving in the automotive industry, resistance spot welding of these steel sheets becomes highly significant since the number of applications of these steels is increasing in auto body structure with replacing those made with conventional and mild steels [2, 7, 8]. Several grades of AHSS are being developed with different phases included depending on the application and required performance. Among various grades of AHSS, the DP and MS AHSS that include ferritic and martensitic micro-constituents in their microstructure are widely used in the automotive industry. The main process for manufacturing these steels is the continuous annealing process followed by a cold rolling step, as shown schematically in Figure 2-1. The amount of martensite in the final microstructure of these steels is controlled by controlling the peak temperature and holding time at this

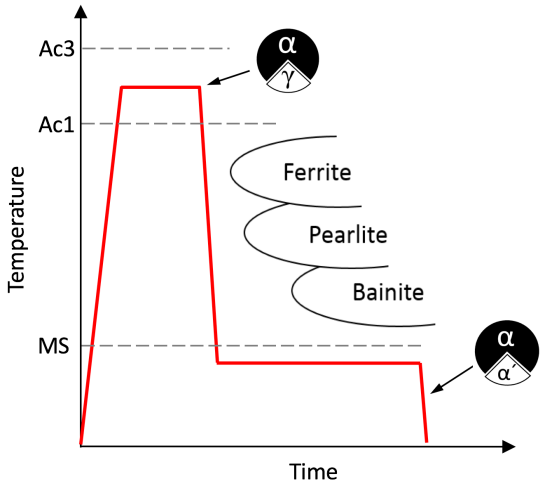

Figure 2-1: Schematic showing the typical thermal cycles used in manufacturing of DP and MS AHSS.

temperature to transforms a desired volume fraction of initial ferrite into austenite that will be transformed to martensite upon quenching to room temperature. For a fully martensitic steel, the entire ferrite is usually transformed to austenite and then quenched to room temperature.

Several studies have shown that the mechanical properties of the final product from above process strongly depends on the volume fraction of the martensite and its strength [9-14]. While ferrite is the soft and ductile phase with hardness values around 90 HV, martensite acts as the secondary hardening phase with hardness value as high as 700 HV and tensile strength as high as 2600 MPa for high carbon (around 0.8 wt. %) martensite. The strength and hardness of martensite strongly relies on its carbon content as shown by several researchers [10, 11] . Therefore, a good combination of these two micro-constituents can results in a good combination of ductility and strength for specific application [15]. Figure 2-2 (a) and (b) show the effect of carbon content on the strength of the

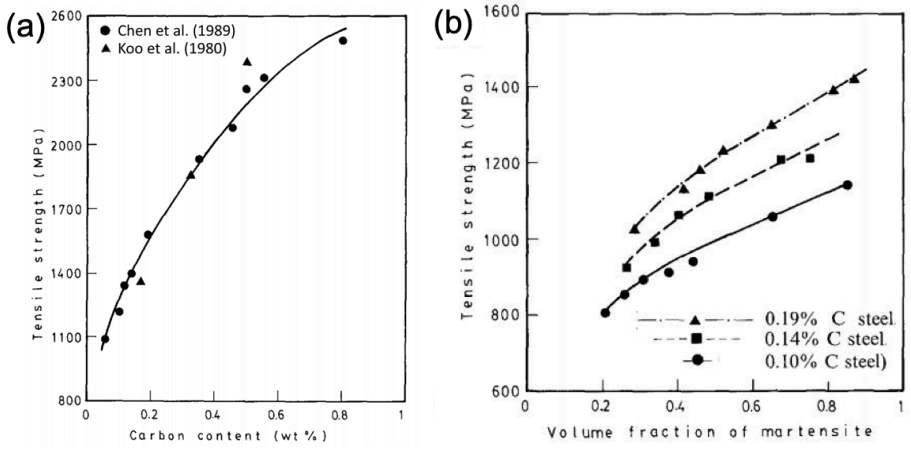

Figure 2-2: (a) Effect of carbon content on the tensile strength of martensite for steels that were super-critically annealed and quenched by water, and (b) tensile strength of DP steels as a function of martensite fraction [16].

martensite and the effect of martensite volume fraction of the tensile strength of the DP AHSS, respectively. Figure 2- 3 shows several grades of DP AHSS with their mechanical properties including the tensile strength and elongation.

While AHSS possess a good combination of strength and ductility due to their complex microstructure, the existence of metastable micro-constituents (here martensite) can make them sensitive to the thermal gradients that can be experience by steel during manufacturing processes such as the resistance spot welding process. This can result in metallurgical changes and degradation in mechanical properties as reported in several studies [3, 4, 13, 16-19]. For several grades of AHSS, a phenomenon known as HAZ softening has been reported by many researchers [3, 4, 9, 12, 13, 20, 21]. To investigate the softening kinetics occurring in heat affected zone of DP spot welds, Biro et al. [12] measured the heat input due to welding by using the methodology introduced by Xia et al. [18] in which the distance from the weld centerline to the fusion zone and inter-critical

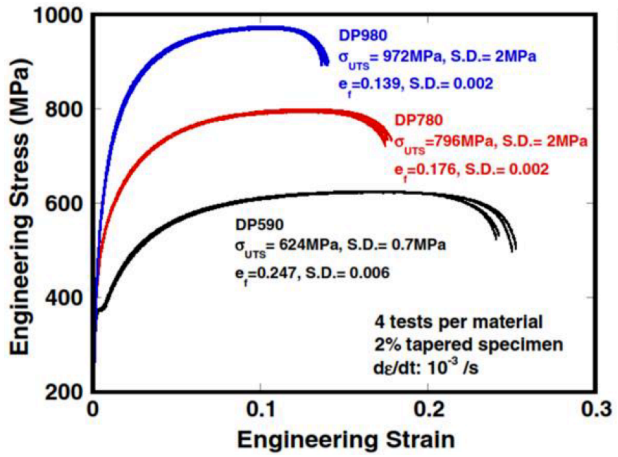

Figure 2- 3: Typical engineering stress vs. strain curves of different grades of DP steels [17]. The martensite volume fraction increases in higher grades from DP590 to DP780 and DP980.

HAZ for DP600 and DP780 were used in Rosenthal's two-dimensional equation. Their work revealed that during the welding, martensite in base metal decomposes into cementite and ferrite resulting in a reduction in the hardness of the HAZ in the subcritical HAZ. Their results did not show the formation of epsilon carbides which is consistent with the work done by Wang et al. [22]. They also described martensite decomposition ratio by using the Avrami equation from the hardness values measured on weld and base metal. Figure 2-4 shows a schematic of different regions of the HAZ and the equilibrium phase transformation temperatures for a steel with 0.15 wt.% carbon. In all the studies by several researchers the HAZ softening has been shown to occur in the SCHAZ of the steel where the experienced peak temperature is below the Ae1 phase transformation temperature and softening is not reported in other regions. In another effort, Biro et al. [23] investigated the transient HAZ softening in their investigations in spot welds made from dual phase and martensitic AHSS. They

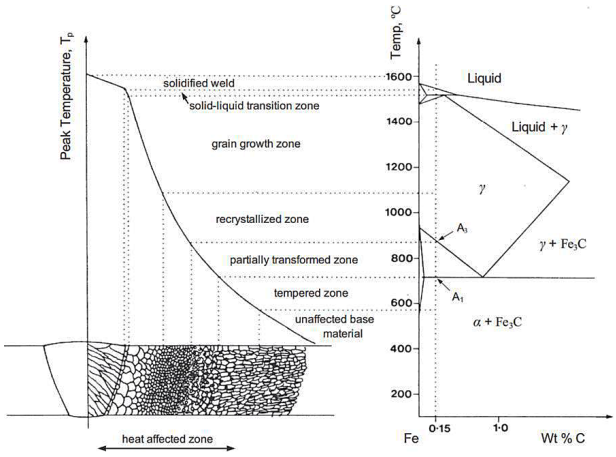

Figure 2-4: A schematic diagram of the various regions of the heat affected zone and equilibrium phase transformation temperatures for a 0.15 wt.% carbon steel [89].

suggested a technique to measure the softening kinetics of above steels by using rapid isothermal tempering by using Johnson-Mehl-Avrami-Kolmogorov (JMAK) equation to calculate the fraction of the completed softening reaction concerning the time of transformation. In their work and other similar ones [12-14] it was shown that the tempering temperature has a reverse relationship with the magnitude of hardness in SCHAZ. Xia et al. [18] used laser welding to study the effects of heat input and martensite on softening of HAZ in dual phase steel sheets. They normalized the heat input by using Rosenthal's equation and found that the extent of HAZ softening is a function of martensite content and heat input. It was shown that the minimum hardness in the HAZ reduces as the tempering time increases meaning a higher portion of martensite decompose into cementite and ferrite. Figure 2-5 shows micrographs obtained from the scanning electron microscopy for a tempered martensite with carbide precipitates in a ferritic matric. The effect of base metal martensite content on HAZ softening has been investigated by researchers like Xia et al. [18] who showed that in laser welding of three dual sheets of steel with the same welding parameters, softening increased with increasing base metal ultimate tensile strength. His team also showed that there is a linear relationship between magnitudes of the HAZ softening and martensite volume fraction in base metal, and therefore concluded that the correlation between softening and base metal tensile strength is indeed due to the linear increase of tensile strength and also the martensite volume fraction [18, 24].

The extraction of local mechanical properties by using sharp instrumentation techniques has been also studied using nanoindentation technique [13]. The grain-scale hardness and elastic modulus were measured using this technique and results on DP spot welds showed that the softening in HAZ is related to the martensite islands, and ferrite phase hardness does not change [13]. Since HAZ softening occurs due to the thermal gradients generated by welding thermal

cycles, many studies were performed to understand the mechanism of this martensite tempering [12, 14, 18, 25, 26] and it was found that martensite tempering is a diffusion driven process [26, 27] and hence its progress strongly depends on the tempering time and temperature. It has been reported [28] that the maximum softening occurs in the region close to the isotherm line, Ae1, with the temperature at the highest point but not in austenitization region and thus without any transformation into austenite, martensite tempered and decompose into other microstructure. The effects of cooling rate of martensite tempering kinetics as also been studied [29] and it has been shown that the higher peak temperature in spot welds corresponds to lower cooling rate, higher tempering time, and higher magnitude of softening, and vice versa. Looking into the literature provides three methods used by researchers to model the microstructure and mechanical property evolutions during the tempering process. Christian et al. [31] modeled the nucleation and growth of carbides emerging

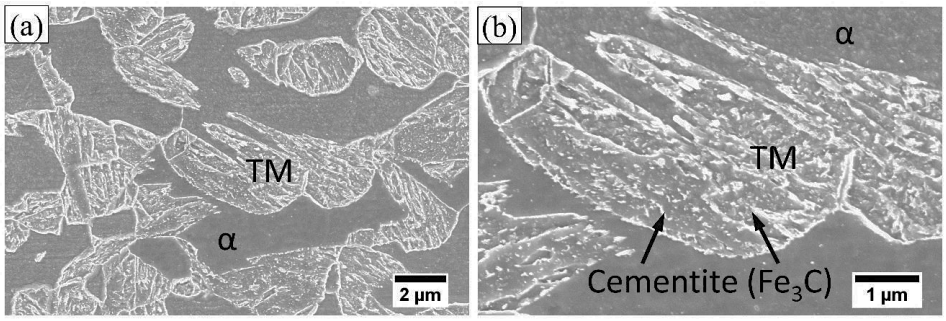

Figure 2-5: Micrographs from scanning electron microscopy showing decomposed martensite in the SCHAZ of a DP AHSS. A combination of ferrite and tempered martensite in (a) and magnified view of tempered martensite island with carbide precipitates on a ferrite matrix in (b) from the work by Saha et al. [30].

from the tempering. Grange et al. [10] used the mechanical properties of welded joints to model the tempering by curve fitting the resultant changes. The other approach was a semi-empirical approach discussed in [16] to predict the HAZ softening in carbon steels by uniting tempering time and temperature into a single tempering parameter and plotting it versus hardness of tempered material. However, the most widely used approach was developed independently by Johnson and Mehl, Avrami, and Kolmogorov [32-34] who generate a time-dependent equation, called JMAK equation, relating volume fraction of daughter phase from its parents in a nucleation and growth process. They proposed that there are three distinct steps during the phase transformations and proposed an equation that describes the kinetics of phase transformations. This equation is used by many researchers to depict the advancement of tempering process [9, 35-37]. From mentioned approaches, Biro et al. [16] proposed that the JMAK equation may be used with some modifications for modeling the tempering phenomena and to be used in Integrated Computational Material Engineering (ICME) models for prediction of AHSS spot welds performance. Tomita studied the effect of second phase martensite morphology (shape, size, and distribution) on the tensile strength by using different heat treatments on dual-phase steels [15]. His results show that the peak temperature, holding time, and cooling rate can influence the morphology of the martensite leading to the different amount of tensile strength and ductility for material. His results from fractography by SEM also depict that the ductility of these steels can vary with microcrack initiation in ferrite or martensite sites. The mechanism of secondary hardening in the tempering of dual phase steels was studied by Saha et al. [30] who performed rapid isothermal tempering of DP780 with ferritic-martensitic-bainitic microstructure using the Gleeble thermomechanical simulator. Laser welding was used in his study to generate a non-isothermal tempering on steels. The importance of time and temperature were explicitly explained in their work. Mechanical properties and fracture of spot welds made from AHSS have been

also studied by many researchers. Numerical and computational tools were used to analyze the failure mechanisms and modes of spot welds during Tension-Shear and Cross-Tension mechanical tests. Chao et al. [38, 39] formulated the stress distribution around weld nugget and showed that the failure load is proportional to the thickness of the steel sheet and the weld nugget diameter. By running tensile tests, he concluded that the failure mechanism of the Tension-Shear sample at the material level is tensile while for cross tension test is a shear fracture. Khan et al. [20] investigated the mechanical properties and microstructure of AHSS spot welds and developed a relationship between chemistry and fusion zone hardness. They showed that fusion zone has a fully martensitic microstructure with the highest hardness compared with other regions of the weld. Their work showed that fusion zone hardness increased as the carbon equivalent of base metal increases and stated that alloying elements could affect the formation of martensite by retarding the kinetics of ferrite and bainite formation. Dancette et al. [40, 41] investigated the damage in AHSS spot welds by using a coupled micro tomography, metallography and fractography and identified the main failure mechanisms as strain localization in base metal or heat affected zone, ductile shear around the weld, and semi-brittle fracture in the weld nugget. They also developed a finite element model to show how the failure mechanisms are leading to macroscopic failure types in the weld. In another work [42] the same method was used for homogeneous and heterogeneous configurations for weld regions of the TRIP780 spot weld, and the crack initiation and propagation up to the failure of the weld were predicted as a function of the geometrical features of the weld. Resistance spot welding in an electrical-thermal-mechanical-metallurgical process and combining all these physics in a single integrated computational model is a significant challenge. Many efforts have been done to develop an ICME model to predict the mechanical properties of the part made with spot welding. For example Yang et al. [43] developed an integrated computational model to predict the load response function of spot weld

under static and dynamic loading for DP590 steel. In their integrated model, making a spot weld was divided into three steps, and a model was developed for each one. The framework of their integrated model can be seen in Figure 2-6. in this model, experiments provide microstructure properties and the validation of the integrated model. Spot welding parameters, geometry, and material for steel sheets are inputs into the spot weld process model. The outputs are the residual stresses and effective plastic strains in the weld. These data in addition to the microstructure properties from experiments then were mapped into the local mechanical model. In the local mechanical model, the weld is constructed from three different regions including base metal, heat affected zone, and fusion zone or nugget. For each region, material properties were given based on their hardness converted to tensile strength. It was also suggested that these data could be alternatively derived from the Gleeble thermomechanical simulation for each region; however, the hardness conversion method was selected as a simplified approach. Tension-Shear and Cross-Tension models then generated

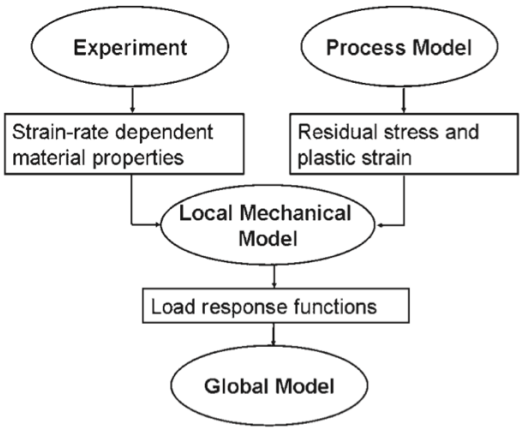

Figure 2-6: Integrated process modeling framework for predicting load response function of spot welds [43].

to predict the response function of the weld. However, this model did not consider steels with tensile strengths greater than 1000 MPa and experimental data from DP590 steels did not show any HAZ softening (see Figure 2-7). In addition, mechanical heterogeneity model needs to be improved by modeling the microstructure of the material in grain scale as a composite of different phases. Using advanced characterization techniques researchers have been able to measure the mechanical properties for different phases in the material microstructure of the weld by using in-situ nanoindentation with scanning electron microscopy and micro pillar compression test to generate a more accurate heterogeneous model of the material [13, 44, 45]. The data collected for the microstructural analysis of the base metal and weld, including the existing phases, their portions and distribution can be extracted and mapped into a model for load response model. These methods can be used to develop the current

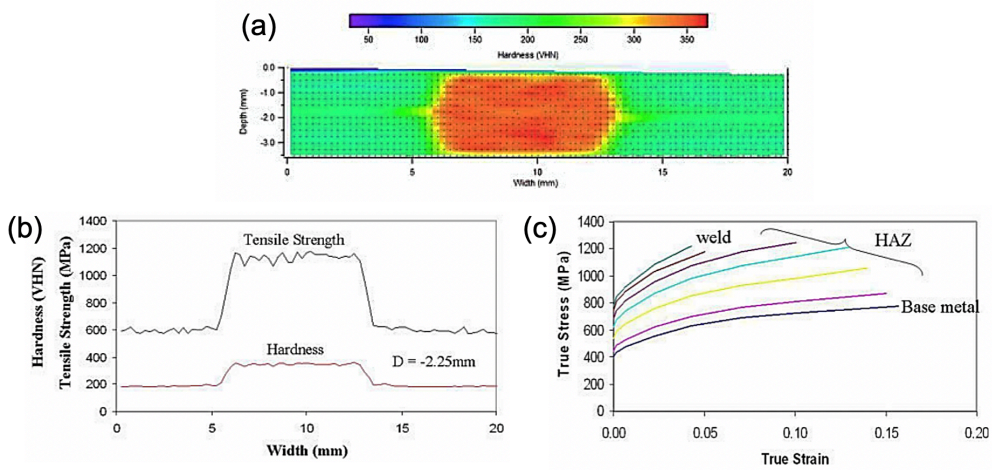

Figure 2-7: Hardness measurements for DP590 and local hardness ratios were used to scale the base metal stress-strain curves in work by Yang et al. [43]. The HAZ softening was not observed in the DP590 steel.

available computational models including the one done with Yang et al. [43]. The fracture analysis can also be added to the load response function in this model. Failure type and mechanisms in the AHSS has also been of great interest of researchers to understand the local and global loading response, fracture initiation, and failure in TS and CT samples made from these steels [38-42, 46, 47]. In the works by Dancette et al. [40-42] macroscopic failure types and mechanisms were used to categorize the failure in spot welds in following groups: (i) strain localization in regions below Ae1 where necking and failure in the thickness of sheet was observed in zone 1 of Figure 2-8 and corresponds to Button Pullout (BP) failure type, (ii) shear fracture that may take place in the spot weld notch and growth towards the regions corresponding to peak temperatures above Ae3 and below melting temperature where a fully martensitic microstructure (zone 2 in Figure 2-8), with BP failure type, and (iii) semi-brittle fracture that passes throughout the faying surface of spot weld with fully interfacial fracture (FIF) and partial interfacial fracture (PIF) types.

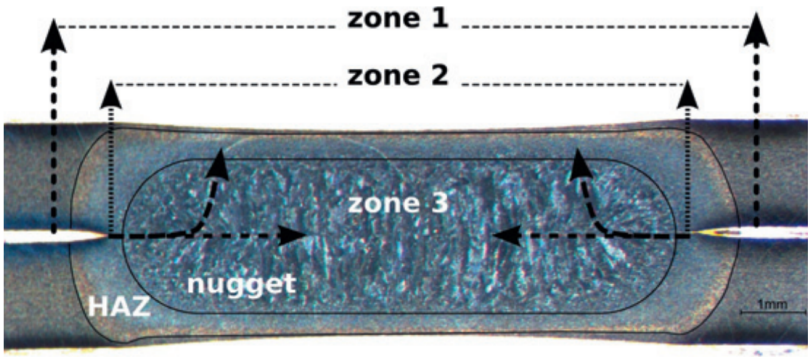

Figure 2-8: Spot weld cross section and potential failure zones for Tension-Shear and Cross-Tension samples. Adopted from the work by Dancette et al. [40].

3 Prediction of Local Elastic-Plastic Properties in AHSS Spot Welds Using Hardness Scaling Method

3.1 Introduction

Advanced High Strength Steels (AHSS) are among the new generation of steels that are being developed to satisfy recent global standards for vehicle safety, fuel economy, and emission requirements. With precisely selected chemical composition and controlled manufacturing process, AHSS possess a combination of strength, ductility, toughness, and fatigue properties due to their complex microstructure consisting ferrite, martensite, bainite, and austenite [1, 48]. Dual-phase (DP) AHSS steels consist of a soft ferrite matrix and hard second phase martensite islands for which increase in steel's ultimate strength is achieved by increasing martensite volume fraction (MVF). For martensitic steels, the entire austenite formed during annealing or hot-rolling transforms entirely to martensite during the quenching process on the run-out table. DP and martensitic steels are AHSS grades that are being widely used in the automotive industry for fabricating auto parts using resistance spot welding technique [1, 49]. Despite having desirable as-received mechanical properties, the existence of metastable phases, particularly martensite, can make AHSS sensitive to higher ranges of temperatures that occur during RSW. Previous researches [14, 16] have shown that in a process, known as martensite tempering, in temperatures between 100 °C and Ae1 line of steel, i.e., in SCHAZ, carbon atoms in carbon-supersaturated martensite microstructure get activated, start diffusing into interlath spacing and dislocations and form clusters, and finally form cementite, e.g. Fe_3C, and coarsen. The final product of this process is tempered martensite consisting ferrite matrix and cementite precipitates, with lower strength, higher

ductility, and reduced hardness. This hardness drop is mainly due to martensite tempering, and change in ferrite hardness has been shown to be slight [13]. It has been shown that time and temperature can affect the extent of softening in AHSS containing martensite [13, 14, 16, 23]. In these studies, it was shown that increasing the tempering temperatures to regions close to and below Ae1 line or increasing the tempering time can result in an increase in the extent of softening in SCHAZ. The strength and failure behavior of spot welded joints under specific combined loading conditions, mainly Tension-Shear (TS) and Cross-Tension (CT) loading, have been investigated in several studies, and failure modes were categorized as full and partial interfacial failures (FIF and PIF), round button (RB), and round button in SCHAZ (RBH) failure modes [38, 46, 47]. Finite element method has been used as the main computational tool to understand the mechanical behavior of spot welds with particular attention to local deformation and failure characteristics as well as the weld geometry on weld's strength [40, 42, 43]. In this work, we initially present the results of hardness measurements performed on spot welds made from different grades of AHSS with different MVF. Hardness drop in each region of the weld is then correlated to the steel's MVF and it carbon concentration. Hardness maps and microstructural analysis are then used to build the geometry of spot weld for FE simulations. The FE models are then partitioned into sections with constitutive behavior obtained by scaling the base metal's true stress-strain curve using the average hardness ratio in the corresponding section. Results from FE simulations are finally compared with those from Tension-Shear testing for the same steels and effectiveness of the FE model with the hardness scaled local stress-strain curves are then discussed.

3.2 Experimental Approach

DP and martensitic AHSS sheet steels with a thickness of 1.6 mm and MVF of 16%, 59%, and 100% were selected to study the extent of softening in SCHAZ

and its effects on global loading response in Tension-Shear specimens. Steel sheets from similar grades were spot welded together with welding parameters resulting nugget diameters of 6 and 8 mm. The welding procedure, specimens' geometry, and testing conditions were chosen in concert with AWS D8.9 [50]. Some of these weld specimens were cross sectioned in rolling direction and prepared for microstructure analysis and hardness measurements, according to ASTM E3 [51]. Microhardness measurements were performed on the cross section of spot welds with 300 gr load and 15 seconds dwell time.

The local hardness drop for each grade, if any, was calculated using the $(H_{BM}-H_{Local})/H_{BM}$ where H_{BM} and H_{Local} are H_{BM} and local hardness. Hardness drop was used later to correlate the extent of softening to steel's chemistry and initial microstructure. The correlations between the extent of softening with steel's carbon content and martensite carbon content (MCC), were then investigated to find which the better representation of softening is. Microhardness maps were also used along with SEM observation to recognize the weld zones and extract weld zones geometry for FE modeling of Tension-Shear testing. BM stress-strain relationship was obtained from uniaxial tensile testing. Local hardness ratio was used to scale the BM stress-strain curve to predict the local constitutive behavior, a required input for computational modeling of Tension-Shear testing.

3.3 Computational Approach

Based on the symmetry of the Tension-Shear sample and to minimize the computational time, only one half of the Tension-Shear specimen was modeled in Abaqus commercial FE package. For geometry and boundary conditions for this quasi-static testing, AWS D8.9 standard was used. Using hardness maps and microstructural analysis, spot weld in this three-dimensional model was partitioned into five cells for SCHAZ to allow for assigning loading response of the material in the form of true stress-strain curves by scaling the BM curves with

cell's averaged hardness ratio. For fusion zone (FZ), upper-critical (UCHAZ), and inter-critical (ICHAZ) one cell was created.

For DP590, since ICHAZ was wider than the other two steel grades and hardness variation was larger, two cells were used to allow for a smoother transition in material properties. It was assumed that this method of partitioning results in more realistic results for global loading response in comparison with using a single partition for HAZ regions.

Typical meshing based on tetrahedron elements with proper refinement was performed to ensure solution converges. In this work, FE models with softening and without softening in SCHAZ were used to understand how HAZ softening impact spot weld strength.

3.4 Results and Discussion

3.4.1 Softening extent in SCHAZ of spot welds

Results from hardness measurements from FZ, SCHAZ, and BM are brought in Figure 3-1 (a) for comparisons. From these results, it was observed that BM hardness increases proportionally as the MFV increases. It was also observed that when MFV in BM decreases from 100% to 59% and 16%, for M1700, DP980LC, and DP590, respectively, the hardness ratio of FZ increases significantly. This indicated the effect of base metal MFV on the hardness of the FZ. Comparing the results for the SCHAZ, as shown in Figure 3-1 (b), shows that as the MVF increases the hardness drop in this region increases. For DP590, DP980LC, and M1700 with 16%, 59%, and 100% martensite in the initial BM microstructure, the hardness drop was measured to be 6%, 18%, and 42%, respectively. This indicated that a direct correlation could be made between the MVF and hardness drop as illustrated in Figure 3-1 (b). For DP590 the softening is very low due to the small amount of martensite phase in the microstructure.

The severe softening in M1700 is clear and a result of higher MVF in this fully martensitic steel. Trends of plots in Figure 3-1 (b) show that the softening extent can be predicted more accurately by using both MVF and MCC. Here and for example, we multiplied MVF by MCC and added results to Figure 3-1 (b). This new plot suggests that a better correlation can be made by combining both these two parameters, i.e., MVF and MCC, for the prediction of softening extent. However, more investigations are needed to understand this relationship with more details. Results from micro-hardness mapping were also used to build the spot weld geometry in computational models. These results and partitions created for spot weld zones along with the mesh on the cross section for DP590 and M1700 spot welds were presented in Figure 3-2, for comparisons. As explained previously, the local constitutive behavior for each region of the weld was obtained by scaling the true stress-true strain curve of BM by the average hardness ratio of that region.

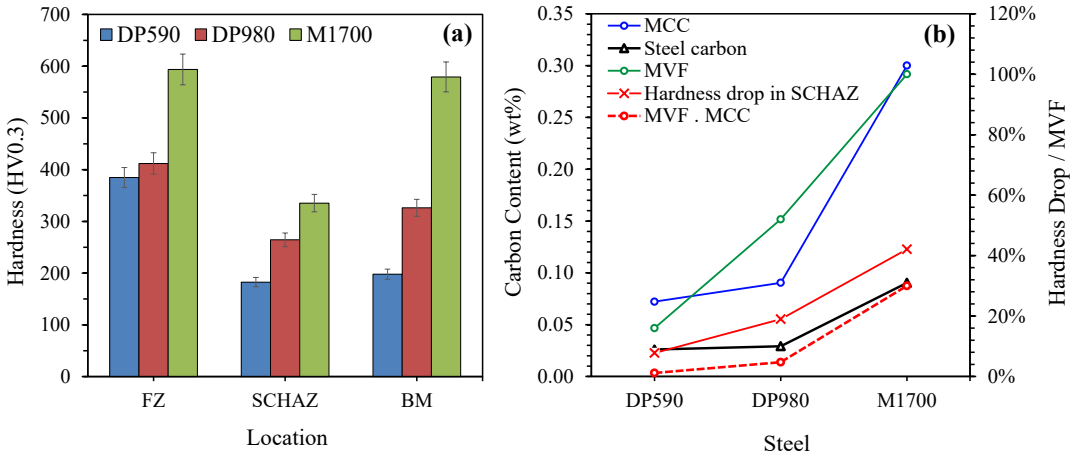

Figure 3-1: Hardness values in three regions of spot weld for steels used in this study (a), Correlation between hardness drop and MVF and carbon content (b).

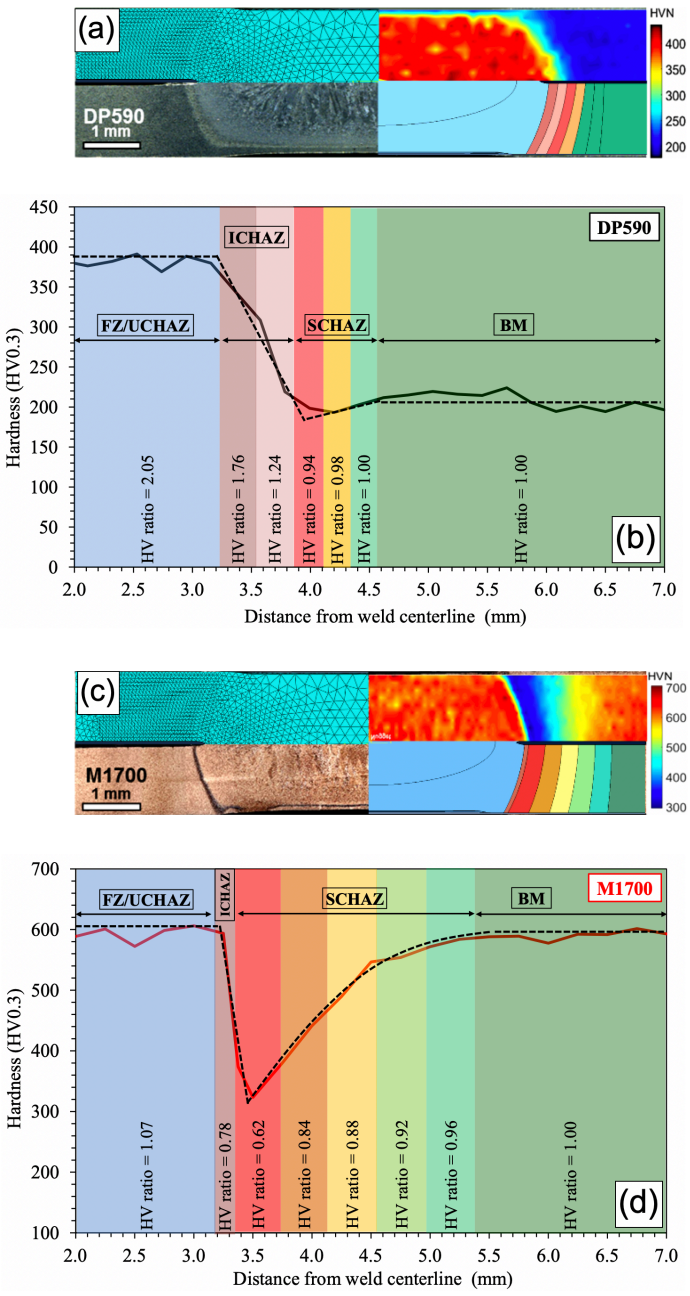

Figure 3-2: Hardness map, partitioned HAZ with local hardness ratio plot, and mesh design shown on the cross section of DP9650 (a and b) and M1700 (c and d) Tension-Shear samples.

3.4.2 Effects of SCHAZ softening on Tension-Shear global response

Finite element simulations were run for Tension-Shear models built for DP590, DP980LC, and M1700 spot welds with nugget diameter (ND) of 6 mm for models with and without softening in HAZ and results are presented in Figure 3-3 (a).

One observation from these results is that the maximum load at failure point increases as the MVF increased in both experimental and computational work. From this result, it is observed that the max load at failure has 5%, 17%, and 34% error, for DP590, DP980LC, and M1700, respectively. This increase in error can be explained by the extent of softening meaning that as the extent of softening increases, the error in results from computational modeling increases as well. This hardness ratio was used to scale the BM properties and also the weld zones were partitioned into a discrete number of the zone. In addition to these, hardness ratio was averaged through each partition.

In contrast with the FE model, real weld has material changes smoothly through and between zones. Therefore, these errors can be acceptable with simplifications that have been used in this study. Another observation from Figure 3-3 (a) can be the difference between load from weld with softening and that from weld without softening. As it can be seen, as the extent of softening increases, this difference increases as well. This implies that when the base metal has higher MVF, the impact of the maximum load for the welded joint reduces more when compared with simulations without SCHAZ softening. This, of course, is valid for this specific ND.

From FE simulations, the difference between load at experiments failure for a model with, and the one without HAZ softening is 0%, 3%, and 7% for steels with 6%, 18%, and 42% hardness drop in SCAHZ. For AHSS with BM strength above 1000 MPa, this difference is considerable, and therefore accurate measurements of local constitutive properties especially for SCHAZ become more critical.

In another attempt to study how the softened-SCHAZ and ND can affect the weld strength, the model for M1700 spot weld was calibrated by using hardness ratios less than measurements, for SCHAZ cells and modified stress-strain curves for these cells were assigned to the FE model and simulations were run for welds with softening in SCHAZ.

The results from recent simulations are plotted in Figure 3-3 (b) along with those from experiments. FE simulations show that after calibrating the model for M1700 spot weld with ND of 6 mm, model is able to predict the load-extension curve for the weld with 8 mm ND better but not overlapping with experiment.

Above shows that if the representative local properties are available, the model can predict the loading response for both nugget diameters and failure modes more accurately.

To understand the role of ND and softened SCHAZ on failure mode of the spot weld, the equivalent plastic strain (PEEQ) at the notch and SCHAZ inner edge for M1700 spot welds with 6- and 8-mm ND are plotted in Figure 3-4 (a).

Results from experiments showed that failure mode for weld with ND of 6 and 8 mm are FIF and RBH, respectively. Comparing PEEQ at notch and SCHAZ in Figure 3-4 (a) shows that PEEQ at SCHAZ for ND of 6 mm is similar to the notch. Considering PEEQ as a parameter that can be used to evaluate the failure mode, this indicates that for the 6 mm, material in notch will reach the failure criterion that can cause crack initiation, growth and finally failure in FIF mode.

Using the same approach for weld with 8 mm ND, it can be seen that the PEEQ in SCHAZ is significantly higher than that in notch indicating that material in this region meets the plastic failure strain before notch leading to necking in sheet thickness and finally failure in RBH mode.

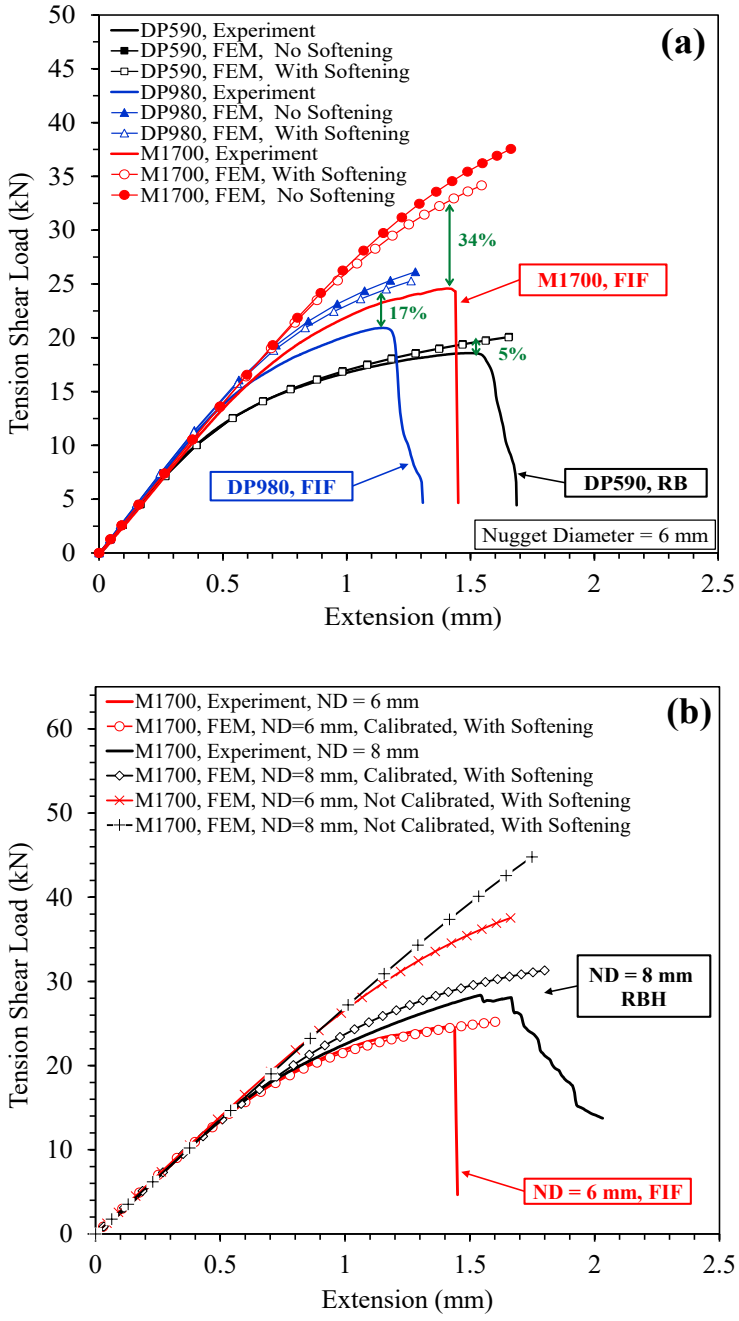

Figure 3-3: Results from FE simulation and experiments for DP590, DP980LC, and M1700 ND of 6 mm (a) and M1700 with ND of 6 and 8 mm (b).

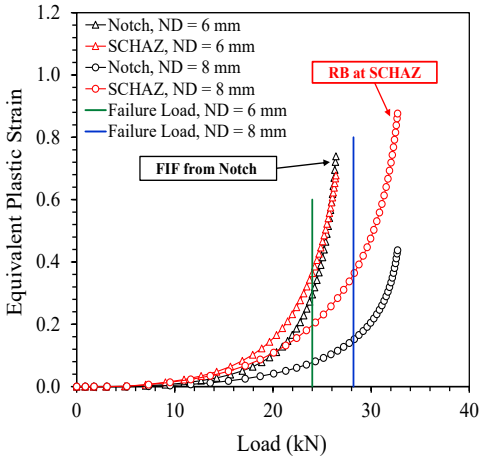

Figure 3-4: Equivalent plastic strain as a function of applied load at the notch tip and SCHAZ of M1700 Tension-Shear sample with nugget diameters of 6 and 8 mm.

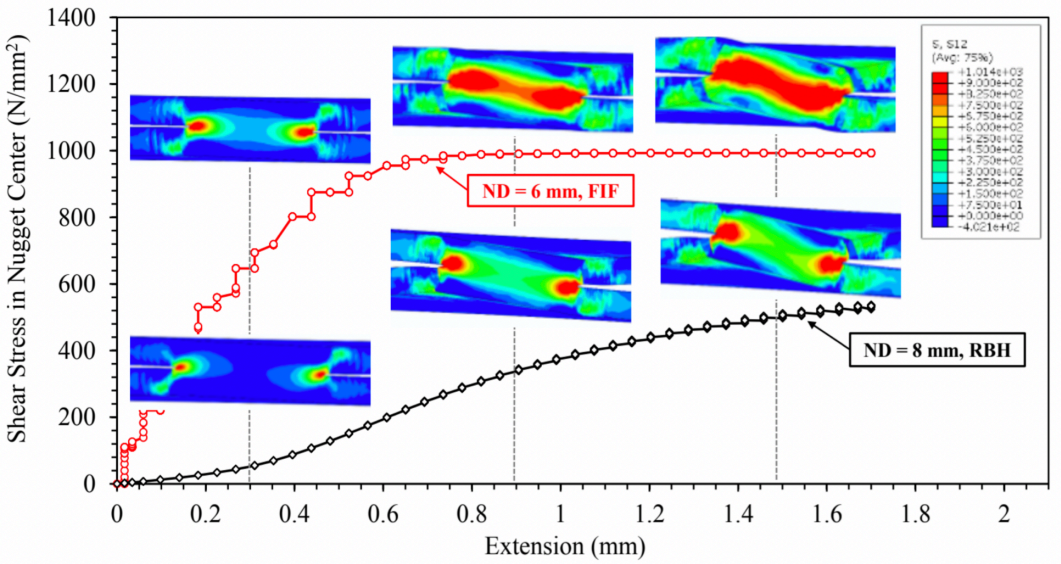

Figure 3-5: In-plane shear stress at the center of nugget on the cross section of M1700 Tensile-Shear samples with nugget diameters of 6 and 8 mm as a function of global extension.

Another observation from FE simulations was made based on the in-plane shear stress in the center of FZ for welds with 6 and 8 mm ND. Results are presented in Figure 3-5. As it can be seen, for weld with ND of 6 mm, shear stress increases significantly as the extension increases while for that with ND of 8 mm this curve is smoother with a lower magnitude. It was also observed that for weld with ND of 6 mm that failed with FIF mode, the in-plane shear stress is significantly higher than that for ND of 8 mm where failure happens at SCHAZ.

3.5 Summary

Based on the data from microhardness measurements, softening was identified in SCHAZ. The hardness drops with the magnitude of 6%, 18%, and 42% was observed in steels with 16%, 59% and 100% of martensite, respectively. The hardness ratio evaluated and used to represent as the extent of softening.

The maximum hardness drop was observed in SCHAZ close to the Ae1 line. Hardness drop increases as steel's carbon content, MVF, and MCC increase; however, it was found that a combination of MVF and MPC could be used to predict better the hardness drop or extent of softening in SCHAZ.

FE model for the Tension-Shear test with partitioned and calibrated weld zones is able to predict the global deformation behavior of specimens when the extent of softening in SCHAZ is negligible, for instance, in spot weld made from DP590. In steels with greater extent of HAZ softening, e.g., DP980LC and M1700, the contribution of SCHAZ and its local constitutive behavior increases in the prediction of deformation response.

4 Constitutive Properties and Plastic Instabilities in the Heat Affected Zones of Advanced High Strength Steel Spot Welds

4.1 Introduction

Advanced High Strength Steels (AHSS) are produced with carefully selected chemical composition and precisely controlled thermomechanical processing. Their ultimate tensile strength ranges from 550 MPa and reaches up to 2000 MPa and is related to underlying microstructures with different fractions of ferrite, martensite and austenite. These properties lead to improved safety, robust performance, and most importantly reducing the weight and achieving higher fuel economy, hence emissions reduction [1, 2] in the transportation industries. In the vehicle manufacturing process, Resistance Spot Welding (RSW) is the most commonly used joining method to assemble stamped components to form the body structure. Thus, from a steel grade design perspective it is very important to ensure that the designed product has a good combination of strength, ductility and spot weldability. Steel manufacturers put considerable effort in the design and processing of new steels to ensure satisfactory weldability in addition to meeting the requirements for basic mechanical properties and surface characteristics.

For several grades of AHSS, heat affected zone (HAZ) softening has been reported by many researchers [3, 4, 9, 12, 13, 20, 21]. Biro et al. [12] investigated the softening kinetics of the HAZ regions of Dual Phase (DP) steels through thermal simulation of base metal samples. In their research, thermal cycles at different locations were described by Biro et al. [7], using the methodology introduced by Xia et al. [18]. The methodology developed by Xia et al. [10] is

based on Rosenthal's heat transfer equations for two-dimensional cross-sections. Biro's research on DP600 and DP780 steels revealed that during the welding, martensite decomposes into ferrite and cementite when subjected to thermal cycles typical to that of subcritical HAZ (i.e., peak temperatures below Ae1). The extent of HAZ softening was confirmed with microhardness measurements. The effect of martensite fraction in the base metal on HAZ softening has been investigated by researchers like Xia et al. [18]. Their research showed that extent of HAZ softening increased with higher base metal ultimate tensile strengths, in three different DP steels during laser welding with similar process parameters. The results suggest a linear relationship between the extent of HAZ softening and base metal martensite volume fraction [18, 24]. The above phenomenon was also validated by other researchers with nanoindentor measurements: a reduction in hardness was observed in regions containing martensite, while no change was observed in ferrite grains [13]. The extent of softening has been shown to be strongly related to the tempering temperature and increases with volume fraction of martensite in base metal (BM) [13, 17, 18]. It is not surprising, because the tempering has little impact on the hardness of ferrite phase and the softening is more pronounced in the martensite [8].

Isothermal tempering kinetics of martensite is a well-known phenomenon discussed in the text books. However, the extension of these mechanisms to non-isothermal weld thermal cycles requires more attention [12, 14, 18, 26, 52] due to changes in the driving force for nucleation of carbides and also diffusivity of carbon in the matrix [26, 27] and therefore depends on the time spent at different temperatures. It has been reported [28] that the maximum softening occurs in the region close to, Ae1, i.e., the temperature at which the incipient formation of new austenite is expected [29]. Low temperature tempering and its effects on kinetics of phase transformation has been studies by several researchers [24, 53-57]. Similarly, and as a part of steel production, all DP and

martensitic AHSS undergo a low-temperature tempering treatment with typical peak temperature of about 200 °C for a period of 90 seconds. During these conditions, clustering of carbon atoms to octahedral lattice sites and dislocations and the onset of transient carbides (ε-carbides) are expected. Therefore, any further tempering from welding thermal cycle may induce the formation of cementite (M_3C) [55-58]. The observation of carbides in the nugget region is often attributed to auto tempering during the cool down cycle of the welding due to recalescence effects [24, 56, 57]. Many of the above published works show that higher heat input leads to lower cooling rate, higher peak temperature, longer time for tempering, henceforth higher magnitude of HAZ softening. The role of softening on the elastic-plastic deformation of steels has also been studied in the literature, for example, the strain localization and premature failure of the welded structure have been attributed to the softening of material in HAZ [19] of press hardened steel.

Recent researches on the new generation of AHSS [4, 5] have revealed an unexpected nonlinear relationship between the base metal tensile strength and that of the spot welded samples when base metal tensile strength exceeds 1000 MPa. These experimental results are extracted from literature and are replotted in Figure 4-1 and illustrates the nonlinearity of Tension-Shear performance above 1000 MPa. This behavior of traditional RSW joints in higher strength AHSS with more complicated microstructures could be an obstacle in using the new generation of AHSS. In our earlier attempts to rationalize the above phenomena through finite element method, the constitutive properties of different HAZ regions were scaled based on local hardness ratio [17, 59]. Using the extent of softening or hardening in the measured hardness values from the HAZ, the base material flow (stress-strain) behavior was scaled linearly. This scaling factor was assumed to be relevant to all characteristics including yield point, strain hardening exponent and ultimate tensile strength. However, our sensitivity

analyses of FEA simulations showed that such an assumption might lead to considerable uncertainty in the predicted performance of spot welded structures.

The goal of this research is to understand the effects of spot-welding process on the local deformation behavior of AHSS spot welded samples. To answer this question, we investigated the local plastic flow of the simulated HAZ samples of a wide range of DP and martensitic AHSS steels using integrated tensile testing and digital image correlation technique. There is an emphasis on the instability behavior commonly known as discontinuous yielding before the onset of homogeneous plastic flow in the material and not on the instability following diffuse necking prior to fracture. The results will provide guidance to computational modeling of spot welded performance in the future and bridges the path from local microstructural evolutions to global deformation and fracture behavior for these welds.

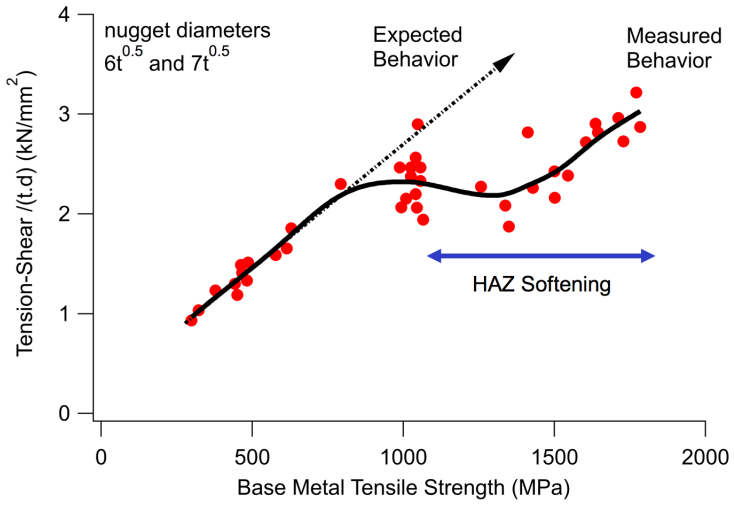

Figure 4-1: Comparison of measured Tension-Shear performance from spot welds made with DP and martensitic AHSS has shown a nonlinear relationship between the spot weld strength and base metal strength.

4.2 Experimental procedure

4.2.1 Materials

Six grades of AHSS including four DP steels (DP590, DP980LC, and DP980MC, DP1180) and two martensitic steels (M1300, and M1700) were selected to represent a wide range of chemical composition, initial microstructure, and base metal tensile strength (see Table 4-1 and Table 4-2). The yield and tensile strength are based on the results from ASTM E8 standard for the sub-size specimen with a gauge length of 25 mm, as shown in Figure 4-2. All the steels used in this study were secured from routine production coils that were tandem reduced and then processed on a water-quenched continuous anneal line. It is noteworthy that all the steels were subjected to a low-temperature tempering treatment with a peak temperature of about 200 °C for a period of 90 seconds during production. The martensite volume fraction (f_M) and its carbon content (C_M) in the dual phase steels were estimated based on image processing and the rule of mixtures. In these calculations, to estimate the martensite carbon concentration, the ferrite carbon content was assumed to be 0.02 wt.%. The equilibrium Ae1 and Ae3 phase transformation temperatures for each steel grade is calculated using JMatPro® and is summarized in Table 4-1.

4.2.2 Spot welding equipment and parameters

One set of spot welded samples was prepared for each grade by welding sheets from the same grade and thickness (total of 6 samples for 6 grades of AHSS steels used in this study). Welding parameters were the same for all welds. A Taylor-Winfield 75-85 kVA, 60 HZ single phase, AC resistance spot welding machine was used. Type A 16 mm ISO 6.0 mm EFD electrodes were used with a water-cooling system and 6 litter/min water flow. Welding procedure sequence was as follows: squeeze (70 cycles); weld time (two pulses of 12 cycle with cooling of 2 cycles between cycles); and hold time (10 cycles). A constant

Table 4-1: Chemical composition, martensite fraction, and phase transformation temperature of the investigated steels.

Steel	Alloying elements (Wt. %)			C_M (Wt. %)	f_M (Vol. %)	Transformation Temperature (°C)	
	C	Mn	Si			Ae1	Ae3
DP590	0.09	0.99	0.284	0.441	16	705	862
DP980LC	0.10	2.19	0.65	0.154	59	682	829
DP980MC	0.15	1.50	0.28	0.327	42	699	827
DP1180	0.14	2.07	0.64	0.17	81	691	822
M1300	0.19	0.39	0.15	0.19	100	723	844
M1700	0.31	0.47	0.19	0.31	100	725	812

Table 4-2: Tensile properties and hardness of the as-received AHSS used in this study.

Steel	Thickness (mm)	YS (MPa)	UTS (MPa)	Total Elongation (%)
DP590	1.5	390	636	23
DP980LC	1.4	710	1056	13
DP980MC	1.6	624	1025	13
DP1180	1.6	956	1266	11
M1300	1.4	1154	1386	6
M1700	1.6	1706	1876	5

electrode load of 5kN was used for all welds. The welding procedure, samples' geometry, and testing conditions were selected according to AWS D8.9 standards [50].

4.2.3 Prediction of thermal cycles and Gleeble thermal simulations

Because of the difficulties in direct measurement of temperature during spot welding, finite element (FE) method was used to obtain the local thermal cycles by simulating the spot-welding process. In this work, results from previous FE simulations by Ghassemi-Armaki et al. [19] were used to interpret the spot weld microstructures. These FE simulations were performed using SORPAS (by SWANTEC) on the same steel grades and sheet thickness. Six locations were selected within the HAZ region of the spot weld corresponding to peak temperatures of 350, 500, and 650 °C [i.e. sub-critical HAZ (SCHAZ) below the Ae1 temperature], 760 °C [i.e., inter-critical HAZ (ICHAZ), between Ae1 and Ae3] and two peak temperatures in upper-critical HAZ (UCHAZ); 950 °C corresponding to fine-grained HAZ (FGHAZ) and 1250 °C corresponding to coarse-grained HAZ (CGHAZ). The extracted thermal cycles were used in a Gleeble-3800 thermomechanical simulator. Thermal histories for Gleeble simulations are presented in Figure 4-3. For the Gleeble simulations, 126 samples (6 steel grades × 3 repeats × 7 peak temperatures) were prepared from AHSS sheets. Tensile tests were performed on specimens with dimensions according to ASTM E8 standard with 25-mm gauge length and dimensions shown in Figure 4-2.

The Gleeble samples were designed such that a uniform temperature is achieved in the middle of samples with dimensions equal to or larger than needed for tensile testing and correspond to the conditions typical to that of HAZ regions from a spot weld. This methodology involved two steps: (1) During Gleeble simulations; four thermocouples were used to measure the temperature gradient in rolling and transverse directions (as shown in Figure 2). The largest drop in

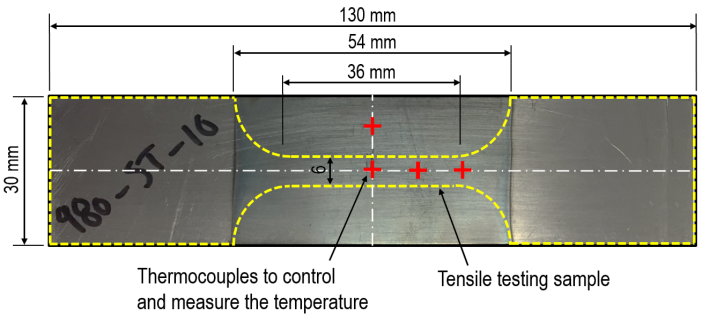

Figure 4-2: Dimensions for the samples used in Gleeble simulations with the outline for the sample used in tensile testing. Tensile sample dimensions are according to ASTM E8 sub-size standard specimen.

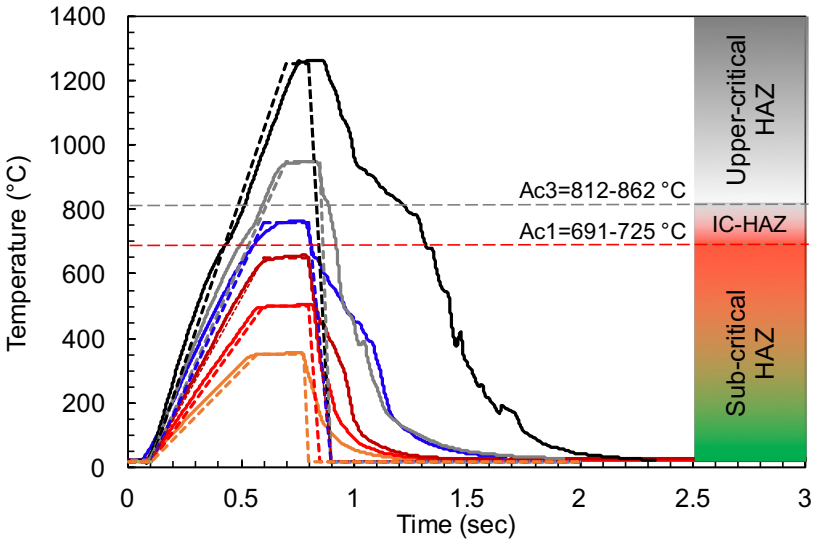

Figure 4-3: Overview of the programmed and measured thermal cycles used for simulating different regions of heat affected zone in Gleeble® thermo-mechanical simulator. The dashed lines show the programmed thermal cycles and the solid lines show the measured ones from thermocouples. Note that we are not able to achieve rapid cooling rate in the experimental sample due to inherent thermal mass in the system.

peak temperature was measured to be 23 °C in rolling direction and place close to the grips. In transverse direction, temperature drop was negligible. (2) The hardness measurements were performed on the cross section of samples cut from Gleeble samples.

4.2.4 Microstructural characterization and hardness measurements

Microstructure of the Gleeble and spot welded samples were characterized using standard characterization techniques [60]. Microhardness measurements were performed by using a hardness tester with 300 grams of load and 15 second dwell time on the cross-section of both the spot welds and Gleeble simulated HAZ samples in the rolling direction, as per the ASTM E92 standard.

The indent spacing was kept at 250 μm for all measurements, unless otherwise specified. Hardness measurements were used for following purposes: (1) to evaluate the local hardness and reveal the hardness heterogeneity throughout the spot weld regions, (2) to distinguish different regions of spot welded samples by comparing the hardness values and transitions, and (3) to calibrate the thermal cycles for the Gleeble thermal simulation as explained later in this section.

4.2.5 Calibration of Gleeble thermal cycles using hardness values

The calibration of thermal cycles for Gleeble simulations were performed by using hardness measurements. This ensured that the final microstructure is similar to that of the spot weld for the corresponding peak temperature. Results from this step are shown in Figure 17 for peak temperature of 650 °C. Microhardness measurements were also used check the uniformity of material in the gauge length of tensile samples.

Typical results are presented for M1700 samples subjected to two

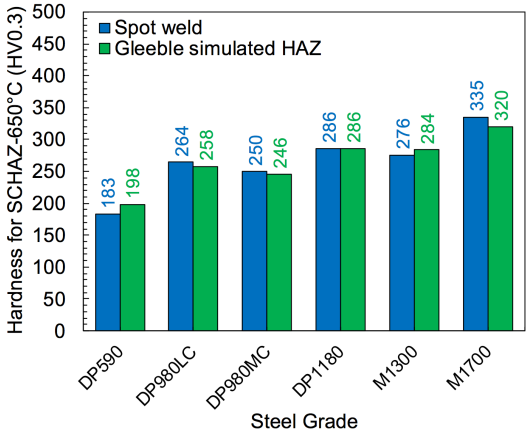

Figure 4-4: Comparison between hardness values from Gleeble thermal simulation for 650 °C peak temperature (as an instance) and softest region of HAZ in all the steels show only slight differences that are within the uncertainty of indenter locations (±200 μm) and hardness measurements (±10 HV).

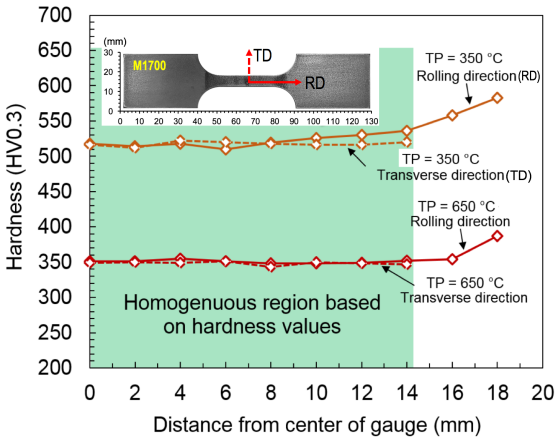

Figure 4-5: Measured hardness distribution in M1700 sample subjected to thermal simulation with 350°C and 650 °C peak temperature along two different directions confirm the validity of our approach to use Gleeble samples as a surrogate to extract constitutive properties of HAZ regions.

tempering temperature of 350 and 650 °C presented in Figure 18, illustrate a uniform distribution of hardness in both rolling and transverse directions. These results proved the validity of our approach to using Gleeble® simulated samples to extract the stress-strain behavior of spot weld HAZ regions.

4.2.6 Tensile testing and digital image correlation technique

The MTS Criterion® C45 universal tensile testing frame was used to perform uniaxial tensile and Tension-Shear testing. The loading condition was set at a displacement rate of 2 mm/min for both type of tests. The tensile testing samples, extracted from the Gleeble samples, follow the ASTM E8 standard.

For spatially resolved measurement of deformation and strain fields within the gauge length, a DIC system (manufactured by Correlation Solutions) was used. Following the procedures suggested by the manufacturer, the surface of samples was coated with prime white and dark speckle patterns on the surface.

VIC-2D image analysis software (Correlation Solutions) was used for post-processing the DIC data. A sampling rate of 10 Hz was used. A virtual extensometer with a length of 25 mm in gauge (along the sheet rolling direction) was used within the VIC-2D software to calculate the overall strains. With these measurements, the engineering and true stress-strain curves were described for different HAZ regions of all the steels.

Tension-shear testing was also used to capture the typical deformation behavior in DP and martensitic steels. DP590 and M1700 spot welded samples were made in concert with AWS D8.9 standard with nugget diameter of 8 mm for both samples. After loading and failure, these samples were cut in the loading direction to reveal the deformation behavior in different regions of welded samples with more details.

4.3 Experimental results

4.3.1 Plastic flows

The methodology for extracting these curves from tensile testing and DIC raw data is explained in Section 2. These results are presented in following in Figure 19, in the form of engineering stress-strain curves and for the readers' review.

4.3.2 Results from Tension-Shear testing

Results from the Tension-Shear tests on DP590 and M1700 spot welded samples are presented in Figure 4a. In both samples the failure locations are identified as the regions that have been heated below Ae3 phase transformation temperatue of each steel. This identification was based on locally experienced peak temperatures predicted by finite element models, as well as, the measured hardness values and their gradients from spot welded samples. The nugget rotation and extent of deformations were significantly different in these two samples. DP590 spot weld shows larger rotation in nugget. In addition, in this sample the plastic deformation in regions close to failure were more pronounced in comparison to that in M1700. Although it is tempting to correlate the failures in M1700 to brittle failures expected in martensitic steels, careful analyses of the failed region showed localized deformation (see Figure 4-7 (b) and (c)). The above results confirm the need for correlation of local microstructural gradients in spot welds (see Fig. 4d) and its response to localized and global plastic deformations, as investigated in the following sections.

4.3.3 Typical local microstructure of spot welds

To understand the localized plastic deformation in M1700 spot welds, high-magnification images of microstructural heterogeneity before mechanical testing is presented in Figure 5. In the as-received base metal of M1700 steel, a martensitic lath microstructure with fine carbides (bright imaging) was observed.

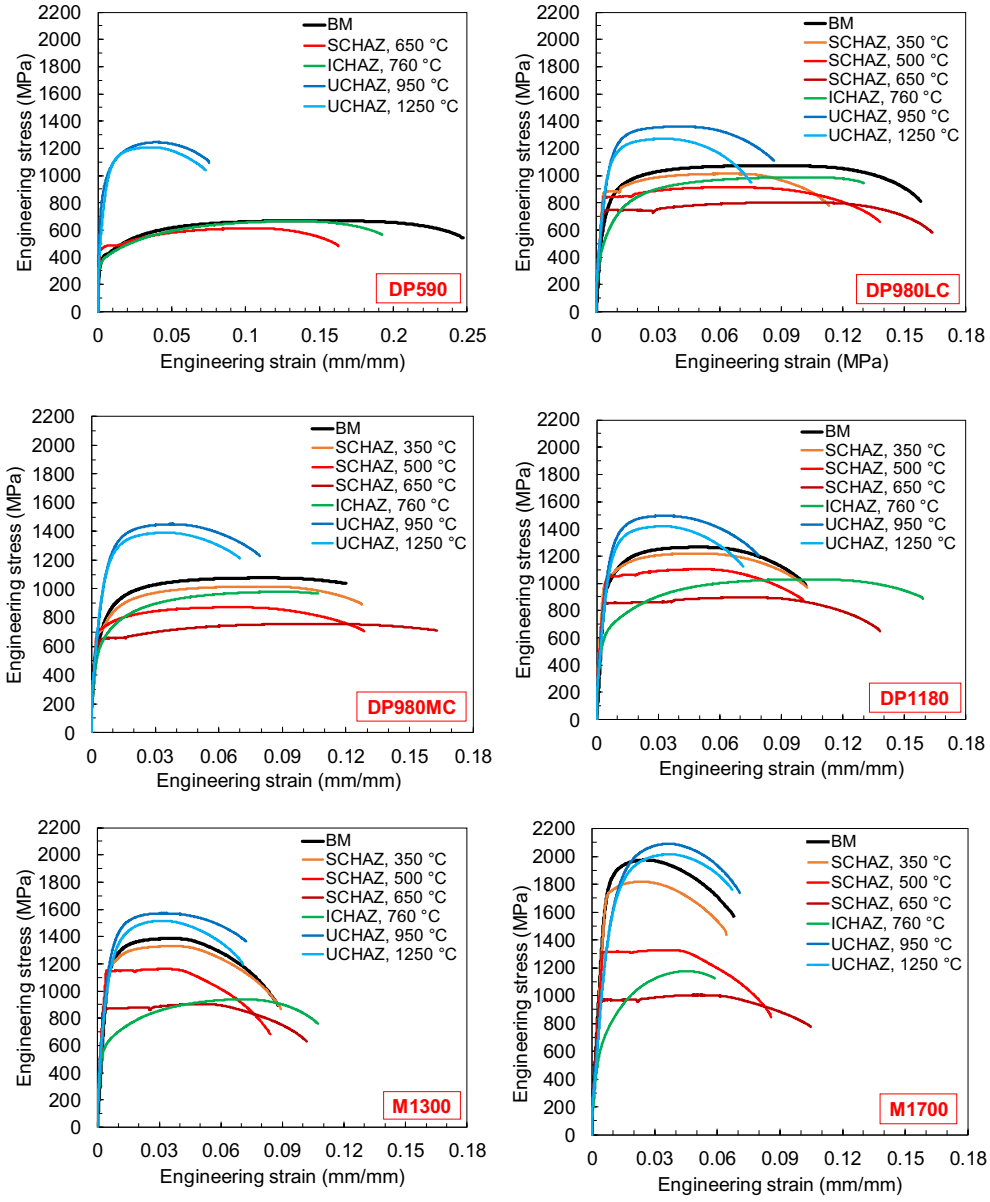

Figure 4-6: Engineering stress-strain curves obtained from tensile testing of base metal and Gleeble simulated HAZ samples for all six grades of DP and martensitic AHSS used in this study.

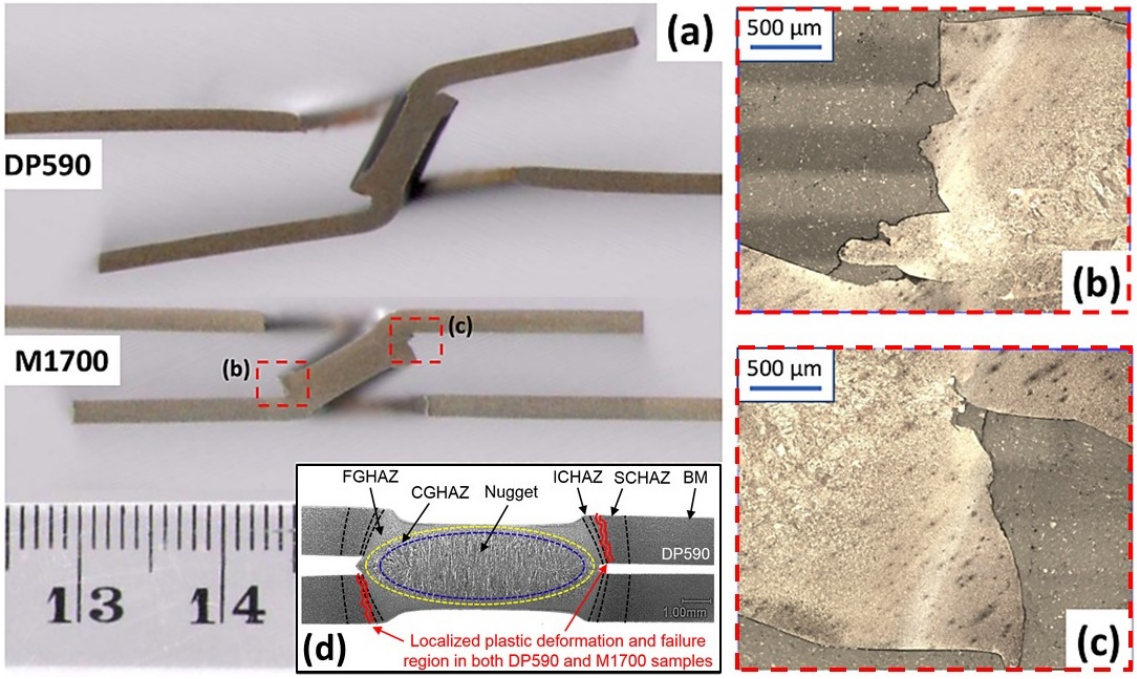

Figure 4-7: (a) Global deformation behaviors and failure in DP590 and M1700 Tension-Shear samples. Different extents of nugget rotation and global deformation can be observed (a). Localized plastic deformation in M1700 steels are marked in locations and are shown in high-magnifications (b) and (c). Failures in both steels are correlated to regions with peak temperature below Ae3 based on comparing the location of failures with predicted thermal distributions from the FE simulations and hardness measurements and are schematically illustrated in (d).

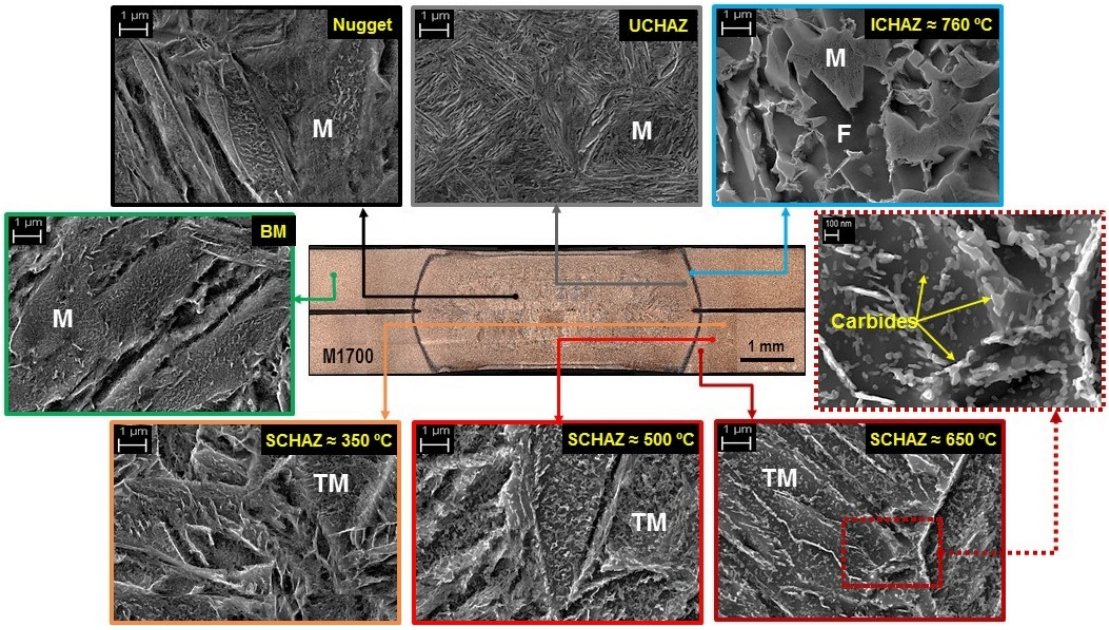

Figure 4-8: Overview of microstructural heterogeneity within the spot welded sample made from M1700 AHSS steel obtained using scanning electron microscopy. The annotations are explained as following: M-Martensite; F-Ferrite; and TM-Tempered Martensite. Note that the identification of carbides is based on the contrast observed in the SEM images.

This is indeed expected since the base metal undergoes a low temperature tempering step during production. Results for the nugget of spot weld similarly showed a martensitic microstructure with fine carbides. The existence of fine carbide in this region can be attributed to auto tempering due to recalescence effect (release of enthalpy of fusion) during weld cooling [24, 56, 57, 61]. The upper-critical HAZ (UCHAZ), including regions corresponding to peak temperatures of 950 °C (FGHAZ) and 1250 °C (CGHAZ), also contained martensite with some brightly imaging fine carbides. Perhaps the most interesting observation from the microstructural analysis is for ICHAZ. In this region, an aggregate of ferrite and martensite phases was observed with the amount of the latter increasing as we move towards the fusion line. Although, we cannot accurately assign the peak temperatures to different locations within the HAZ of spot welds, our interpretation of interpretations of different regions are based on the etching response, high-magnification observation of microstructure and also the measured hardness gradients (see Figure 4-9).

The widths of ICHAZ varied from 0.1 to 0.3 mm, depending on the chemistry and phase transformation temperatures of each steel. In the SCHAZ of dual phase steels, we observed ferrite and tempered martensite. In the case of martensitic steels, only tempered martensite was observed. In SCHAZ corresponding to lower peak temperatures (BM and lightly etching regions) cementite particles are finer and more dispersed while in regions experiencing higher peak temperatures (darkly etching), the cementite particles are sparse and coarsened in martensite substructures and along the prior austenite grain boundaries.

Based on the iso-surface temperature contours from FE analyses, the lightly etching regions should have experienced a peak temperature below 350°C and the darkly etching regions should have experienced peak temperatures ranging from 500 to 650°C. Above identifications are phenomenological and must not be considered as fact due to our inability to extract thermal signatures during

welding. Therefore, we have used FE simulation results, hardness measurements, and microstructural features to correlate the local plastic deformation and failure to microstructures in the SCHAZ or ICHAZ regions. It is noteworthy that these observations are not new and have been reported extensively in the literature [9, 12-14, 57, 62-65].

4.3.4 Microhardness examination of spot welded samples

Results from microhardness measurements performed on the cross section of spot welded samples are presented in Figure 4-9. These results illustrate the existence of softening and hardening in the HAZ of all steels, however with different extents. The softening is observed in two regions of spot welded samples: (1) In the SCHAZ of all steels with DP590 and M1700 possessing the minimum and maximum hardness ratios of 94% and 58%, respectively; (2) In the ICHAZ regions wherein minimum hardness was similar to that of SCHAZ and experience peak temperatures close to Ae1. In ICHAZ an increase in hardness with an increase in the freshly formed martensite is observed.

Interestingly, the above data also correlated with microhardness data measured from samples (to be described later) subjected to Gleeble thermal simulations. For example, the maximum hardness values were observed in the samples with two peak temperatures used in Gleeble simulations; 950 °C and 1250 °C corresponding to FGHAZ and CGHAZ, correlates with martensite microstructure that forms within fine and coarse-grained austenite grains in the spot welds, respectively.

4.3.5 Comparison of YS, UTS and strain hardening exponent of Gleeble simulated HAZ samples

Raw data from all tensile tests performed on Gleeble thermally simulated specimens are presented earlier in this chapter. For comparative purposes, here we use the YS and UTS ratios and measure strain hardening exponents as

shown in Figure 7 (a) and (b) and Figure 8. Results presented in Figure 7 (a) show an increase in YS ratio for samples with T_{peak} = 350 °C, followed by a continuous decrease as T_{Peak} approaches the 650 °C, for DP steels. The trend is different for the fully martensitic steels (M1300 and M1700) in which a continuous reduction of YS ratio is observed. Interestingly, for both the DP and martensitic steels, the reduction in YS ratio continues to ICHAZ regions, where the T_{Peak} was 760 °C with values lower than that of SCHAZ regions for all steels. The DP590 and M1700, possess the minimum YS to be 1.02 and 0.38, respectively, in the entire HAZ. By increasing the T_{Peak} and eventually going above the Ae3, the YS increases in all steels. The maximum YS ratio was observed in UCHAZ with a peak temperature of 950°C wherein the FGHAZ microstructure was observed from the microstructural analysis. The minimum and maximum YS ratios were observed at T_{Peak} of 950 °C for DP590 and M1700 to be 2.34 and 1, respectively.

Similar analyses were performed using the UTS ratios for all steels. Results shown in Figure 7 (b) confirm that the tensile strength in SCHAZ decreases with an increase in peak temperature and minimum UTS for all steels observed in SCHAZ at T_{Peak} of 650°C. The minimum and maximum UTS ratio observed for DP590 and M1700 to be 0.96 and 0.54, respectively. The maximum UTS observed for all steels with a peak temperature of 950°C in the region where the fine grain martensitic microstructure was observed from SEM analysis. The UTS ratio slightly decreases by moving from 950 °C towards 1250°C peak temperature. The change in strain hardening exponent (n term in the flow curve equation $\sigma = k\varepsilon^n$) for steels subjected to different thermal cycles are summarized in Figure 8. Interestingly, the “n” values decreased to a minimum value of 0.04 for the all the samples subjected to thermal cycling at a peak temperature of 500°C which corresponds to semi-perfect plastic behavior. The two fully martensitic steels (M1300 and M1700) show the largest drop in strain hardening despite the high strain hardening values in base metal before thermal cycling. With the

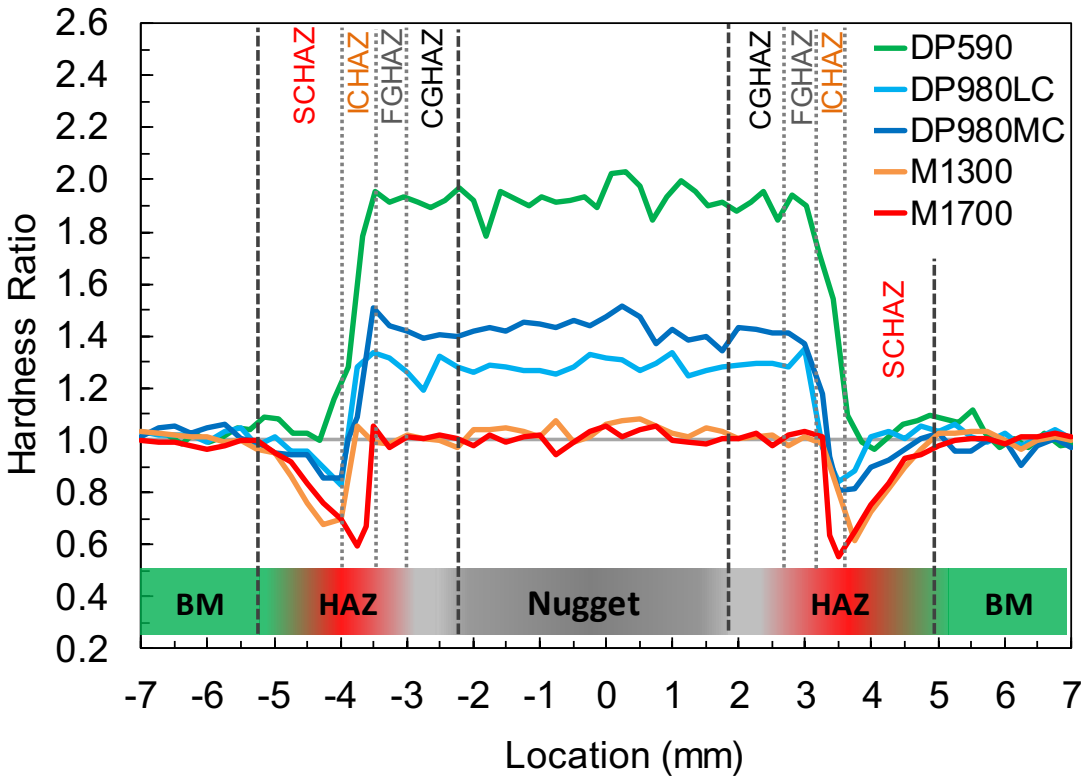

Figure 4-9: Hardness ratios along the diagonal line across spot welds showing the hardness heterogeneity. Results show softening in SCHAZ and ICHAZ regions and hardening in UCHAZ and nugget. The base metal hardness for each steel is measured as: DP590: 199, DP980LC: 324, DP980MC: 311, M1300: 452, and M1700: 585 Vickers. Dash lines show the approximate boundaries between regions of the spot welds.

increase in peak temperature from 500 °C to 650 °C, the hardening exponent increases up to 760°C corresponding to the ICHAZ, where at the highest value were observed for all steels. The strain hardening shows a slight decrease with increase in peak temperature and by moving from the ICHAZ towards UCHAZ.

4.3.6 Observation of yield point phenomena

Discontinuous yielding in the form of yield point phenomena (YPP) with corresponding Lüders band was observed in thermally simulated samples for peak temperatures below Ae1 (i.e., SCHAZ) in all the steels. The YPP is characterized by upper yield stress (UYS), lower yield stress (LYS), and Lüders strain (ε_L), as shown schematically in Figure 9 (a). The interpretation of stress-strain curves with YPP is schematically illustrated in Figure 9 (b) with the spatial strain field calculated from DIC analysis of DP1180 steel subjected to thermal cycles with a peak temperature of 650°C, as an instance.

Figure 9 (b), shows the Lüders strain initiation and propagation in the gauge length of the sample at different stages marked as (1), (2) and (3). With continued straining above the YPP, the strain hardening sets in and eventually leads to failure (Figure 9 (b, 3-6)).

4.4 Discussion

The primary focus of this chapter is to investigate the effect of thermal cycles with different peak temperatures, similar to those in spot welding process, on the local constitutive properties of DP and martensitic advanced high strength steels. In the previous section, the variation of plastic flow properties in terms of YS, UTS, and strain hardening exponents are summarized.

The re-emergence of YPP and corresponding Lüders strain are also shown. Although, previous researches are focused on the elastic-plastic properties of tempered DP and martensitic steels, all of them ignore the local mechanical

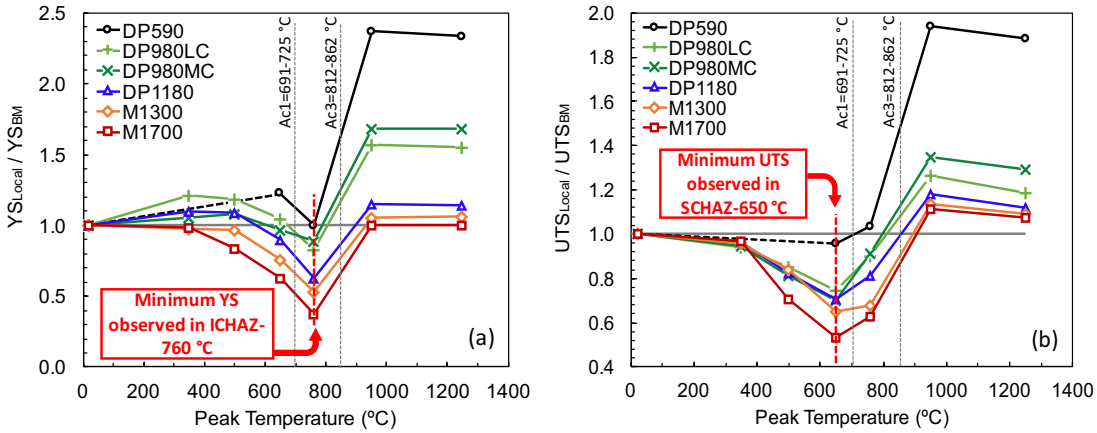

Figure 4-10: Variation of yield stress and ultimate tensile stress as a function of peak temperature obtained from Gleeble thermally simulated HAZ samples.

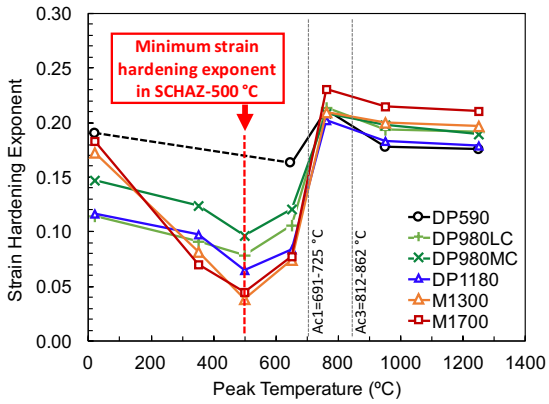

Figure 4-11: Variation of strain hardening exponent as a function of peak temperature obtained from Gleeble thermally simulated samples.

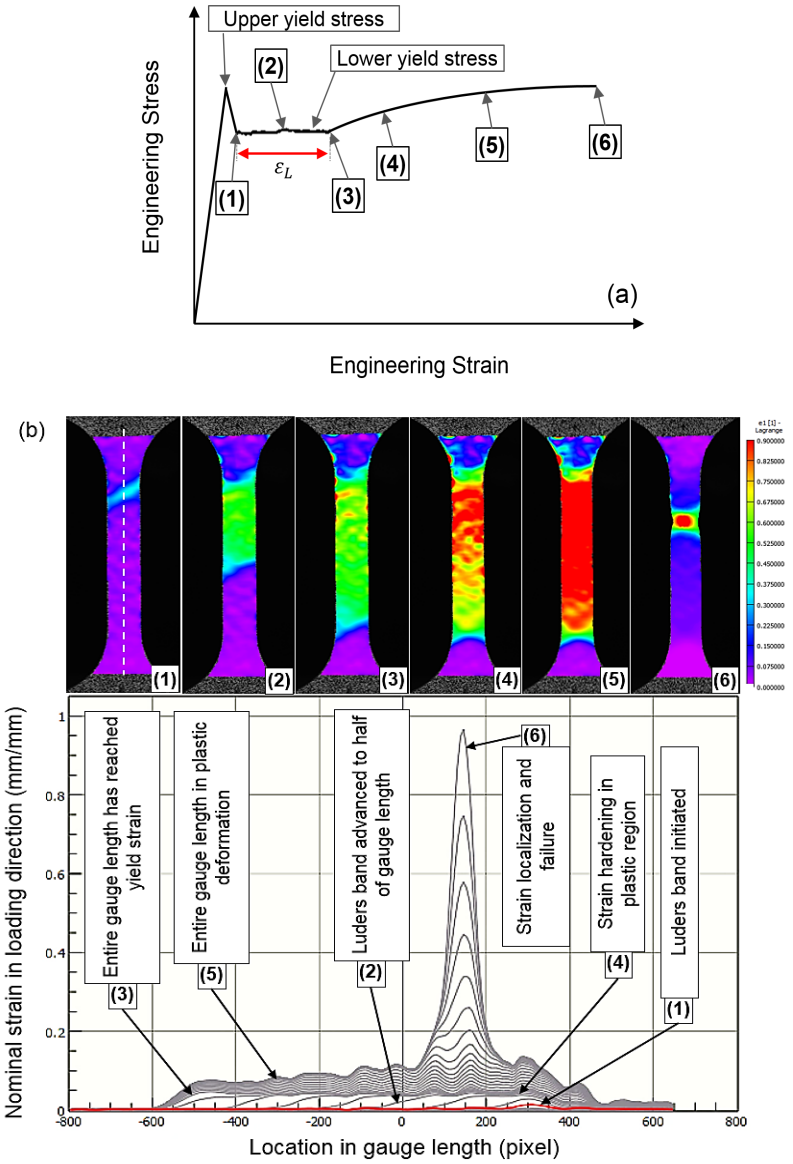

Figure 4-12: Schematic representation of stress-strain curve for material with discontinuous yielding (a) and DIC images from Lüders band initiation and propagation in the gauge length and strain along the path in the loading direction for DP1180 Gleeble simulated HAZ sample tempered to 650 °C (b).

heterogeneities in scales smaller than gauge length and the associated plastic instability. Therefore, in the following discussions, we initially discuss the material heterogeneity and then evaluate the details of plastic instability. Finally, these characteristics will be correlated to the underlying microstructures.

4.4.1 Heterogeneous plastic flow properties

Results presented in section 3 show that thermal cycles with different peak temperatures could lead to significant changes in local constitutive properties (YS, UTS, and hardening exponent) for thermally simulated samples that are simulative of local regions of spot welds. As these local microstructures influence deformation behavior and failure of AHSS spot welds the heterogeneity of elastic-plastic properties needs detailed analyses. Since the lowest values for YS and UTS ratios were measured from samples with peak temperatures of 760 and 650 °C for all steels, these regions can experience strain localization leading to lower strength and/or change in failure mode that is described in Figure 4-1. Therefore, the discussions in this section will be primarily focused on samples heated to these two peak temperatures. Figure 10 shows the YS and UTS ratios for different steels used in this study. As it can be seen, for all these steels (except DP590) and at these peak temperatures, the YS and UTS ratios are below one (except DP590 and DP980LC). This implies that the mechanical heterogeneities increase in higher grades of these steels. Another interesting observation is that the YS ratio in ICHAZ (at 760 °C) is lower than that in SCHAZ (at 650 °C) in all the steels. This result suggests that this region may be the initial site for the strain localization in spot welds. It is noteworthy that we have used only one peak temperature (760 °C) for reproduction of ICHAZ material and therefore we do not know whether this result is generic and applicable to other peak temperatures with different fractions of fresh martensite. At other temperatures, substantially above Ae1 and reaching Ae3, the extent of the newly formed austenite is expected to increase by replacing the initial microstructure of

the base metal. These continually varying fractions of ferrite (low carbon supersaturation with no carbides), tempered martensite (partial carbon supersaturation with carbides) and fresh martensite that forms from the austenite fromed during reheating are bound to influence the overall strain partitioning between these constitutent phases. Implictions of these heterogeneous plastic properties will be explained later in this section, after detailed analyses of the spatial and temporal plastic instabilities observed in DIC.

4.4.2 Spatial and Temporal Variations of Plastic instabilities

An important outcome of our experimental work is the observation of plastic instability, in the form of yield point phenomena, in samples with peak temperatures corresponding to SCHAZ regions (< Ae1). As presented in Section 3, the YPP and corresponding Lüders strain were mainly observed in samples with peak temperatures corresponding to 500 and 650 °C, and was negligible in samples with peak temperature of 350 °C. Figure 11 summarizes the effect of peak temperature on Lüders strain: the measured Lüders strain increases with the peak temperature and reaches the maximum in samples heated to a peak temperature of 650 °C for all the steels.

The only exception to this observation is from DP980MC because there was no momentous change in Lüders strain from samples heated to 350 to 500 °C. In contrast, DP1180 and DP980MC steels showed the largest and smallest Lüders strain at 650 °C, respectively. The Lüders strain can be correlated to the carbon content in the ferrite (BCC) or partially tempered martensite (BCC/BCT) lattice structures. This hypothesis was confirmed by correlations shown in Figure 12, *i.e*., the Lüders strain of SCHAZ samples decreases with carbon concentration of martensite. The observation of YPP and Lüders strain and association only with samples of certain thermal cycles needs to be rationalized and will be the focus of the next section.

Results shown in Figures 11 and 12 are based on DIC measurements from a 25-mm gauge length on the surface of tensile samples. Therefore, these values are average of the overall response of aggregated plastic flow that are happening at different rates across the whole gauge length. It is quite possible that the plastic flow properties at local levels can be different in regions containing varying mixtures of original ferrite, partially or fully tempered martensite, newly formed martensite that have been produced during thermal cycling. By post-processing the DIC data and plotting the Lüders band velocity, we can get insight into the dynamics of nucleation and growth of plastic instabilities in gauge length of samples. Results from such analyses (strain value of 0.1) was performed for DP590, DP980LC, and M1700 steel samples subjected to thermal cycles with a peak temperature of 650 °C are shown in Figure 13. The results from Lüders velocity contours show different behavior. As it can be seen in M1700 sample, the number of Lüders band nucleation sites are significantly higher than that in

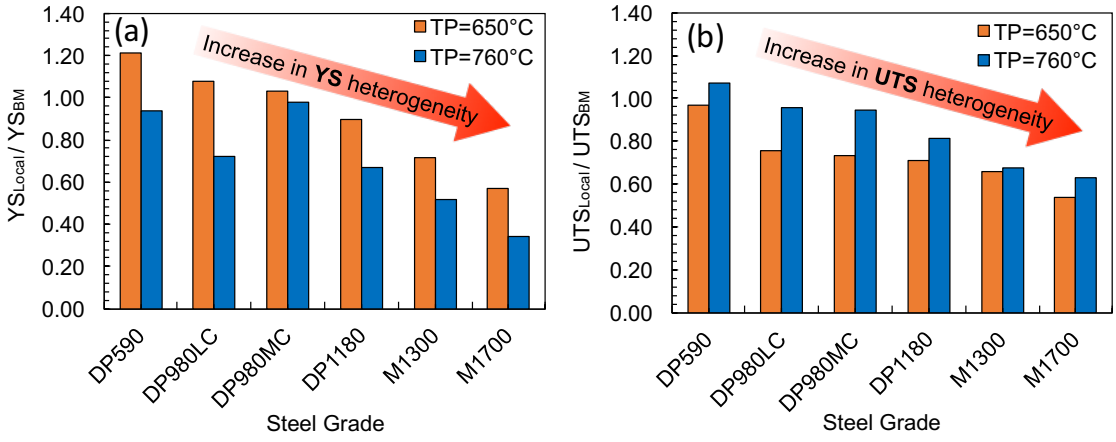

Figure 4-13: Plastic flow heterogeneity in HAZ of AHSS spot welds based on results from tensile testing on thermally simulated samples. This heterogeneity increases in higher grades of these steels.

DP980LC and then DP590. The Lüders velocity is also different with higher values belonging to M1700 and then DP980LC. This result confirms that the Lüders strain has different orientations with reference to loading axis, potentially due to spatial variation of the texture. Currently, such small-scale effects cannot be modeled using the finite element models and may require microstructure-based crystal plasticity models.

4.4.3 Overview of Microstructural Changes and Rationalization of Plastic Instabilities

The kinetics of phase transformations of DP and martensitic steels during isothermal and non-isothermal thermal conditions, as well as their correlations to stress-strain behaviors has been extensively studied in the literature [4, 9, 11-14, 18, 20-22, 24, 25, 35, 55-57, 61, 63, 66-84]. Based on the comprehensive review of the literature and computational models, we provide a schematic illustration of the microstructure evolution in six grades of steels during thermal cycling. The diagram is based on microstructure evolution in dual phase steels (see Figure 14). Similar evolutions are expected for the fully martensitic steels by considering only the martensite phase.

UCHAZ region: In this region, the steel is heated to single phase austenite region and cooled rapidly to room temperature. This leads to the formation of fresh martensite from both fine- and coarse- austenite grains. These regions which are known as FGHAZ and CGHAZ have been studied extensively in the welding literature. Since the plastic instabilities were not observed in this region, rest of the discussions will focus only on the SCHAZ and ICHAZ regions.

SCHAZ region: In this region, the only microstructural change (see Figure 14b) is related to continued tempering of the pre-existing martensite. It is

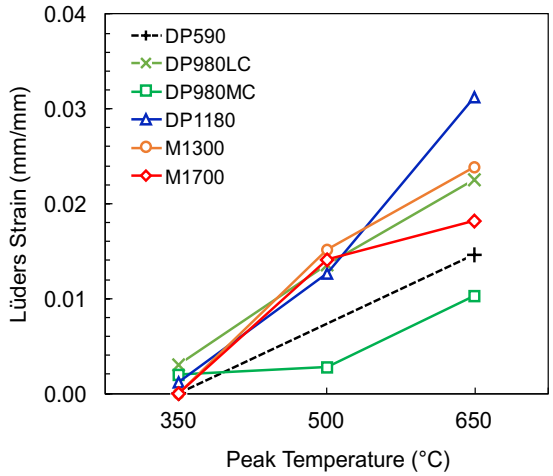

Figure 4-14: Lüders strain measured from Gleeble simulated SCHAZ samples. In all steels Lüders strain in SCHAZ increased with the thermal cycle peak temperature.

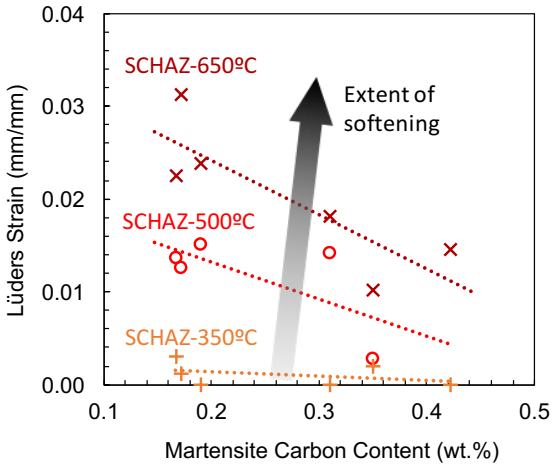

Figure 4-15: Lüders strain as a function of martensite carbon content and peak temperature in SCHAZ. Lüders strain showed an inverse correlation with martensite carbon content and increased with thermal cycle peak temperature.

well known that this tempering reaction is accompanied by carbon clustering within the lattice or to the dislocations, growth of pre-existing carbides, nucleation and growth of new carbides. Furthermore, a reduction of dislocation densities, that formed during the original martensitic reaction before thermal cycling, is also expected. The extent of these reactions is dictated by thermal signatures that control the time spent at different temperatures below Ae1.

ICHAZ region: In the ICHAZ, previously tempered martensite in the base metal transforms partially into austenite (see Figure 14c) on heating above Ae1. Due to rapid heating, short isothermal heating, and cooling cycles, the carbides in original tempered martensite are partially dissolved. On cooling down, this austenite transforms to fresh martensite.

Due to the inherent difference in thermal expansion coefficient between ferrite and austenite, during the cooling and transformation of the austenite to martensite, stresses will be generated in the original tempered martensite or ferrite. This boundary conditions may induce the geometrically necessary dislocations in the boundaries of original BM microstructure and freshly formed martensite. Similar to the other regions of HAZ, the extent of fresh martensite will be dictated by thermal signature, i.e., peak temperature and time spent above the Ae1 temperature.

Rationalization of Yield Point Phenomenon: Emergence of yield point phenomenon is related to Cottrell atmosphere brought about by segregation of carbon and/or nitrogen to dislocations which pins the mobile dislocations and the onset of Lüders strain [85-91]. While the upper yield stress is related to the static pinning of dislocation by Cottrell atmosphere [85, 86], however, the rapid dislocation multiplication has been known to play a significant role in the Lüders band propagation and strain [87, 92, 93].

Both phenomena are strongly related to the carbon content and dislocation density of steels. The formation of Cottrell atmosphere has been shown to be strongly related to the amount of free carbon and mobile dislocation density in the microstructure and the interaction between these two [86, 88-91]. The observation of YPP in SCHAZ of fully martensitic steels of this study indicates that this phenomenon can happen in tempered martensite. Several studies have also shown that tempering supersaturated ferrite can also lead to the formation of Cottrell atmosphere and hence occurrence of YPP [87].

The carbon content of bcc iron can change as the peak temperature changes. This is shown in Figure 15 based on thermodynamics calculation using JMatPro® software, for equilibrium condition. Interestingly, the ferrite carbon content increases significantly, i.e., about ten times as the tempering temperature increases from 350 to 650 °C. This carbon remains in the bcc lattice upon rapid cooling cycles and can have pinning effects on the dislocations [86, 89]. Therefore, both the temper-aged ferrite and tempered martensite are responsible for the YPP in DP and martensitic steels.

With significant microstructural changes in SCHAZ (YPP was only observed in this region), the effect of tempering on both the ferrite (temper-aging) and martensite (tempering) and the amount of free carbon and mobile dislocation density have to be considered in a unified fashion. Phenomenological models for the YPP can be used to study the variation of dislocation density in the microstructure. The model introduced by Hahn [92], as shown with its parameters in Figure 16, is one model that uses the dislocation density as the main parameter for generating stress-strain curves with YPP. We used this model to generate the stress-strain curves corresponding to those obtained from tensile testing experiments.

The corresponding curves for the tensile testing samples with the lowest and the highest YS are plotted in Figure 16 along with curves for SCHAZ

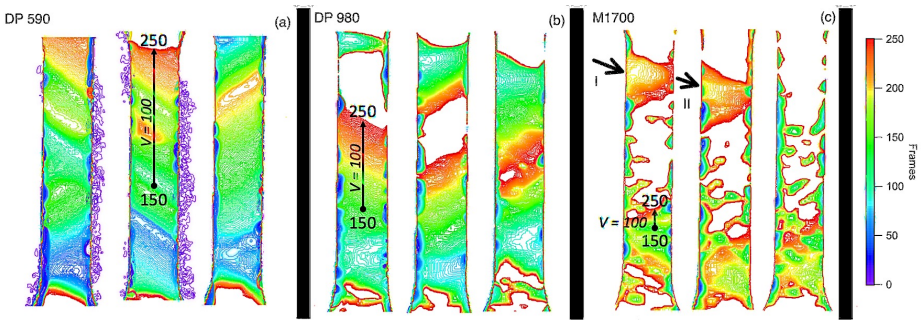

Figure 4-16: Contour of localized strain trajectories for DP590, DP980LC, and M1700 samples, subjected to thermal cycles with a peak temperature of 650 °C, at strain of 0.01 and as a function of time. The Lüders band motion and numbers of initiation sites increase from DP590 to M1700. The rapid motion, multiple Lüders band initiation sites, and cross-width band motion are remarkably higher in M1700. Frames correspond to time intervals of 0.1 second.

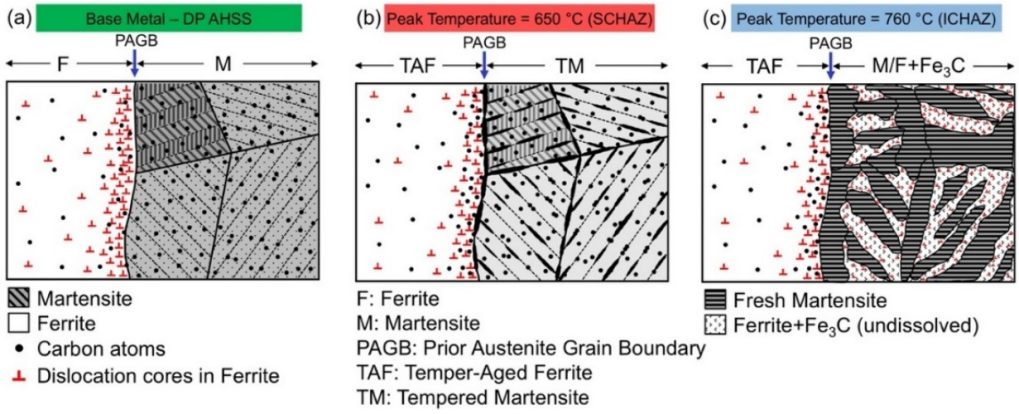

Figure 4-17: Schematic illustration of microstructural evolutions occurring during thermal cycles of spot welding of DP AHSS steels with peak temperatures of 650 and 760 °C, corresponding to SCHAZ and ICHAZ, respectively. For the fully martensitic steels, events in martensite phase can be adopted and therefore, no separate schematics are needed.

samples. The dislocation density for these two curves is also shown and indicating that the dislocation density in the steel's microstructure changes due to the thermal cycles with different peak temperatures. Although these types of models formed based on fitting of experimental data can be used for other materials however due to numerous variables, there is no unique solution. Thus, this type of models cannot effectively represent the YPP for different size-scales. The above sensitivity analyses show that these two parameters (carbon and dislocation density) can vary remarkably in different peak temperatures and reflect on the plastic instabilities seen in the thermally simulated samples subjected to peak temperatures belonging to SCHAZ of DP and martensitic AHSS. The appearance of plastic instabilities and Lüders band in the mechanical behavior of the SCHAZ and ICHAZ regions may lead to high degree of uncertainties and plastic instabilities in the behavior of the AHSS spot welds.

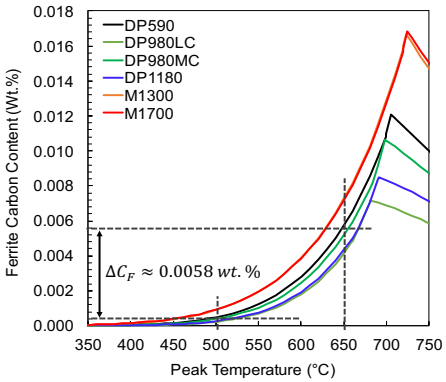

Figure 4-18: The amount of carbon that can dissolve in ferrite in equilibrium as a function of peak temperatures. Carbon solubility in ferrite increases with an increase in peak temperatures. Slight reduction above a maximum value at high temperatures above 700°C is indeed expected due to the on-set of the austenite formation.

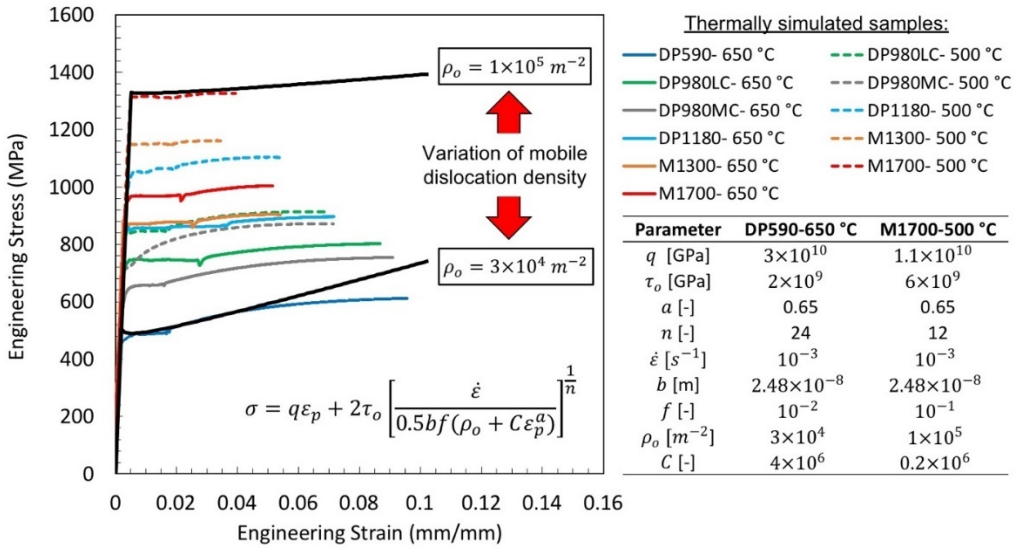

Parameter	DP590-650 °C	M1700-500 °C
q [GPa]	3×10^{10}	1.1×10^{10}
τ_o [GPa]	2×10^9	6×10^9
a [-]	0.65	0.65
n [-]	24	12
$\dot{\varepsilon}\ [s^{-1}]$	10^{-3}	10^{-3}
b [m]	2.48×10^{-8}	2.48×10^{-8}
f [-]	10^{-2}	10^{-1}
$\rho_o\ [m^{-2}]$	3×10^4	1×10^5
C [-]	4×10^6	0.2×10^6

Figure 4-19: Variation of dislocation density based on fitting a phenomenological model proposed by Hahn [92]. In this model: σ is the plastic stress, q is the macroscopic work hardening coefficient, τ_o is the resolved shear stress, b is the burger's vector, $\dot{\varepsilon}$ is the strain rate, ρ_o is the initial mobile dislocation density, f is the fraction of initially mobile dislocations, ε_p is the plastic strain, and a, C and n are dislocation density parameters from experiments. A wide range of mobile dislocation density was used in the fittings.

4.5 Summary

The effect of thermal cycles with different peak temperatures due to spot welding process on the local constitutive properties and plastic instabilities of several DP and martensitic AHSS were investigated. Following conclusions can be made based on the results and analyses:

Significant softening, in terms of hardness change, was observed in both SCHAZ and ICHAZ regions of spot welded samples. The extent of softening was similar in these regions in areas close to Ae1 phase transformation temperature of each steel. The lowest and highest extents of softening were observed in DP590 and M1700, with hardness ratios of 0.94 and 0.58, respectively.

Interestingly, the minimum yield stress ratio (YS_{Local}/YS_{BM}) was observed in the ICHAZ regions heated to a peak temperature between Ae1 and Ae3 in all steels which may be the location for strain localization in some loading modes. This result is in contrast with existing understanding that the SCHAZ might be the site of strain localization.

Yield stress and tensile stress heterogeneities were observed in all steels with degradation of these properties in the softened HAZ (both SCHAZ and ICHAZ). The heterogeneity in these softened regions increased in higher strength steels with a higher fraction of martensite in their microstructure.

Discontinuous yielding in the form of yield point phenomena with corresponding Lüders band was observed in SCHAZ of all steels. The Lüders strain in each steel increased with the peak temperature and was related to the carbon content of the tempered martensite. The magnitude of the Lüders strain was shown to be inversely related to the carbon content of martensite.

The formation of Lüders band and its propagation was different in different steels. In higher strength steels, more initiation sites and cross-width propagation were observed.

5 Uncertainties in Finite Element Simulation of Yield Point Phenomena in Advanced High Strength Steel Spot Weld

5.1 Introduction

Results from tensile testing of dual-phase (DP) and martensitic advanced high strength steel (AHSS) samples subjected to heat-affected-zone (HAZ) thermal cycles below the Ae1 temperature, presented in Chapter 4, revealed the existence of discontinuous yielding in the form of yield point phenomena (YPP). These samples were subjected to typical HAZ thermal cycles with peak temperatures ranging from 500 to 650 °C. The formation of YPP and its corresponding yield plateau and Lüders strain have been studied by many researchers [85, 89, 91, 94-96] and it has been shown that the Lüders strain is sensitive to concentration of carbon, ferrite volume fraction and grain size, temperature, and strain rate. It is indeed well known that the YPP behavior is manifested in steels due to the reduction in dislocation motion with the presence of Cottrell atmosphere, i.e., segregation of carbon atoms in dislocations [85, 86, 91, 97, 98]. It is interesting to note that the FE simulations of spot welds until now has not considered the YPP behavior in the HAZ regions and forms the motivation of the study presented in this chapter.

The first step towards addressing this gap is to implement material constitutive model capable of describing YPP. Literature review indicates that there are many approaches to capture the YPP behaviors in FE simulations. The first approach is based on phenomenological models that is based on carbon concentration, dislocation density, multiplication, and velocity parameters [92, 99-102]. The second indirect method is based on developing a calibrated material model that

faithfully reproduces the tensile testing result with yield point phenomena. This methodology relies on modifying constitutive properties (i.e. stress-strain relations) of the FE elements to be represented by Upper Yield Stress (UYS), Lower Yield Stress (LYS) and strain hardening rate [99, 101]. Interestingly, Schwab and Ruff [99] calibrated the UYS and LYS based on the measured angle of Lüders' band with reference to loading axis using digital image correlations (DIC) and the onset of yield point (from measured stress-strain curve). After this calibration, it is assumed that this elemental material model would be able to exhibit a yield plateau for any other testing conditions or complex geometries. The effect of YPP on deformation behavior of steel tubes was studies by Hallai et al. [103, 104]. This is perhaps the most complex geometry for which material model with YPP included is used up to date. In this work, they used a rate dependent material model with YPP with UYS and LYS at the onset of Lüders strain and the initiation of strain hardening part of the stress-strain curve, respectively, obtained from the uniaxial tensile testing.

The application of the above material models with YPP included has not been extended to complex parts with heterogeneous material distributions and geometrical nonlinearities as that of. In addition, the effect of the YPP on the local and global plastic instabilities has not yet been studied, to the knowledge of author of the student. With the observation of the YPP in the HAZ of DP and martensitic AHSS spot welds, this becomes important to include such complicated material model in FE simulations with the aim to investigate possible impacts on loading response and instabilities, in both the local and global aspects. Therefore, the motivation of this work is to investigate the effect of this phenomena and its corresponding Lüders strain on the mechanical performance of spot welded samples made from DP and martensitic advanced high strength steels. With the difficulties in experimentally investigating the local and global effects of the YPP on mechanical performance of spot welded samples, the

numerical analysis using finite element method (FEM) become the candidate for this study. This chapter is structured as follows. The first section is dedicated to the FEA simulation methodology and materials constitutive models. In the next section, an overview of the published experimental data from TS samples are presented that are relevant for validation of FE simulations. Next, results from FE simulations and sensitivity analyses on material model, fracture criteria, and mesh design are presented and compared with experimental results. Finally, the implications of the simulations and the role of YPP on the overall performance of the spot welds are discussed.

5.2 Simulation Methodology and Validation Experiments

5.2.1 Development of Local Constitutive Material Models

Data Generation: The M1700 fully martensitic steel with 0.31 wt.% carbon, 0.47 wt.% manganese, and 0.19 wt.% silicon was used in this study. Results shown in previous chapters showed that this steel experiences significant microstructural changes during spot welding process depending on the local peak temperature. Results showed the onset of yield point phenomena in samples subjected to SCHAZ conditions with peak temperatures of 500 °C and 650 ºC. In this work results obtained from tensile testing on Gleeble simulated HAZ samples were used as material model input for FE simulations. Details for the Gleeble simulations and tensile testing can be seen in Chapter 4. To extract element scale constitutive properties for different regions of spot weld, a virtual extensometer with 1-mm length was used in post-processing of DIC data. The results from these measurements in the form of true stress-strain curves are shown in Figure 5-1. Each curve was then assigned to corresponding section of the HAZ of spot weld in FE models for TS and CT sample.

Generation of Material Model with Yield Point Phenomena: In this work we adopted the method introduced by Schwab and Ruff [99] for generating the

element-scale material models with YPP included. This method uses the observed yield stress and Lüders angle in tensile testing of samples in the DIC measurements to calculate the UYS and LYS to describe the element-scale material behavior for FE simulations. Details for this model can be found in Ref. [99]. The UYS and LYS are then calibrated until the stress-strain curve from FE simulation of UT sample matches with experimental observations. Typical values for these two parameters for SCHAZ regions are summarized in Figure 5-2. Results from our DIC measurements showed that the Lüders band front angle may change during propagation in the gauge length resulting in changes in calculated UYS and LYS. For example, for sample subjected a peak temperature of 650 °C this variation was measured to be around 10 degrees. These results show that by changing the Lüders angle from 50 to 60 degrees, the LYS and UYS change by -23% and +18%, respectively.

In our calibrated YPP model (CYPP), a Lüders angle of 56 degrees was used. To

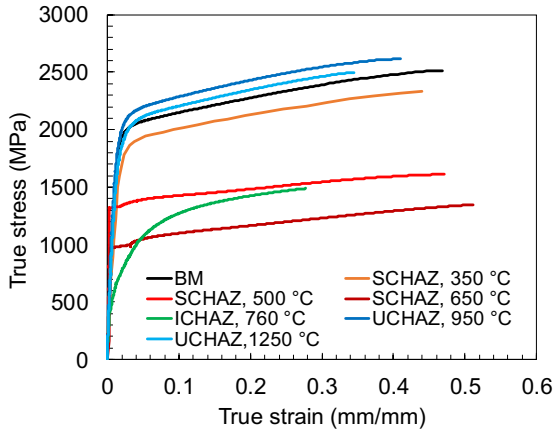

Figure 5-1: Local elastic-plastic properties obtained from thermally simulated samples representing the local properties of M1700 spot weld used in FE simulation of uniaxial tensile testing and TS and CT tests.

investigate the sensitivity of this parameter, we choose an upper limit of 60 degrees. The calculated UYS and LYS were found to be 1112 and 904 MPa, respectively. Similar calibration was performed for the tensile data from samples subjected to a peak temperature of 500 °C. The UYS and LYS were calculated to be 1425 and 712 MPa, respectively. For material at 500 °C, the UYS and LYS were calculated to be 1723 and 1090 MPa, and 1918 and 959 MPa, for CYPP and EYPP, respectively.

With above sensitivity to the Lüders band front angle, three different material models, including: (1) model without YPP (NYPP), (2) model with calibrated YPP (CYPP), and (3) model with exaggerated YPP (EYPP) were considered as a part of sensitivity analysis for the SCHAZ region of weld in FE simulations of TS sample.

Damage Model: A strain-based stress-state and strain-rate independent

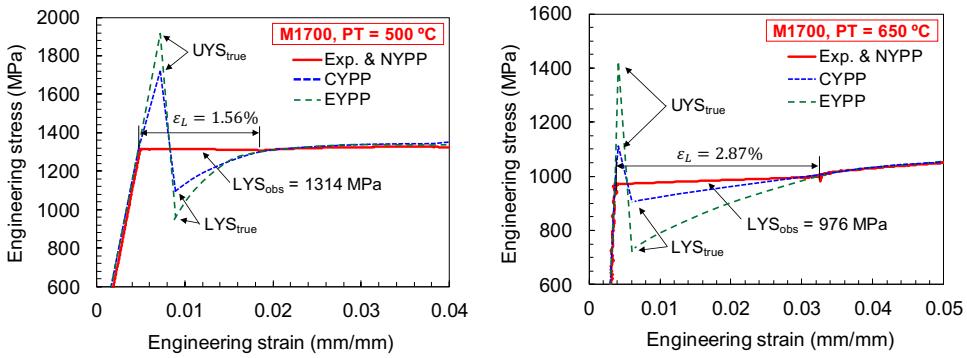

Figure 5-2: Three element-scale material models including NYPP, CYPP, and EYPP for M1700 at 500 °C (and 650 °C peak temperatures obtained from the method introduced by Schwab and Ruff [99]. Material models for CYPP and EYPP were calculated based on observed YS and variation of the Lüders angle in gauge length of UT sample.

constant fracture criterion was initially used in this study. Due to the complexity ofthe strain and stress fields and as explained later in this chapter, a stress-based damage model based on the tensile failure at integration point of the elements was used in conjunction to the strain-based model. The equivalent fracture strain at failure for each peak temperature was derived from post-processing of DIC data during tensile testing and used in FE simulation of TS sample as the damage model. For all regions but the SCHAZ with peak temperatures of 500 and 650 °C, a stress-based failure criterial was used in conjunction with the strain-based model. This, as explained later in this chapter, was to account for the conditions in which the UYS in SCHAZ at 500 and 650 °C reaches values above the tensile strength of the adjacent regions.

5.2.2 Finite Element Analysis

FE models: Three-dimensional FE models for the UT and TS (with 4- and 8-mm nugget diameter) tests were generated in Abaqus commercial FE package. The geometry and boundary conditions were in concert with the requirements suggested by ASTM E8 [105] and AWS D8.9 standards [50]. These models are shown in Figure 5-3. For the UT sample, the entire geometry was modeled, however for the TS sample, only one half of geometry was modeled, due to the symmetry. The FE model for UT was mainly to calibrate the material models for different peak temperature, particularly for material at 500 and 650 °C with YPP. These calibrated material models as mentioned above were used as element scale material inputs for different regions of spot welds during the simulation of TS sample.

Mesh design: The meshing was performed by using eight-node linear brick elements. The element size for UT model was the average of that used in SCHAZ at 500 and 650°C and comparable to the length of virtual extensometer (1 mm) used to extract the strain history from DIC data. The element sizes

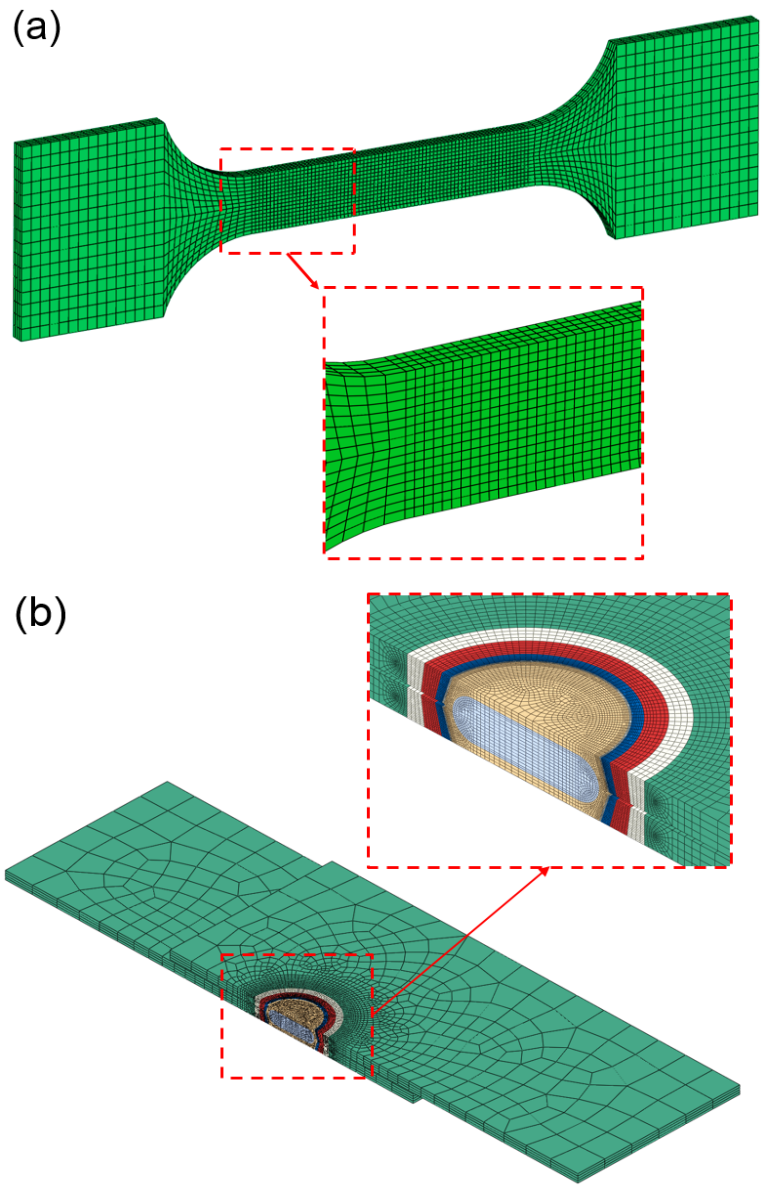

Figure 5-3: Three-dimensional FE models prepared in Abaqus for uniaxial tensile (a) and Tension-Shear (b) samples. The TS sample was partitioned into sections representing different regions of the spot welded sample. A closer look at partitioning, mesh, and material assignment can be seen in Figure 5-4.

ranged from 30 μm in SCHAZ to 3 mm in regions close to the two ends of TS model.

Special attention was paid to the mesh design for the complex geometry of spot weld such that enough number of elements are assigned to each region of weld based on the overall geometry and expected deformation (see Figure 5-4). The element deletion technique was used to describe the crack initiation, propagation, and failure in TS samples. A mesh refinement analysis was performed to investigate the sensitivity of results to element size by increasing the number of elements from around 130k to 270k.

FE solver options: Two FE solvers can be used for solving the quasi-static loading condition in UT and TS tests; (i) the implicit (computationally intensive) quasi-static solver and (ii) dynamic explicit (less computationally intensive) solver. The latter is usually suggested for solving problems that include

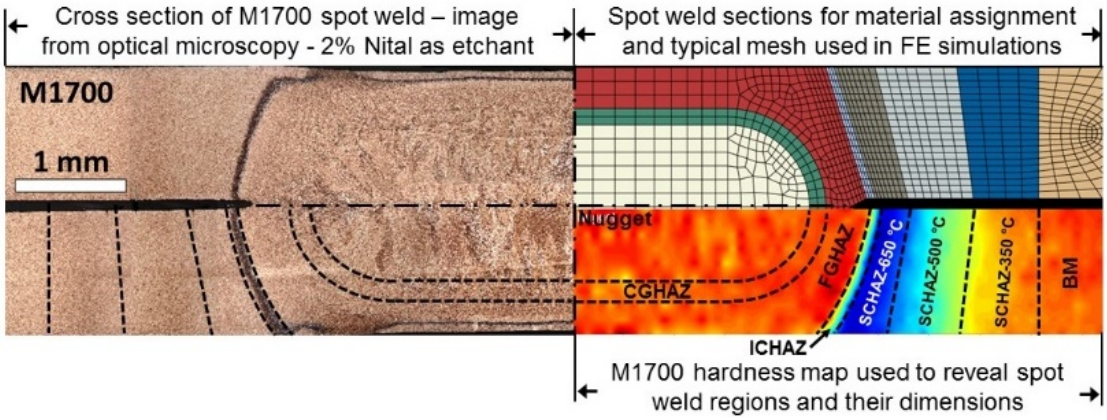

Figure 5-4: Image from optical microscopy of cross-section of M1700 spot weld. A 2% Nital etchant was used to reveal the microstructure. Results from hardness mapping are also shown in addition to FE model partitioned for material assignment.

nonlinearities in both geometry and material properties, large deformations, failure and fracture modeling. However, with several parameters in the dynamic loading (mainly mass and time scaling, and damping factors), the justification of the results becomes important. In this work we initially used the implicit solver for the TS model with CYPP material and ran the simulation. The computational time for this solver was about two days with difficulties in finishing the simulation due to large deformation, nonlinearities, and fracture model. The explicit solver, on the other hand, was able to solve the same problem in about three hours. This could be expected as the implicit solver needs a series of iterations to establish the equilibrium condition between the elements while the explicit solver does not seek the equilibrium condition and directly solves the nodal accelerations. The computationally intensive inversion of the stiffness matrix and the decrease in time step size is another reason responsible for the longer solution times. More details on the differences between these two solvers is out of the scope of this work and reader is referred to literature, for examples Ref. [106-109]. A similar simulation time was used for both the solvers with a mass scaling of 40 for the explicit solver to reduce the computational time. The results from the explicit solver were noisy, in terms of amplitude of oscillations in loading response. Therefore, numerical filtration was needed to obtain results comparable to that from implicit solver. The current work details our calculations based on the explicit solver only.

Material assignment to spot weld regions: The FE models for TS sample was partitioned into 9 sections, each section representing one peak temperature used in Gleeble thermal simulations. These sections were including the base metal (BM), 3 sections in SCHAZ (350, 500, 650°C), ICHAZ (760°C), UCHAZ (950°C, corresponding to FGHAZ), UCHAZ (1250°C, corresponding to CGHAZ), and nugget (above melting temperature). Each true stress-strain curve shown in Figure 5-1 was then assigned to its corresponding partition in FE models. For the

nugget the same material as CGHAZ was assigned as it was not practical to reproduce this region in Gleeble simulator. Figure 5-4 shows a detailed view of above partitions along with the microhardness map and mesh design on the cross-section of sample. For two sections in SCHAZ with peak temperatures of 500 and 650 °C, three different material models, i.e. NYPP, CYPP, and EYPP were used, as explained in previous section.

The results from FE simulations using these material models for 500 and 650 ºC were compared with those from experiments, as presented in next section.

5.2.3 Overview of Validation Experiments

As detailed in previous chapters, TS samples were prepared by welding two sheets of M1700 steel with the same thickness of 1.6 mm and using welding parameters resulting in 4- and 8-mm nugget diameters. Sample dimensions and mechanical testing procedures were followed as per AWS D8.9 standard [110]. An MTS Criterion C45 tensile frame with constant displacement rate of 2 mm/min were used for loading the samples and results were recorded in form of load-extension for comparison with results from FE simulations.

The mechanical testing on UT samples were performed using the same displacement rate. Microstructural analysis on failed TS samples were also performed using the scanning electron microscopy to capture the local deformations.

5.3 Results

5.3.1 Simulation Results for Uniaxial Tensile Testing

Results from FE simulation of UT sample for the peak temperature of 650 °C are presented in Figure 5-5. The material model (shown in Figure 5-2) with CYPP material model used in FE simulation was able to predict the stress-strain curve

with the YPP and its corresponding observed YS and Lüders strain comparable to those observed in UT experiments. Results for UT sample at 500 °C also showed that the material model with YPP is able to generate similar stress-strain curve similar to that of experiment. In both samples, i.e. 500 and 650 °C, the Lüders band nucleated from one end of the gauge length (Figure 5-5-1) and propagated through the entire gauge length (Figure 5-5, 1-4). The strain hardening stage was then started followed by plastic strain localization and failure in the gauge length (Figure 5-5, 5-6). The Lüders angle from FE simulation for SCHAZ-650 °C was measured (see Figure 5-5 (c)) to be 56±2 degree (depending the location in gauge length) which was comparable to that from experiments; 58±3 degree. Finally, the results from UT experiments did not show a UYS for 500 and 650 °C. This can be related to several factors including slight misalignments of sample in tensile testing (however below standard specified range), small scratches, residual stresses, and heterogeneous material distribution in tensile samples as can be expected for tempered DP and martensitic microstructures. With the material models being calibrated to predict the YPP in the UT samples, FE simulation of TS samples were implemented.

5.3.2 Simulation Results for Tension-Shear Test

Results from FE simulations of TS samples with 4- and 8-mm nugget diameters are presented in Figure 5-6 along with those from experiments. As explained in the previous section, three YPP models (NYPP, CYPP, and EYPP) and two damage models (with and without TFC) were used in FE simulations.

Oscillations in load-displacement curve: Although the experiments show only slight oscillations in load-displacement curves, results from FE simulations show significant oscillations, particularly in higher levels of load close to the peak value. The extent of the oscillations increases with the transition of calculations moving from NYPP to CYPP and EYPP material models. A comparison between the peak load in TS samples, shows a slight increase in the peak load for

samples with EYPP in which the UYS and LYS were changed by +18% and -23%, respectively, with respect to the CYPP. The difference between peak loads for NYPP and CYPP is not noticeable. To understand the local and global deformation behaviors in the TS sample a closer analysis is needed. This can be done by plotting the equivalent plastic strain (PEEQ) at various stages of global deformation and on the cross section of the weld (Figure 5-7). Only the results from simulations using CYPP material model was presented because there were not any noticeable differences in strain distribution contours.

Based on these observations, the equivalent von Mises stress, σ_{vm}, will be used later in this study for comparisons. From Figure 5-7 for the TS samples, the strain localization initiated in ICHAZ as denoted by point (a). With further increase in global deformation, the plastic strain propagates into the SCHAZ where material models for peak temperature of 650 °C were assigned to elements. This is followed by first instabilities in the form of YPP in these elements (point a and b). With small Lüders strain for elemental material models (see Figure 5-1 and

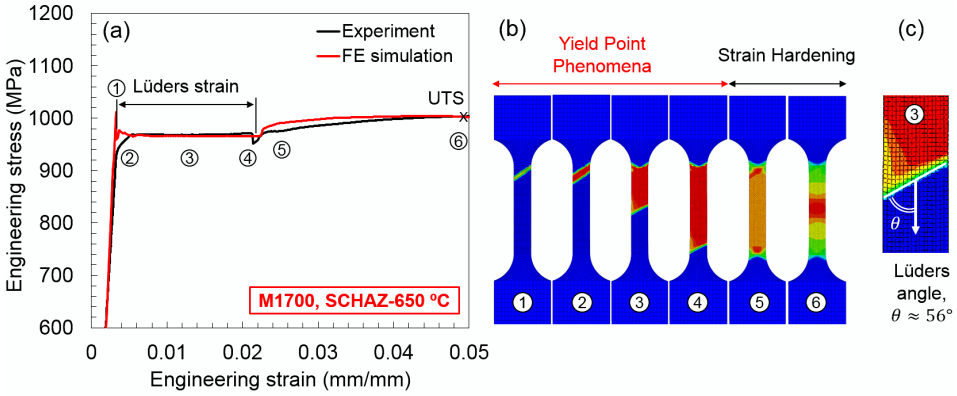

Figure 5-5: Results from the FE simulation of uniaxial tensile testing was used to calibrate the material models with YPP for peak temperatures of 500 and 650°C. Results shown for 650 °C uniaxial tensile sample.

Figure 5-2), the transition between YPP and strain hardening occurs with a slight increase in global extension (0.05 mm for TS). With further increase in global extension, the strain hardening initiates in the same elements and at global extensions of 0.5 mm. At extension of 0.5 (point d), the crack initiates in the ICHAZ region and grows as global extension increases. From this point onwards, small oscillations in load are observed with high magnitudes of oscillations with simulation of CT

testing. As mentioned earlier, the range of oscillations in both TS increase from NYPP to CYPP and finally EYPP material model. Interestingly, the first two models show the same range of oscillations. Finally, simulations suggest that the failure in all samples initiates and propagates in the ICHAZ region.

Stress heterogeneity and application of stress-based damage criteria:

Results from strain distribution presented in earlier section did not show

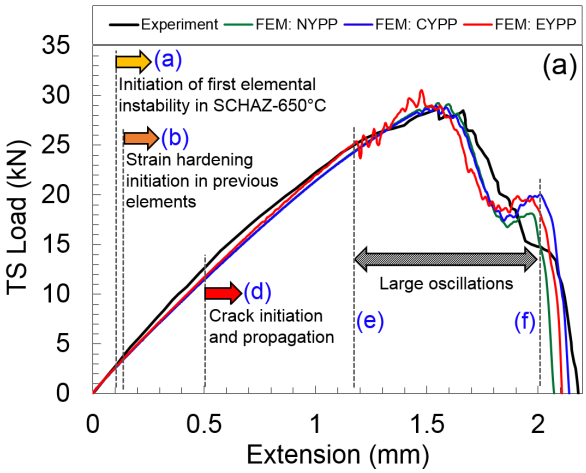

Figure 5-6: Results from FE simulation of TS sample with 8 mm nugget diameter for material models including: NYPP, CYPP, and EYPP. For CYPP FE simulations with and without a Tensile Failure criterion were performed.

noticeable differences in models with different YPP material models. This could be expected as the difference between YPP material models is in the existence and level of stress at a certain strain (also NYPP has no UYS and LYS). Therefore, we used the calculated heterogeneous stress distributions (equivalent von Mises stress, σ_{vM}) in this section for comparisons. Figure 5-8 depicts the heterogeneous stress distribution at different global extensions from FE simulations of TS model. The heterogeneous stress distribution starts in SCHAZ-650°C and then extends to the SCHAZ-500 °C, as the global extension increases. Interestingly, the extent of stress heterogeneity increases with transition from NYPP to CYPP and then EYPP material models.

Perhaps the most important observation from these results is the existence of the heterogeneous stress distribution in ICHAZ (while material for this region did not show YPP in Gleeble simulations). This condition can be related to the fact that in a continuum domain, the loads and thus the stresses can transfer to adjacent regions. In addition, the stress levels in ICHAZ showed values above its UTS. This indicated the need to use a stress-based failure criterion, TFC, in conjunction with the strain-based damage criteria. Results from application of this conjunct damage model are presented in Figure 5-9 and Figure 5-10 with results from experiments for TS sample with nugget diameters of 4 and 8 mm. Three factors are used to compare these results: (i) local deformation and necking, and (ii) the failure mode. The two typical types of failure in these spot welds are the interfacial failure (IF) occurring in the UCHAZ and nugget, and the plug failure (PF) that takes place in HAZ. Figure 5-9 shows the results from FE simulation of TS sample with a 4 mm nugget diameter with CYPP material model. The results from experiments are also included with micrographs from the failed samples. As illustrated, the failure mode from experiments (9c) and FE simulations (9b) by only using the strain-based damage model resulted in FIF failure (b and c) while the FE model with TFC (9a) resulted in PF-ICHAZ failure (a). The comparison of

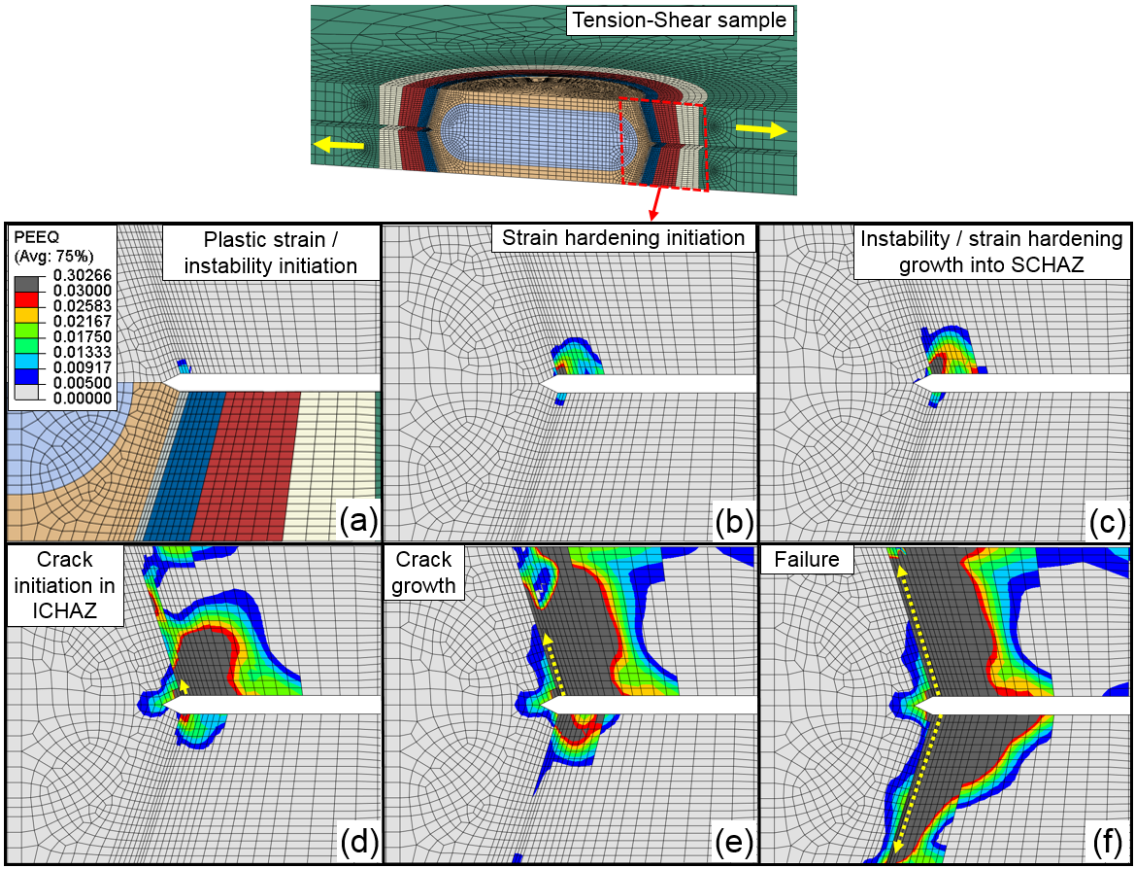

Figure 5-7: Evolution of equivalent plastic strain in TS sample: (a) initiation of plastic strain and instability from ICHAZ, (b) strain hardening initiation in the same region, (c) growth of plastic strain and instabilities into SCHAZ, (d) crack initiation in ICHAZ, (e) crack propagation in through the sheet thickness in ICHA, and (f) failure of TS sample from ICHAZ. The deformation scale is set to zero in above figures.

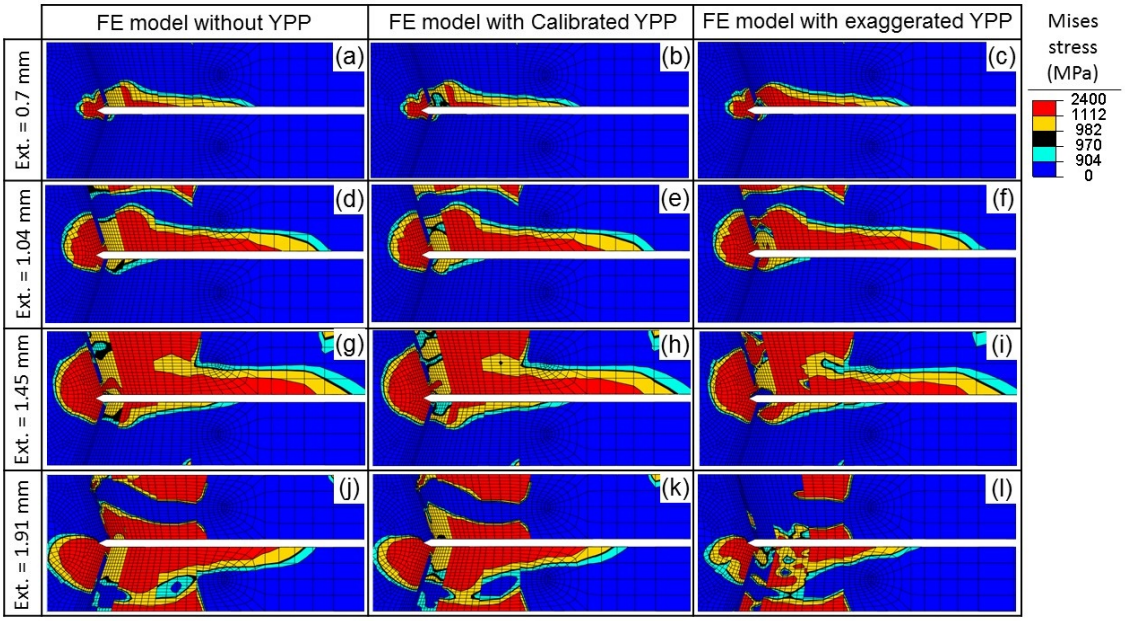

Figure 5-8: Heterogeneous stress distribution in the HAZ of TS sample obtained from FE simulations show the oscillation and alteration of stress in SCHAZ region of the weld. Three material models for SCHAZ were used in FE simulations.

local deformation and necking is not applicable to this sample since the failure mode is different. In addition, the UCHAZ and nugget completely separate from the TS sample in the model with conjunct damage model where the TFC was added.

Similar method was used to compare the results for TS model with 8 mm nugget diameter. Figure 5-10 presents the results for TS sample with an 8 mm nugget diameter. Results are more interesting here. While the failure mode is the same (PF-ICHAZ), the local deformations and necking are significantly different. In model without TFC, the necking in HAZ < Ae3 is evident with about 20% of reduction in the cross section of region. These value match well with results from experiments (14% and 24%). The same value for the model with TFC was significantly lower and about 4%.

5.4 Discussions

5.4.1 Oscillations in Global Loading Response

Results presented in previous section showed the existence of load oscillations in results from FE simulation of TS models, for all the YPP models. The largest oscillations were observed in regions close to the peak load in the both type of samples. This emergence of large load oscillations can be explained by considering the fraction of the material involved in plastic deformation and also the YPP material model as the crack revolved around the nugget axis. This is shown in Figure 5-11. With increase in the amount of material that involves in plastic deformation and YPP, the effect of material model, especially the difference between the UYS and LYS, becomes important. This resulted in increase in amplitude of load oscillations by moving from NYPP to CYPP, and then EYPP. This can be also the reason for seeing larger oscillations in UT samples than in TS, as in the UT samples the entire cross section of the sample in involved in YPP simultaneously. The heterogeneous and repetitive alteration

and fluctuation of stress in the SCHAZ can have detrimental impact on simulation with complex geometries that may experience both fatigue and impact loading conditions, which is the focus of the future work. Other factor influencing the magnitude of the oscillations is the mesh design. This is explained later in this section.

5.4.2 Uncertainties in FE Simulations of YPP

The study of local deformation and plastic instabilities with the characteristics explained in the previous sections stresses the need for characterization techniques that are able to measure such phenomena with proper resolution. In this study we used FEM for investigating the local and global phenomena, however, there are several uncertainties in the results from FE simulations. In this part of this study we discuss some of these uncertainties relevant to the FE simulation of YPP. Figure 5-12 presents summaries these uncertainties.

Material model for YPP*:* The calculations for UYS and LYS were done based on the phenomenological model by Schwab and Ruff [99]. These material parameters were calibrated by using the experimental results from uniaxial tensile testing sample that represent a certain loading condition. Several studies have shown the dependency of Lüders strain to the geometry of the sample, strain rate, temperature, and stress state [92, 95, 98, 101, 102, 111].

In addition, fracture models, mesh design and element size can also affect the results from FE simulations, particularly the load oscillations, as shown in this study. In this study, a strain-based fracture model was used with no dependency to stress state, strain rate and temperature. This could result in uncertainty of the results from the FE simulations and is indicative of the need for developing material models for YPP with above dependencies included. In addition, such dependence needs to be considered in experiments and for both the extraction of local properties and material models, as well as in TS tests.

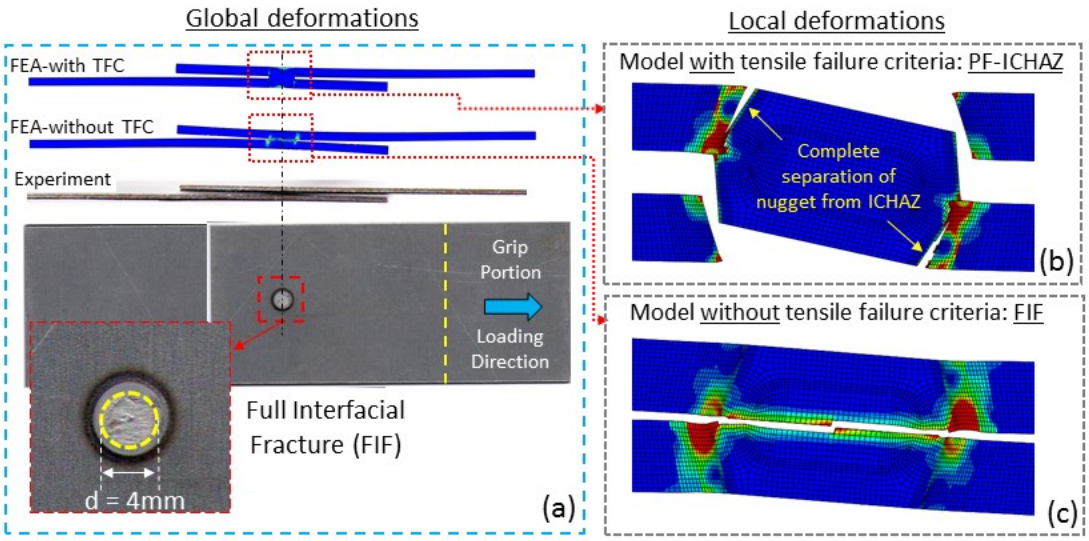

Figure 5-9: Results from FE simulations and experiments for TS sample with 4 mm nugget diameter show that the use of tensile failure criteria can lead into incorrect results. The failure mode from experiments and FE simulations with only strain-based damage model resulted in FIF failure (b and c) while the FE model with TFC resulted in PF-ICHAZ failure (a).

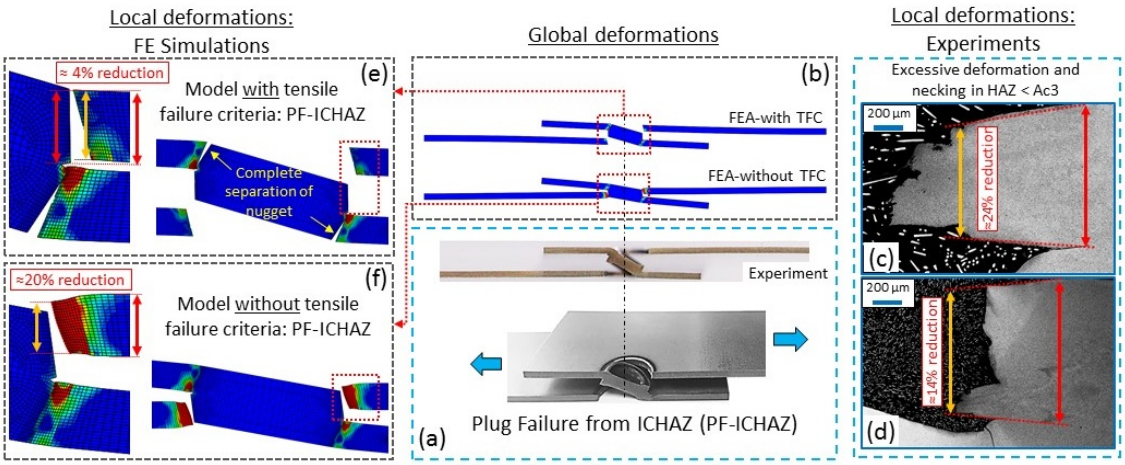

Figure 5-10: Results from FE simulations and experiments for TS sample with 8 mm nugget diameter also show that the use of TFC can lead into incorrect results. Although the failure mode is similarly occurring in ICHAZ, however, the local and global deformations are significantly different. The model without TFC, shows results similar to those from experiments with comparable necking and local deformations, as shown in (a, b, d, e, and f).

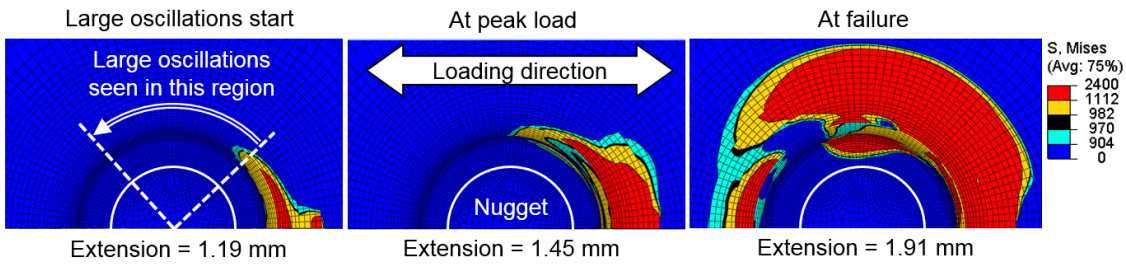

Figure 5-11: The initiation and growth of equivalent stress from front side to the other side of the spot weld. The element size in loading direction changes from 0.03 to 0.2 µm affecting the deformation behavior observed at peak load in deformation curves from FE simulations.

Another uncertainty related to the FE modeling of YPP is regarding the homogeneity of nucleation and growth of Lüders band in the gauge length of the UT sample or in the specific region of the part. This can promote the Lüders band front velocity and thus decrease the local material's Lüders strain. Results Chapter 4 showed that both homogeneous and heterogeneous nucleation can occur in the simulated HAZ samples. The complexity of such problems in which the microstructural characteristics can affect the nucleation and propagation of Lüders band under various loading conditions requires more advanced FE methods such as crystal plasticity finite element method (CPFEM) which is out of scope of this work however needs to be considered for an effectively descriptive FE model for YPP.

Fracture criteria: Results from application of different damage models in FE simulations presented in Figure 5-9 and Figure 5-10 showed that including the YPP in material model results in stress heterogeneity in HAZ and more importantly increase of stress in ICHAZ to value above its UTS, when the material model with EYPP was used. This led into the need for a stress-based damage model and as a result, the TFC was added to the damage model enabling the damage model to initiate damage and failure in this region.

The results from this conjunct damage model, however, showed that the predicted deformation and failure in TS model do not match with the results from experiments. Therefore, although a stress-based failure criterion with value equal to the UTS of local material was used, the results from such criterion do not match with the observations from experiments and application application of such failure criteria for models needs to be investigated in the future work.

HAZ partitioning and material model assignment: In this work a step-wise partitioning technique was used for assigning material models to the of spot weld in TS sample. This HAZ partitioning is usually done in welded samples and based on the number of peak temperatures that were used to reproduce the local

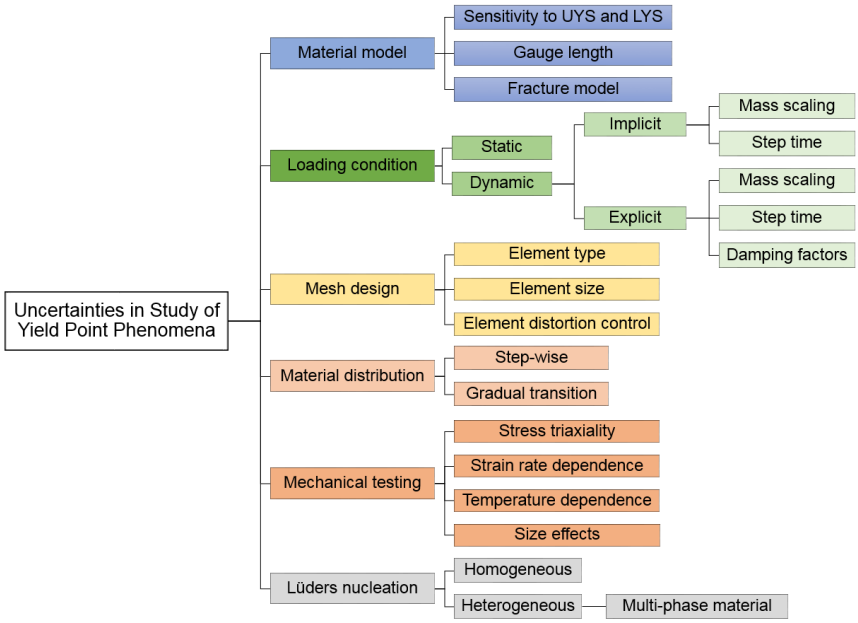

Figure 5-12: Uncertainties in the study of yield point phenomena and its effects in deformation behavior of welded samples.

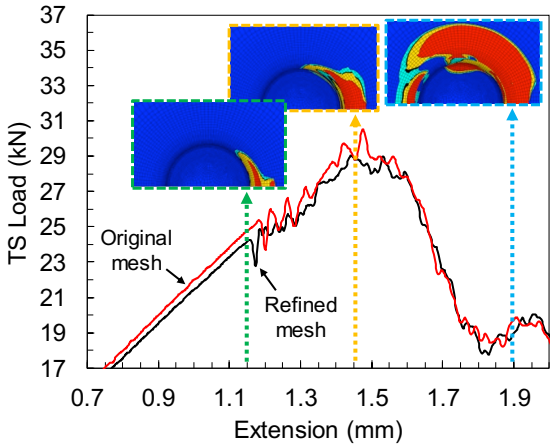

Figure 5-13: Mesh sensitivity analysis revealed the effect of element size on the oscillations observed in loading response. Results are presented for TS FE model with EYPP material input.

material in Gleeble simulations. Therefore, it can be expected that the discontinuous transition of material and number of partitions for HAZ affect the strain localization and local plastic instabilities in the SCHAZ of TS samples and generally in models with gradual transition in material properties.

Mesh design and element size: The fracture models have strong dependency to the mesh design and element size therefore a special attention needs to be paid to the mesh design and element type. Results from a sensitivity analysis on element size performed in this work (see Figure 5-13) showed that, mesh design and element size in combination with the fracture models can influence the amplitude of load oscillations. This needs to be considered when interpreting the results from FE simulations, especially when fracture models are used in combination with material models with YPP included.

5.5 Summary

In this study, experimental and computational approaches were used to investigate the effect of YPP on the deformation behavior and plastic instabilities in TS samples made from M1700 AHSS. Several uncertainties relevant to the material model with YPP and FE simulation technique were considered. Following conclusion can be made from these studies:

- Local and global instabilities in the form of load oscillations were observed in the deformation behavior of both TS samples with nugget diameters of 4 and 8 mm. The local instabilities were in the form of stress heterogeneities in SCHAZ were input elemental material was assigned with YPP included and showed dependency to YPP model and its corresponding UYS and LYS.
- Global instabilities in loading curves were related to the material model with YPP, mesh characteristics, and FE solver options. Studies on these factors showed several uncertainties relevant to FE simulation of YPP in AHSS spot welds.

- The amplitude of load oscillations was similar in result from experiments and those from the FE simulations with NYPP and CYPP. The EYPP showed oscillations significantly larger than those from experiments, NYPP and CYPP. This was related to the difference between UYS and LYS used in the material model, with a direct correlation.
- Results from FE simulations showed large oscillations in load, in regions close to the peak load. The magnitude of the oscillations in this region showed increase from NYPP model to CYPP model and then EYPP. This was related to the difference between the UYS and LYS in the YPP material models as well as the variation of element size and aspect ratio. Another factor affecting the amplitude of oscillation was the element size used in region where in the crack initiates and propagates.
- A stress-based failure criterion (TFC) was added to the damage model to capture the failure due to the increase of stress in ICHAZ to value above the UTS. Results from this model showed pre-matured semi-brittle abrupt failure from ICHAZ for both the 4 and 8 mm nugget diameters. The local and global deformation and necking was also significantly different when the stress-based model was added to damage model. Although this model showed the possible failure from this region, the results did not match with those from experiments and added another uncertainty to the FE simulation of YPP in spot welds.
- With several uncertainties in the FE simulations stemmed from material dependency to loading condition, strain rate, temperature, and length scales, this can be concluded that current material models for YPP for application in FE simulations are still primitive with respect to the material scale, rate dependency, and stress state.

6 The Individual Role of Weld Geometry and HAZ Softening on Mechanical Performance of AHSS Spot Welds

6.1 Introduction

With the new regulations for the automotive industry to produce greener cars, steel makers have been focused on designing new generation of steels known as advanced high strength steels (AHSS) to reduce the weight and fuel consumption and increase the safety of cars. Dual-phase (DP) and Martensitic (MS) steels are among the AHSS that are widely used in manufacturing of chassis and body of the cars in automotive industry. Resistance Spot Welding (RSW) is the main joining technique in manufacturing of the parts made from these steels. DP and MS steels have a ferritic-martensitic and fully martensitic microstructures, respectively. Although martensite is a hard microconstituent with high levels of tensile strength (up to about 2800 MPa) however it has a metastable structure and decomposes into ferrite and carbide during the RSW in a phenomenon known as martensite tempering in temperatures below the Ae1 phase transformation temperature of steel, as extensively studied by several researchers [3, 12-14, 16, 18, 19, 63]. Results presented in Chapters 3 and 4 on this work also showed that constitutive properties are heterogeneous throughout the DP and MS spot welds, depending on the initial microstructure and carbon content of the steel. In addition, the HAZ softening was observed in both ICHAZ (due to formation of fresh ferrite) and SCHAZ (due to tempering of martensite) in all the steels with different extent increasing from DP590 to M1700.

The deformation and failure behavior of the spot welded samples has been investigated in several studies [40-42] and it has been shown that the strength

and failure in spot welds in a function of the geometry of the spot weld and material properties. In these studies, failure type or mode in DP and MS spot welds are categorized into two main types of interfacial failure (IF) and round button (RB, also Plug Failure (PF)) failure. The failure location is different in these two. In interfacial failure, crack passes through the nugget of the weld on the faying surface of spot weld (fully interfacial failure, FIF), or initially moves on the faying surface and then deviates through the thickness of steel sheet and passes through the FGHAZ and/or CGHAZ. The second type of failure, i.e. RB failure, can take place in two regions of HAZ: (i) in softened HAZ (ICHAZ and SCHAZ), and (ii) in FGHAZ and CGHAZ. A combination of above failure modes can also occur in spot welds. In this chapter a combination of failure type and its location is used to describe the failure in the spot welds. This has been shown later in this chapter in Figure 6-3.

While the role of spot weld geometry on the strength and failure of spot welded samples is studied by several researchers, the individual role of spot weld geometry and HAZ softening has not yet fully understood. In this chapter, the local constitutive properties obtained from tensile testing and digital image correlation on Gleeble simulated HAZ samples are used as material input for FE simulations of TS and CT samples with three nugget diameters of 4, 6, and 8 mm. These descriptive FE simulations help to understand the local-global relationship in deformation behavior and failure of AHSS spot welds made form DP and martensitic AHSS and reveal the root cause of the nonlinearity seen in the strength of these welds (as shown in Figure 1-2). The results from these FE simulations are then compared with those from experiments for validation. This needs to be mentioned here that in this chapter and based on the results shown in Chapter 5 of this work, it is assumed that YPP has little to no impact on the global deformation and failure behavior of these steels and therefore, in this

chapter material models without calculated upper and lower yield stresses were used in FE simulations.

6.2 Experimental procedure

6.2.1 Materials

Three grades of AHSS including DP590, DP980LC, and M1700 were used for this study. Chemical composition, initial microstructure and tensile properties for these steels are shown in Table 6-2 and 6-3, for comparisons. These three steels represent a wide range of carbon content and martensite volume fraction in their base metal.

6.2.2 Local constitutive properties and damage model

As comprehensively presented in Chapter 4, the thermal cycles due to resistance spot welding process results in heterogeneous made from DP and MS AHSS. These local constitutive properties are required for the FE simulations as material input. These local mechanical properties were obtained in Chapter 4 of this work from the mechanical testing on Gleeble simulated HAZ samples and the base metal for each steel and are presented in Figure 6-1 in form of engineering stress-strain curves, for comparisons. To predict the failure of the TS and CT samples there is a need to a damage model. In this work we use the equivalent

Table 6-1: Chemical composition, martensite fraction, and phase transformation temperature of the investigated steels.

Steel	*Alloying elements (Wt. %)*			C_M *(Wt. %)*	f_M *(Vol. %)*
	C	*Mn*	*Si*		
DP590	*0.09*	*0.99*	*0.284*	*0.441*	*16*
DP980LC	*0.10*	*2.19*	*0.65*	*0.154*	*59*
M1700	*0.31*	*0.47*	*0.19*	*0.31*	*100*

plastic strain (PEEQ) at failure as a strain-based damage model. It is assumed that the failure in model is not stress-state and strain-rate dependent and therefore a constant plastic strain failure is used in the FE simulations. To obtain the PEEQ at failure for each region of HAZ, a virtual extensometer with a length of 1-mm was in the strain measurements from DIC data. This was the smallest possible extensometer that could be used in DIC analysis based on the dimensions of the sample, resolution of DIC system, and experiment setup. The DIC equipment was manufactured by Correlation Solutions® and the VIC-2D post-processing software, was used for this purpose. For the nugget the same material properties as the FGHAZ-1250 °C was used as it was not practical to reproduce this region in Gleeble thermos-physical simulator. The plastic strains at failure for different regions of HAZ of spot welds made from the three steels of this study are presented in Table 6-3.

Table 6-2: As-received tensile properties for the AHSS used in this study.

Steel	***Thickness (mm)***	***YS (MPa)***	***UTS (MPa)***	***Total Elongation (%) (25-mm Gauge Length)***
DP590	*1.5*	*390*	*636*	*23*
DP980LC	*1.4*	*710*	*1056*	*13*
M1700	*1.6*	*1706*	*1876*	*5*

Table 6-3: Equivalent plastic strain at failure for different regions of HAZ of the steels used in FE simulations for the damage model.

Steel	*SCHAZ-350 °C*	*SCHAZ-500 °C*	*SCHAZ-650 °C*	*ICHAZ-760 °C*	*FGHAZ-950 °C*	*CGHAZ-1250 °C*
DP590	-	-	*0.95*	*0.86*	*0.08*	*0.06*
DP980LC	*0.61*	*0.68*	*0.72*	*0.45*	*0.07*	*0.06*
M1700	*0.46*	*0.64*	*0.61*	*0.34*	*0.07*	*0.05*

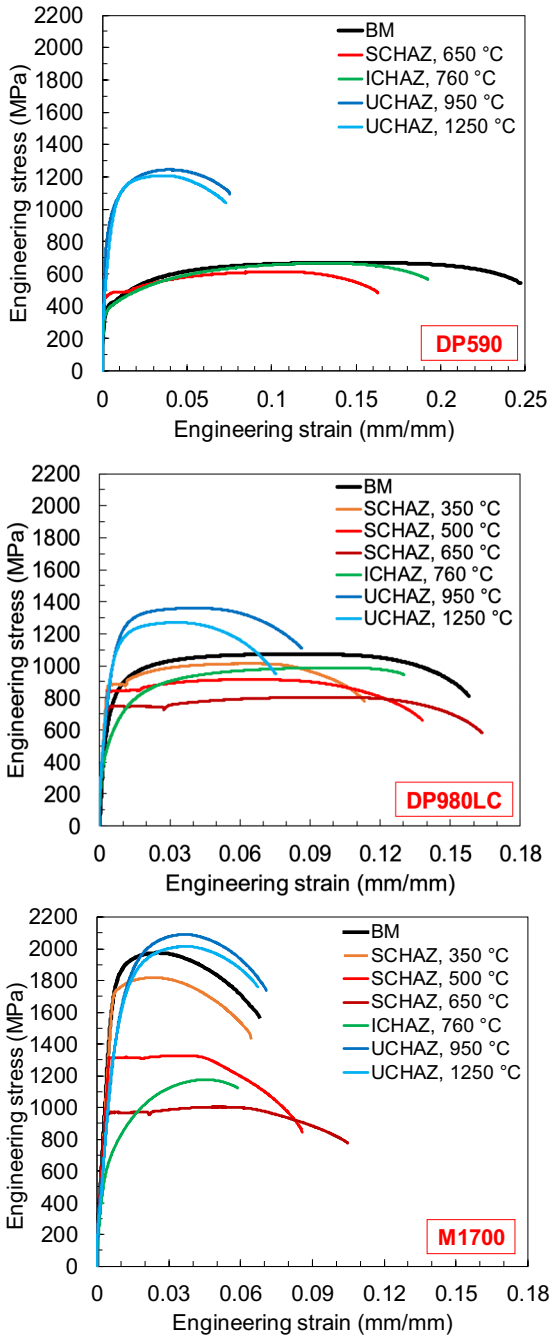

Figure 6-1: Engineering stress-strain curves obtained from tensile tests performed on base metal and Gleeble thermally simulated HAZ samples made from the three DP and MS AHSS used in this study.

6.2.3 Overview of Validation Experiments

As detailed in previous chapters, TS and CT samples were prepared by welding two sheets of the same steel and using welding parameters resulting in nugget diameters of 4, 6, and 8 mm. Sample dimensions and mechanical testing procedures were followed as per AWS D8.9 standard [110]. An MTS Criterion C45 tensile frame with constant displacement rate of 2 mm/min were used for loading the samples and results were recorded in form of load-extension for comparison with results from FE simulations.

6.3 Finite element simulations

Three-dimensional FE models for the TS and CT samples were prepared in Abaqus commercial FE package by following the specifications detailed in AWS D8.9 standard [50]. Due to the symmetrical geometry and to minimize the computational cost, only on half and one quarter of TS and CT samples were modeled, respectively. These models are shown in Figure 6-2 and Figure 6-3. As illustrated in Figure 6-3, the HAZ of the FE models for TS and CT tests were partitioned into several regions as following: BM, SCHAZ-350 °C, SCHAZ-500 °C, SCHAZ-650 °C, ICHAZ-760 °C, UCHAZ-950 °C, UCHAZ-1250 °C. This partitioning was done based on the number of tempering peak temperatures used in Gleeble simulations and for different regions of spot weld.

With a width of about 200 microns for the ICHAZ (depending on the distance between the Ae1 and Ae3 phase transformation temperatures of steel) and the existence of SCHAZ with three regions corresponding to three tempering peak temperatures (350, 500, and 650 °C), there is a need to design local meshes that are able to capture the deformations in these narrow regions with sharp transitions in constitutive properties. As a result, the meshing in both TS and CT models was done by using C3D8R elements with size ranging from 70 microns to 2 mm and at least 4 elements were used in the thickness of the steel sheet in

regions far away from the spot weld. Explicit FE direct solver was used in the FE simulations based on the complex geometry, large plastic deformations, and nonlinear material behavior with fracture models. Ductile fracture model and progressive damage were used in Abaqus to model the failure in parts. As explained earlier a constant equivalent plastic strain at failure was used and it was assumed that stress-state and strain rate do not change the strain at failure.

6.4 Results

Results from the FE simulations and mechanical testing on spot welded samples with 4, 6, and 8 mm nugget diameters are presented in Figure 6-4, for comparisons. The failure modes from the experiments and FE simulations are also reported in these figures. This must be noted that due to difference in the thickness of the steel sheets used in this study, results are normalized with the thickness of the sheet with the thickness of steel sheet thickness, as sheets ranged from 1.4 to 1.6 mm. While the FE simulations were able to predict the deformation behavior and failure mode for each sample, there were differences between the peak load (PL) and the extension at peak load (PLE) obtained from these simulations and those from experiments. This could be related to several uncertainties relevant to the experiments and FE simulations and is discussed in detail later in this chapter. The analysis of load-extension curves shown in Figure 6-4 showed that three sections can be distinguished in each loading curve: (i) initial linear section, (ii) nonlinear section with inclination of loading curve up to the peak load (PL), and finally (iii) the post-peak load (PPL) section. Two main PPL behavior can be seen in the TS curves: (i) complete drop of the load to failure which is related to the sudden brittle failure and corresponds to IF and RB-FGHAZ/CGHAZ, and (ii) gradual decrease in load as the global extension increases up to final complete failure which is related to progressive ductile damage and corresponds to RB-ICHAZ/SCHAZ.

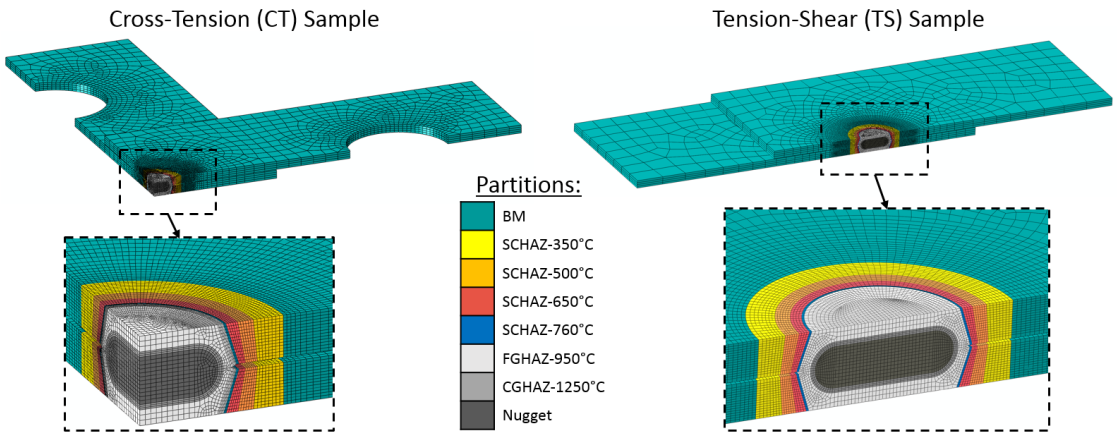

Figure 6-2: Finite element models for TS and CT samples with partitioned HAZ, material assignment, and mesh design. Due to the symmetrical geometry and for the sake of computational time.

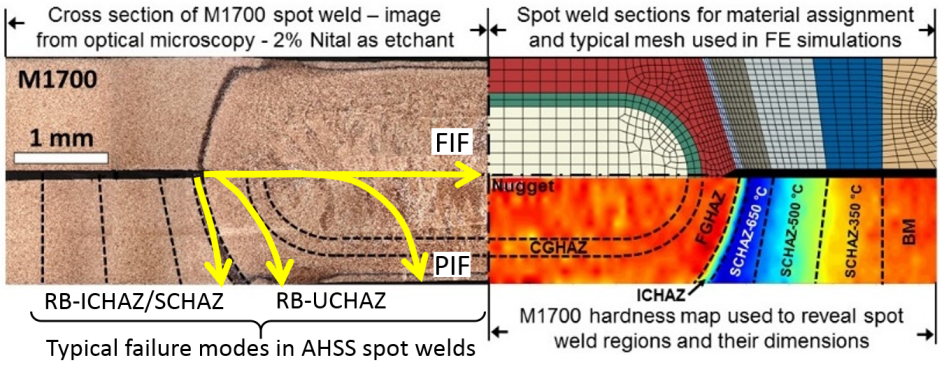

Figure 6-3: HAZ was partitioned into several regions based on the number of the tempering peak temperatures used in Gleeble thermal simulations. Results from hardness mapping are shown in addition to the mesh design and typical failure modes in AHSS spot welds.

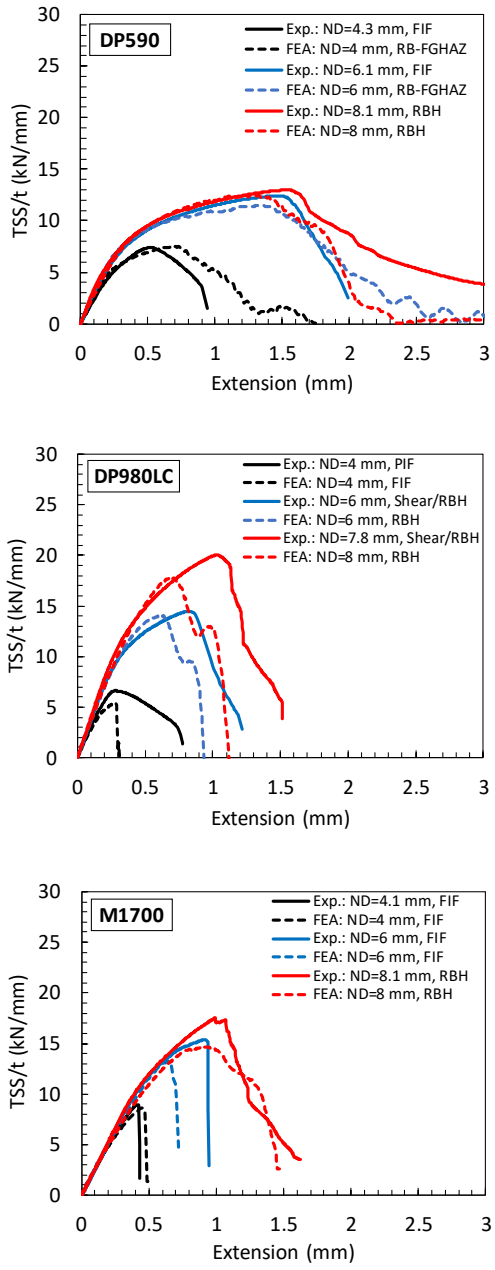

Figure 6-4: Results from experiments and FE simulations for DP590, DP980LC, and M1700 TS samples with 4, 6, and 8 mm nugget diameters. Failure modes are also shown in the legend of each plot.

The nugget diameter (ND) and the base metal tensile strength (BMS) also showed to have impact on the performance of the spot welded TS and CT samples. Figure 6-5 shows the normalized TS strength (TSS) and CT strength (CTS) as a function of ND and BMS. One general observation from these results is that the strength of both TS and CT samples increases initially with the nugget diameter and BMS up to certain values of (critical nugget diameter, ND_{cr}, and base metal strength, UTS_{cr}) and then decreases. This is interesting that the failure mode also changes at these critical values from the IF or RB-UCHAZ to RB-ICHAZ/SCHAZ.

From Figure 6-5 (a) and (c), the effect of nugget diameter on the strength of spot weld (TSS and CTS) can be seen. In general increase in nugget diameter leads to increase in TSS and CTS however the effectiveness decreases as the nugget diameter passes a critical nugget diameter in both TS and CT samples for all steels. The critical nugget diameter in all cases is around 6 mm, and it is interesting to note that the failure mode in TS samples changes at this nugget diameter, from FIF/Shear to RBH. For the CT samples a change in failure mode from RB to RBH is clear.

On exemption from this general rule is the TS sample for DP980LC for which the strength continuously increases with the same slope with the nugget diameter. It is important to notice that the failure mode does not change for this sample at the critical nugget diameter (around 6 mm). The drop in the strength for both the DP590 and M1700 is the same in Figure 6-5 (a).

Figure 6-5 (b) and (d) illustrate the normalized TSS and CTS as a function of the BMS, for nugget diameters of 4, 6, and 8 mm. As it can be seen it both plots for TS and CT samples, the nonlinearity increases in both the TSS and CTS with increase in nugget diameter, indicating the role of weld geometry on the nonlinearity.

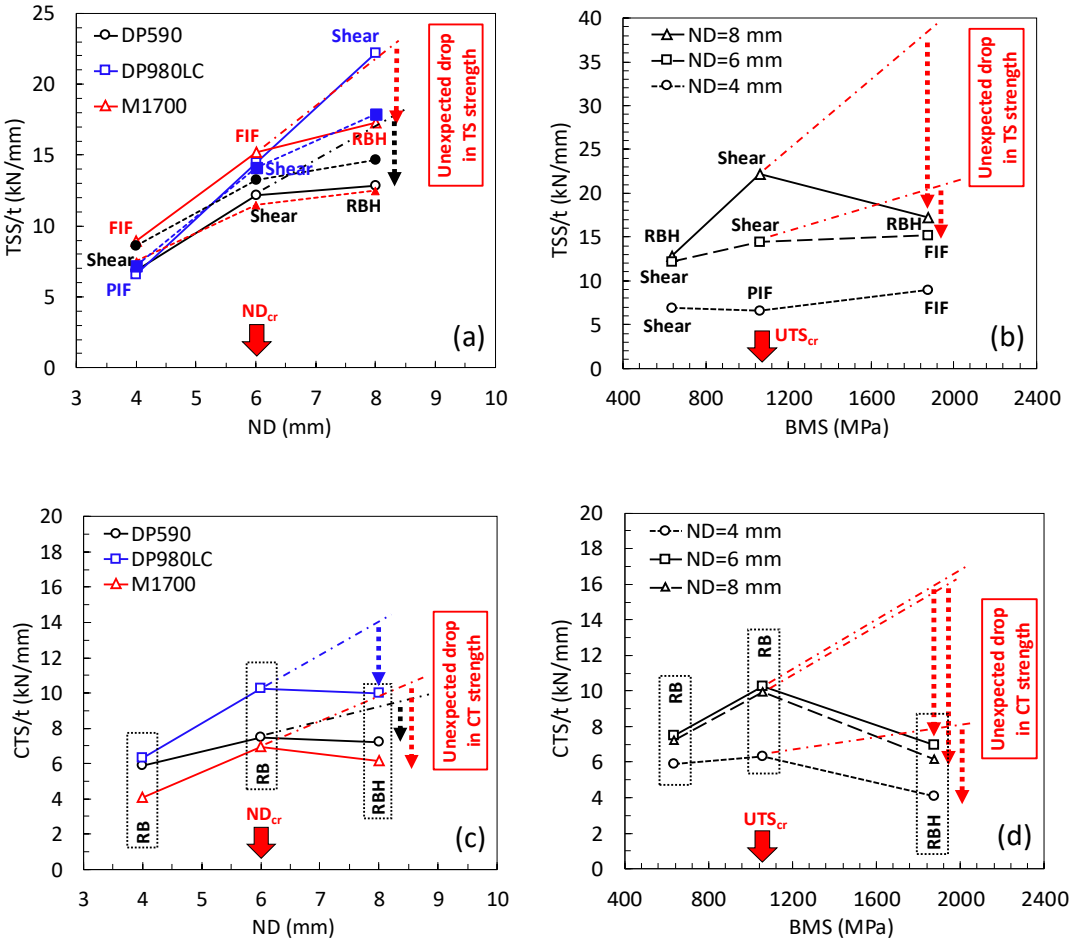

Figure 6-5: Experimental results from TS (a and b) and CT (c and d) samples made from DP590, DP980LC, and M1700 with three nugget diameters of 4, 6, and 8 mm. The initial martensite volume fraction for these steels are 16, 59, and 100 percent, respectively. Failure mode for each sample is also shown.

6.5 Discussion

Results presented in the previous section reconfirmed the existence of a nonlinear relationship between the BMS, and TSS and CTS in the DP and MS AHSS used in this study. These results showed that the nugget diameter (geometrical factor) and BMS (related to the chemical composition and initial microstructure of steels) have direct impact on the strength and failure behavior of these AHSS spot welds. In this section results from experiments and FE simulations are used to explain the above nonlinearity by considering the individual role of nugget diameter and material heterogeneity, with particular attention to the HAZ softening in ICHAZ and SCHAZ, in spot welds using a local to global approach.

6.5.1 Plastic strain evolution and failure path

Figure 6-6 shows the plastic strain localization, crack initiation and propagation and failure for M1700 TS samples with different nugget diameters. Only the cross section of the TS samples is shown. From this figure three different failure modes can be distinguished. For the nugget diameter of 4 mm although the initial plastic strain localization occurs in the ICHAZ, the growth of plastic strain in the notch tip of the weld reaches the plastic strain failure criteria and crack initiates from this point. By continuing the loading, the crack growth into the nugget and TS sample fails from the nugget with FIF failure mode.

The evolution of the plastic strain in different regions of spot weld (including notch, FGHAZ, ICHAZ, and SCHAZ) for this sample and other two samples with nugget diameters of 6 and 8 mm are presented in Figure 6-7 for comparisons. These results, in addition to those shown in Figure 6-8 can be used to understand the plastic strain concentration and evolution in the TS and CT samples made with different nugget diameters. As examples, results for M1700 for TS and CT models.

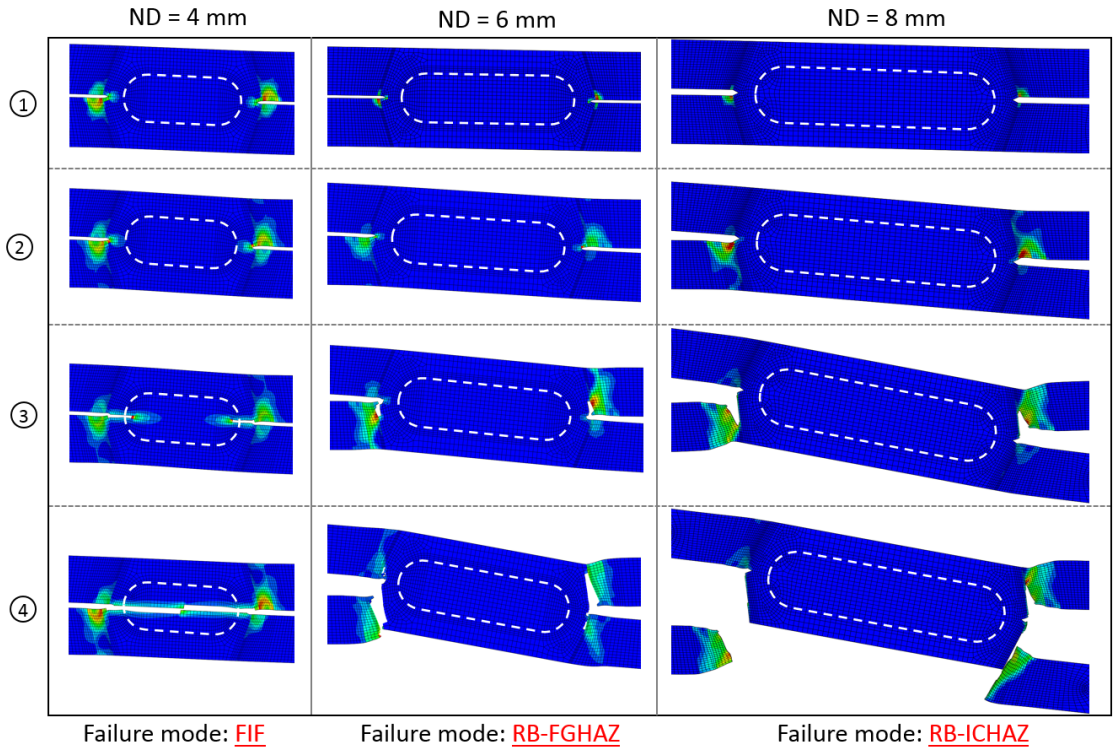

Figure 6-6: Results from FE simulation of TS test for M1700 spot welds with 4, 6, and 8 mm nugget diameters. The evolution and localization of the equivalent plastic strain on the cross section of samples show M1700 TS samples. Three failure modes were observed: FIF for ND=4 mm, RB-FGHAZ for ND=6 mm, and RB-ICHAZ for ND=8 mm. The main competition was observed between the ICHAZ and FGHAZ based on the strain localization, crack initiation, propagation, and failure.

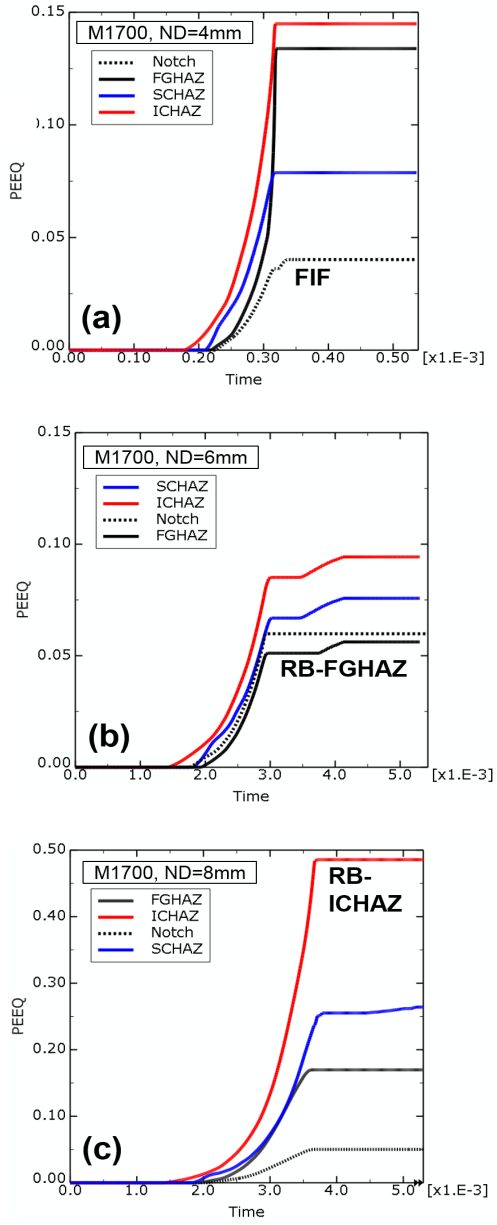

Figure 6-7: Equivalent plastic strain evolution in different regions of TS samples made from with 4, 6, and 8 mm nugget diameters. Note that in each plot, only one region reaches the failure plastic strain and failure and other curves never reach their failure strain levels.

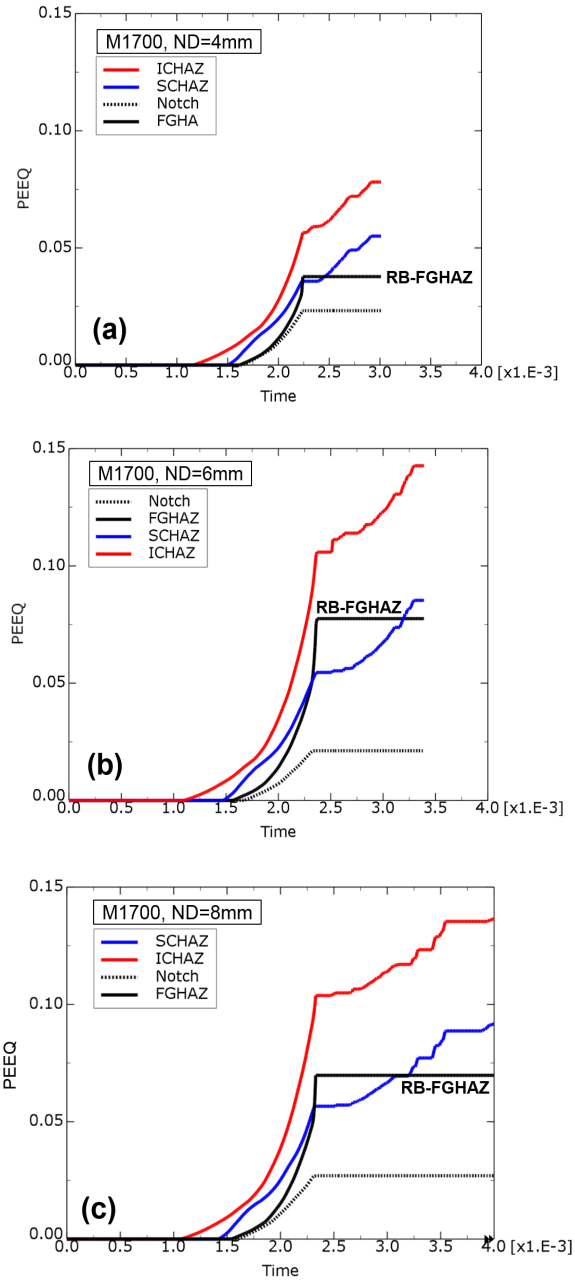

Figure 6-8: Results from the FE simulations of M1700 CT sample with 4, 6, and 8 mm nugget dimeters showing the evolution of the PEEQ in different regions of the HAZ on the cross section of CT sample.

6.5.2 The role of HAZ softening on spot welds performance

A new set of FE simulations was performed to investigate the role of HAZ softening that occurs in both the ICHAZ and SCHAZ on the performance of the TS and CT spot weld. The FE model for TS and CT samples with 8 mm nugget diameter and M1700 fully martensitic AHSS was selected for this investigation. The selection of steel and weld geometry was based on following: (i) the largest extent of softening was observed in this steel based on results shown in Chapter 3 and 4, and (ii) results from TS and CT experiments showed that the largest degradation in strength of spot welds belongs to this steel and when the nugget diameter is 8 mm. The methodology for this investigation is based on substituting the material properties for certain softened regions, i.e. ICHAZ and/or SCHAZ, in the FE model with that of base metal, simulating the condition that the HAZ softening does not happen in those regions. Based on this methodology, following cases (also shown in Table 6-4) were considered in this study:

- Case 1: Both ICHAZ and SCHAZ are included (similar to spot weld)
- Case 2: Softening do not occur in ICHAZ and material for SCHAZ-650°C is used instead.
- Case 3: Softening do not occur in SCHAZ and BM material used instead.
- Case 4: Softening do not occur in entire weld. BM material properties used for both ICHAZ and SCHAZ.

The strength (peak load, PL) of TS and CT samples (TSS and CTS) obtained from FE simulations for cases shown in Table 6-4 are presented in Figure 6-9, for comparisons. These results show that for both the TS and CT samples if there is not HAZ softening (both SCHAZ and ICHAZ) in FE simulations about 12% and 14% change (increase) in TSS and CTS can be expected. Considering the extensive softening that occurs in the M1700 (highest between the three steels used in this study) one can assume that the softening is not a dominant factor in

degradation of the AHSS spot welds. This however needs to be investigated for other steels, as done later for DP980LC in this section. This is also interesting that for the case in which ICHAZ was not considered (Case 2) the TSS and CTS showed 0.2% and 4.1% change, respectively. In general, and for M1700 it can be said that exclusion of either ICHAZ or SCHAZ from the FE simulations can lead to up to 15.5% increase in the strength of spot weld. Results presented in Figure 6-9 for M1700 TS and CT samples showed that the HAZ softening is not a dominant factor on the strength of M1700 spot welds and the geometry (nugget diameter) is the main factor.

Above behavior needs to be investigated for other steels as well. As an example, the same methodology was used for DP980LC to understand that if the HAZ softening has a similar role in performance of the spot welds made from this steel. The load-extension curves obtained from FE simulations for DP980LC and M1700 TS and CT sample are plotted in Figure 6-10, for comparisons. The results interestingly show that HAZ softening has a completely different role in different steels. While the role of HAZ softening was minor in M1700 spot welds

Table 6-4: Material assignment to different regions of the spot weld for studying the role of HAZ softening on spot weld performance.

	Material properties assigned to spot weld HAZ regions (ND=8mm)							
Case 1	CGHAZ-1250°C	CGHAZ-1250°C	FGHAZ-950°C	ICHAZ-760°C	SCHAZ-650°C	SCHAZ-500°C	SCHAZ-350°C	BM
Case 2	CGHAZ-1250°C	CGHAZ-1250°C	FGHAZ-950°C	SCHAZ-650°C	SCHAZ-650°C	SCHAZ-500°C	SCHAZ-350°C	BM
Case 3	CGHAZ-1250°C	CGHAZ-1250°C	FGHAZ-950°C	ICHAZ-760°C	BM	BM	BM	BM
Case 4	CGHAZ-1250°C	CGHAZ-1250°C	FGHAZ-950°C	BM	BM	BM	BM	BM

performance, it significantly impacts the strength (TSS and CTS) and extension at peak load (TSE and CTE) in DP980LC samples. In DP980LC, HAZ softening decrease the TSS and TSE by 44% and 32% and decrease the CTS and CTE by 31% and 36%, respectively. The same changes in M1700 were 12% and 42% increase in TSS and TSE, and 14% and 63% increase CTS and CTE. Therefore, while HAZ softening has a positive impact on the M1700 performance, it has a negative impact on DP980LC performance.

Results from FE simulations presented above for DP980LC and M1700 steels are combined with the experimental data for a range of DP and MS AHSS and shown in Figure 6-12, for comparisons. In this figure this is assumed that HAZ softening has a linear effect on the strength of DP and MS steels, meaning that in both the effect of HAZ softening increases with the extent of softening which was shown to be related to initial microstructure and carbon content of steels (see

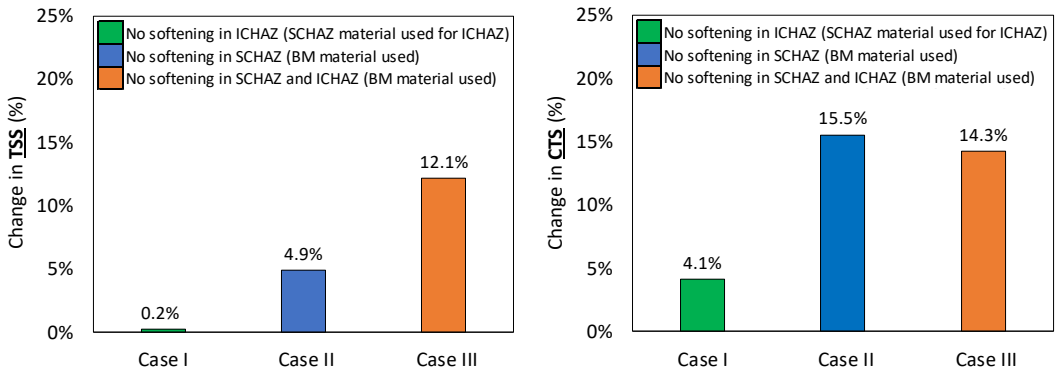

Figure 6-9: The change in the TSS and CTS when the SCHAZ and/or ICHAZ were not included in the FE simulations. Results show that exclusion of only ICHAZ has minimal impact on both TSS and CTS while the exclusion of either or both SCHAZ and ICHAZ can have up to 15.5% change (increase) in TSS and CTS.

Chapter 3 and 4 for details). This can be rationalized by considering the extent of HAZ softening and its role in the performance of the spot welds. For example, DP590 with 16% martensite in its base metal showed slight HAZ softening (only 6% drop in hardness, based on results presented in Chapter 3 and 4), and therefore a slight impact on the weld's strength can be expected. This is shown in Figure 6-12 by a small difference between the curve for spot welds behavior without HAZ softening and that with the HAZ softening (from TS experiments). DP980LC with 59% martensite in its initial microstructure however showed a higher extent of softening in HAZ (18% drop in hardness) and 44% drop in performance due to HAZ softening. Therefore, this can be concluded that the extent of HAZ softening is directly related to the initial microstructure of the steel, i.e. the martensite volume fraction in base metal.

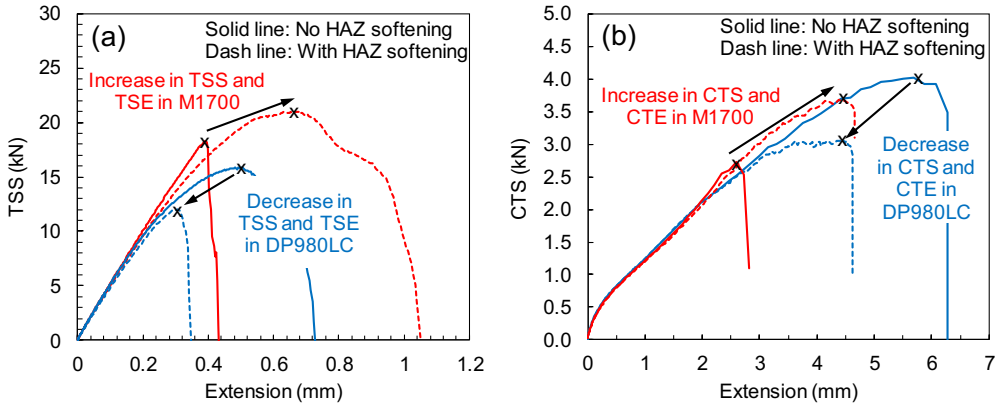

Figure 6-10: The effect on HAZ softening on TS and CT strength and extension for DP980LC and M1700 steels showed that the role of HAZ softening is complex and different in different grades of AHSS. While it deteriorates the performance of DP980LC spot welds it improves the performance of M1700 ones.

The drop in the performance of the DP AHSS spot welds can be related to the fact that the martensite acts as the hardening microconstituent in these steels and the HAZ softening significantly reduces its strength in regions close to the spot weld, resulting in a drop in peak load and global deformation of the spot welded sample. This however is different in MS AHSS, meaning that since in these spot welds the base metal has a semi-brittle behavior with low ductility (about 5% for M1700, for example), small global deformations can lead to high strain concentrations in range of failure strain of base metal resulting in crack initiation and failure occurring in UCHAZ. The occurrence of HAZ softening increases the ductility in the softening region (ICHAZ/SCHAZ) and allows for more deformation and energy absorption, and consequently increases the peak load for the spot welds made from MS AHSS. The strain localization and failure also occur in regions with more distance from the spot welds centerline. This is evident from the results from FE simulations shown in Figure 6-10 and Figure 6-11.

6.5.3 Uncertainties in FE simulation of AHSS Spot Welds

During the FE simulations and when comparing their results with those from experiments (TS and CT tests) differences between the peak load (PL) and extension at peak load (PLE) were seen. Figure 6-13 summarizes the differences between peak load measured from FE simulations and experiments. Steps were taken by adjusting the fracture strain for different regions of HAZ to calibrate the FE models so that results match better with the experimental work. However, with several sources of uncertainties in both the FE simulations and also the experiments, this seemed to be a tedious task and therefore FE simulations were used as descriptive models in this study.

Figure 6-13 shows that for both the TS and CT samples, as the nugget diameter increases the difference between the results from experimental and FE simulations increases. This is interesting to notice that larger nugget diameters

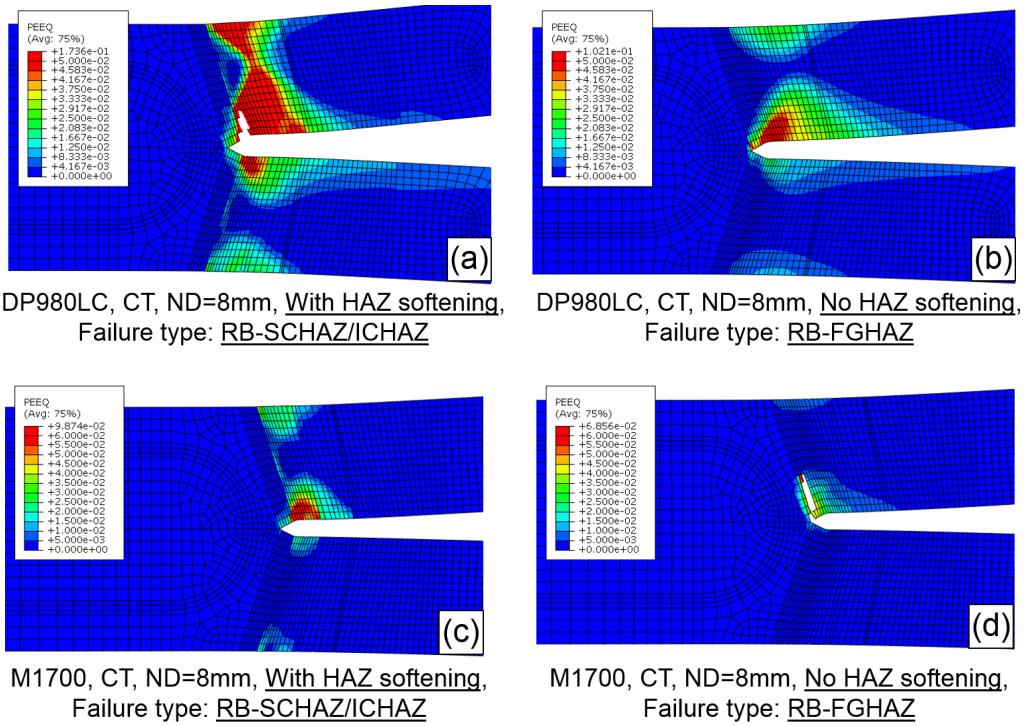

DP980LC, CT, ND=8mm, With HAZ softening, Failure type: RB-SCHAZ/ICHAZ

DP980LC, CT, ND=8mm, No HAZ softening, Failure type: RB-FGHAZ

M1700, CT, ND=8mm, With HAZ softening, Failure type: RB-SCHAZ/ICHAZ

M1700, CT, ND=8mm, No HAZ softening, Failure type: RB-FGHAZ

Figure 6-11: Equivalent plastic strain localization, crack initiation, and path on the cross section of CT sample made from DP980LC in (a) and (b), and M1700 in (c) and (d), with and without HAZ softening obtained from FE simulations. In DP980LC HAZ softening resulted in premature failure and in M1700 improved the weld strength. Local and global deformations and failure type and mechanisms were affected by existence of HAZ softening in this sample.

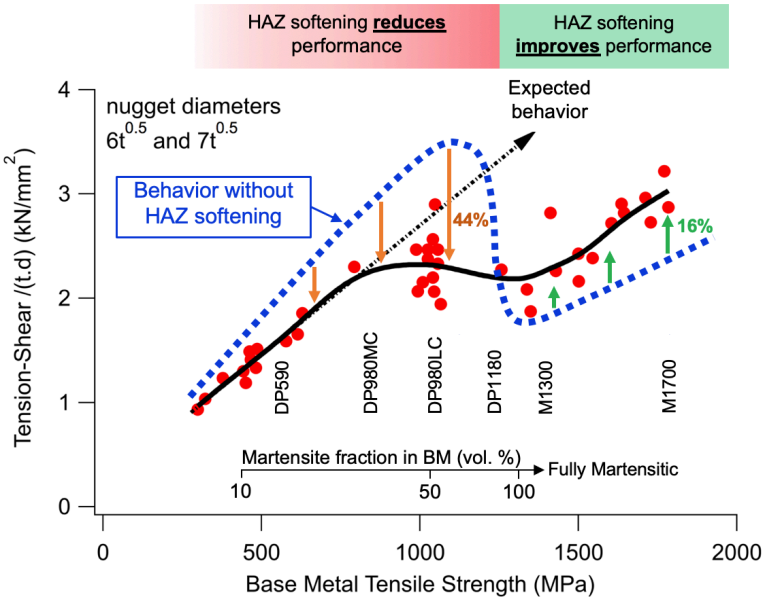

Figure 6-12: The complex role of HAZ softening on the strength of Tension-Shear samples made from DP and MS AHSS. While HAZ softening plays a strong role in strength of DP steels and can significantly reduce welds strength, for example by 44% in DP980LC sample, depending on the martensite volume fraction in initial microstructure, it has a minor role in strength of MS steels and improves welds strength by 16% in M1700 TS sample, as an example.

result in failure in the softened HAZ. In addition, the differences are larger in results for CT samples. To understand the underlying reasons or these differences there is a need to understand the uncertainties and assumptions relevant to both the experiments and FE simulations. Some of these uncertainties are listed in following:

- Material assignment to HAZ in FE models (continuous versus step-wise)
- Stress triaxiality and strain rate dependency of constitutive behavior and fracture strain
- TS and CT loading fixture and measurement techniques
- Existence of micro-cracks at the notch and voids on faying surface on spot welds
- Nugget size measurement

Several uncertainties are explained in more details in following:

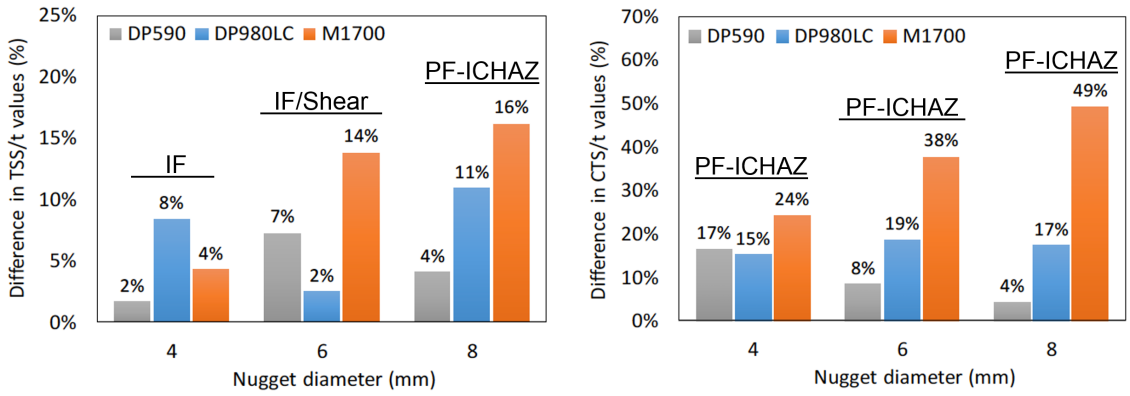

Figure 6-13: Difference between the peak loads measured from experiments and FE simulations for TS and CT samples with 4, 6, and 8 mm nugget diameter. The difference increases from DP590 to DP980LC and M1700 as the material heterogeneity and nugget diameter increase.

6.5.3.1 Material distribution in HAZ

While a continuous material distribution and gradual change between HAZ regions exist in the real spot welds, a step-wise method was used in the FE models for TS and CT samples (see Figure 6-2 and Figure 6-3). The used in step-wise method was due to partitioning of HAZ and the limited number of peak temperatures used in Gleeble simulations. By using the step-wise method, a constant material property is used for a region of HAZ that does not represent the real material distribution is spot welds. These can change the results from FE simulations and calibration techniques are needed to match the deformation behavior predicted from FE simulations with that from experiments.

6.5.3.2 Damage model and failure criteria

A constant fracture strain failure criterion was used in this study. This failure criterion was obtained from uniaxial tensile testing. Results from the work by many researchers have shown that the fracture strain is a function of the stress triaxiality and Lode angle [112, 113]. This can influence the crack initiation and propagation in the spot welded samples based on the local stress state (stress triaxiality).

6.5.3.3 Effect of micro-cracks and voids on faying surface of spot weld

Results from scanning electron microscopy on the cross section of spot welded samples (see Figure 6-14 as an example) showed the existence of micro-cracks at the notch where two sheets of steel are welded, and voids on faying surface of spot welds. To investigate the effect of these micro-cracks on spot welds performance, we included a crack with a length of 200 microns, as shown in Figure 6-14, typical to those observed in spot welds, and compared results with the model without this crack. Results from this analysis are shown Figure 6-15.

Result showed that including the micro-crack can have significant impact on the

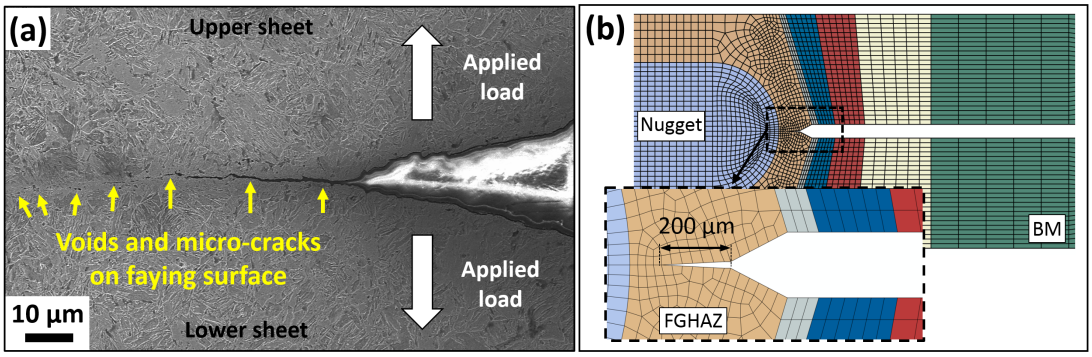

Figure 6-14: Results from scanning electron microscopy revealed pre-existence of micro-cracks and voids at the notch tip and on faying surface of the spot welds (a). FE model with and without crack at faying surface for M1700 CT with 4 mm nugget diameter (b).

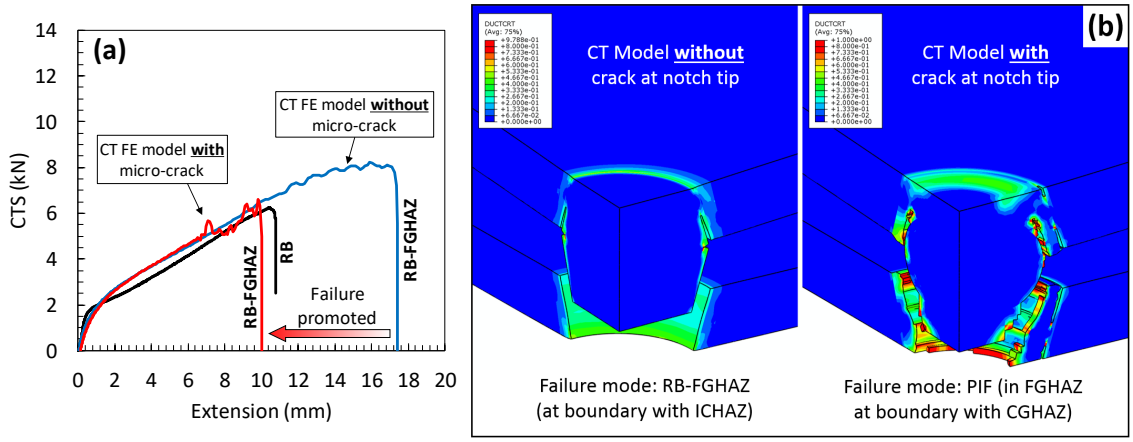

Figure 6-15: Results from FE simulation of M1700 CT sample with nugget diameter of 4 mm for the sample with and without micro-crack at the notch tip. Including the micro-crack to model resulted into 28% and 43% decrease in PL and PLE (a). This also affected the crack path to regions closer to the nugget for the sample with micro-crack (b).

CTS and CTE on the spot welds (here M1700 CT sample with nugget diameter of 4 mm). While the failure mode was RB-FGHAZ in both models, the crack initiation site and propagation path were different. In the model with the micro-crack, the crack moved towards the nugget and changed path when faced the CGHAZ and continued propagated on the boundary between the FGHAZ and CGHAZ. Therefore, although the failure mode did not change, the peak load and the extension at peak load in the model with micro-crack decreased by 28% and 43%, respectively. This significant change in results should be considered when comparing the results from experiments with those from the FE simulations, as a source of uncertainty.

6.6 Summary

Following conclusions can be made based on the results obtained from this study:

- Results from experiments and FE simulations showed that TSS and CTS does not increase linearly with the BMS or nugget diameter. Critical BMS and nugget diameter of 1000 MPa and 6 mm were detected as the values that the failure mode in both the TS and CT samples changes from a semi-brittle (IF and RB-UCHAZ) to a ductile failure (RB-ICHAZ/SCHAZ).
- The failure from ICHAZ has not been reported in literature. The lowest yield stress in this region, make it the site for plastic strain localization, crack initiation and propagation in the samples with larger nugget diameter (above the critical size). This was captured in the results from FE simulations.
- Results from experiments and FE simulations showed that the mechancial performance of AHSS spot welds is influenced by the weld geometry and the heterogeneous distribution of constitutive properties in the spot weld. The HAZ softening showed to have a complex role in performance of spot

welds. Results from FE simulatons showed that HAZ softening can play a different role in different grades of steels. It was shown that it can lead into degradation of DP980LC spot welds performance while improving M1700 performance.

- One interesting outcome from this study was the observation of minium yield stress in the ICHAZ. This suggest that improving the mechanical performance of the SCHAZ can not be effective without paying attention to ICHAZ. This also has to be noticed that the HAZ softening is beneficial in the performance of MS steels and there is no need to alleviate the HAZ softening in these steels.
- The uncertainties in experiments and FE simulations were shown to have significant impact on the peak load and extension at peak load of spot welded samples making it difficult to obtain an accurate assessment of spot welds performance in terms of peak load and extension at peak load from the FE simulations. These models however can help in understanding the local-global deformation and failure behavior, as well as the role of individual regions of the spot weld, as presented in this chapter.

7 Conclusions and Recommendations for Future Work

7.1 Conclusions

A comprehensive study was performed on the deformation behavior and failure of the AHSS spot welded samples. The role of heterogeneous material distribution and spot weld geometry was investigated by understanding the material-process-performance relationship and using a local-global approach. The effects of local thermal cycles typical to those in resistance welding process on the local microstructural evolutions and mechanical performance changes were investigated to rationalize the global deformation and failure behavior and explain the nonlinearity seen in the strength of AHSS spot welds. Results obtained from above study are concluded in below:

- Microstructural and mechanical evaluations on spot welds and Gleeble simulated samples showed that thermal cycles due to resistance spot welding can significantly change the local microstructure and mechanical properties, leading to a heterogeneous material distribution in AHSS spot welds. The extent of this heterogeneity was shown to be related to the initial microstructure and chemical composition of steels, as well as the experiences thermal cycle.
- A comparision between the yiefld stress values obtained from the microhardness scaling method and those from the Gleeble simulated HAZ showed that hardness scaling method in not effective in prediction the yield stress in the softened HAZ and overstimates the yield stress in this region of DP and MS AHSS spot welds.
- Significant softening, in terms of hardness change, was observed in both SCHAZ and ICHAZ regions of spot welded samples. The extent of softening was similar in these regions in areas close to Ae1 phase

transformation temperature of each steel. The lowest and highest extents of softening were observed in DP590 and M1700, with hardness ratios of 94% and 58%, respectively.

- Interestingly, the minimum yield stress ratio (YS_{Local}/YS_{BM}) was observed in the ICHAZ regions with experienced peak temperature between Ae1 and Ae3 in all steels of this study, suggesting this region to be the location for plastic strain localization and damage initiation. This result is in contrast with existing understanding that the SCHAZ might be the site of strain localization initiation.
- Yield stress and tensile stress heterogeneities were observed in all steels with degradation of these properties in the softened HAZ (both SCHAZ and ICHAZ). The heterogeneity in these softened regions increased in higher strength steels with a higher fraction of martensite and carbon in their microstructure.
- Discontinuous yielding in the form of yield point phenomena with corresponding Lüders band was observed in higher temperatures in SCHAZ of all steels. The Lüders strain in each steel increased with the peak temperature and was shown to be related to the carbon content of the tempered martensite and the peak tempering temparature. The magnitude of the Lüders strain was shown to be inversely related to the carbon content of martensite.
- The formation of Lüders band and its propagation was different in different steels. In higher strength steels, more initiation sites and cross-width propagation were observed.
- Results from implementation of YPP in FE models revealed local and global instabilities in the form of load oscillations in TS samples. The local instabilities were in the form of stress heterogeneities in SCHAZ when the

input elemental material was assigned with YPP and showed dependency to YPP model and its calculated UYS and LYS.

- Global instabilities in loading curves were related to the YPP material model, mesh characteristics, and FE solver options. Studies on these factors showed several uncertainties relevant to FE simulation of YPP in AHSS spot welds.
- Results from FE simulations showed the existance of large oscillations in load in regions close to the peak load of the load-extension curve. The magnitude of the oscillations in this region showed increase by moving from NYPP to CYPP and then EYPP and increase in the difference between the calculated UYS and LYS.
- A stress-based failure criterion was added to the damage model to capture the failure due to the increase of stress in ICHAZ to value above its tensile strength. Results from this model showed pre-matured semi-brittle abrupt failure from ICHAZ for both the 4 and 8 mm nugget diameters. The local and global deformation and necking was significantly different when the stress-based model was added to damage model. Although this model showed the possible failure from this region, the results did not match with those from experiments and added another source of uncertainty to the FE simulation of YPP in spot welds.
- With several uncertainties in the FE simulations of YPP in AHSS spot welds due to material dependency to loading condition, strain rate, temperature, and length scale, this can be concluded that current material models for YPP for application in FE simulations are still primitive and needs improvements.
- Results from Tension-Shear and Cross-Tension experiments and FE simulations showed that TSS and CTS does not increase linearly with the BMS or nugget diameter. Critical BMS and nugget diameter of 1000 MPa

and 6 mm were detected as the values that the failure mode in both the TS and CT samples changes from a semi-brittle to a ductile failure. The location of the failure also changed from the nugget with hard martensitic microstructure to the softened HAZ (mainly ICHAZ based on FE simulations).

- The failure from ICHAZ has not been reported in literature. With the lowest yield stress seen in this region this can be expected for this region to be the strain localization and failure initiation site.
- Results from experiments and FE simulations showed that the loading and failure behavior is influenced by the weld geometry and the heterogeneous distribution of constitutive properties in the spot weld. The HAZ softening showed to play a complex role in performance of spot welded sample. In DP AHSS it decreased the strength and global extension of TS and CT samples. In contrast, it played a different and minor role by improving the strength and global extension of MS AHSS.
- The uncertainties in experiments and FE simulations were shown to have significant impact on the measured peak load and extension at peak load in spot welded samples making it difficult to match the results from FE simulations with those from experiments.
- Results from this wrok showed that despite the current believe that HAZ softening leads into degradation of performance of AHSS resistance spot welds, the role of HAZ softening is in fact complex and different in different grades of AHSS. The results from this work can help the steel makers and automotive industry to better understand the role of HAZ softening in each steel grade and take proper action to improve the performance of the parts made from these steels.

7.2 Recommendations for Future Work

- Results from tensile testing on Gleeble simulated HAZ samples showed the existence of yield point phenomena (YPP) in the subcritical heat affetcted zone (SCHAZ) of all the DP and MS AHSS used in this work. The existence of this phenomena needs to be also evaluated in AHSS spot welds by using advanced characterization techniques such as nanoindentation and microscale mechanical testing.
- The impact of YPP on performance of spot welds needs further investigations, especially under dynamic and cyclic loading relevant to fatigue behavior.
- Numerous studies have shown the dependence of the material behavior (including YPP) and damage model (fracture strain) to the stress state (stress triaxiality), Lode angle, and strain rate. Therefore, the material and damage models need improvement by including above factors in the future studies.
- With the levels of yield stress and ultimate tensile strength in both the SCHAZ and ICHAZ, techniques to improve the mechanical performance of this region needs to be employed. Post-welding heat treatments, post-weld straining of weak regions (here ICHAZ), and alloy design can be of helpful techniques in this manner.
- Alloy design can be used by modifying the chemical composition to reduce the Ae_3 and Ae_1 so that the distance between spot welds centerline and ICHAZ/SCHAZ regions increases resulting an increase in the welds performance. This technique could be used in DP spot welds as HAZ softening has showed to reduce the performeance in these steels. (HAZ softenign showed to improve the performance of MS steels).
- Since the nugget diameters below the criotical size (around 6 mm) leads to interfacial failure with low energy absorption and poor crashworthiness

and not desired in the automotive industry, techiques to improve the welds toughness, such as tempering of all the regions above the Ae_3 can be beneficial. This can increase the strength and global extension of the spot welded samples with higher impact on higher grades (with higher carbon content in the martensite that resulted in lower ductility in UCHAZ of weld).

Bibliography

[1] R. Kuziak, R. Kawalla, and S. Waengler, "Advanced high strength steels for automotive industry," *Archives of Civil and Mechanical Engineering,* vol. 8, no. 2, pp. 103-117, 2008.
[2] S. Keeler and M. Kimchi, "Advanced High-Strength Steels Application Guaidelines," *www.worldautosteel.org,* 2014.
[3] N. Yamauchi, T. Taka, K. Kunishige, and N. Nagao, "Softening Behavior in Heat-Affected Zone of Flash Butt Welded Hot Rolled Dual Phase Steel (HSLA Having Low Yield Ratio. 7)," 1982, vol. 22, pp. B107-B107: IRON STEEL INST JAPAN KEIDANREN KAIKAN 9-4 OTEMACHI 1-CHOME CHIYODA-KU, TOKYO 100, JAPAN.
[4] K. Kunishige, N. Yamauchi, T. Taka, and N. Nagao, "Softening in weld heat affected zone of dual phase steel sheet for automotive wheel rim," SAE Technical Paper1983 1983, Available: http://papers.sae.org/830632/, Accessed on: 2015/05/01/06:40:00.
[5] H. Ghassemi-Armaki, S. Bhat, S. Kelley, and S. Sadagopan, "Quasi-Static Spot Weld Strength of Advanced High-Strength Sheet Steels This study highlights the spot weld strength in tension-shear and cross-tension loading modes, and HAZ strength as a function of base metal strength, in sheet steels," *WELDING JOURNAL,* vol. 96, no. 3, 2017.
[6] P. Maugis, W. D. Hopfe, J. E. Morral, and J. S. Kirkaldy, "Multiple interface velocity solutions for ternary biphase infinite diffusion couples," (in English), *Acta Materialia,* vol. 45, no. 5, pp. 1941-1954, May 1997.
[7] D. Bhattacharya, "Developments in advanced high strength steels," 2005, pp. 70-73.
[8] V. H. B. Hernandez, S. K. Panda, M. L. Kuntz, and Y. Zhou, "Nanoindentation and microstructure analysis of resistance spot welded dual phase steel," *Materials Letters,* vol. 64, no. 2, pp. 207-210, 2010 2010.
[9] T. Waterschoot, K. Verbeken, and B. C. De Cooman, "Tempering kinetics of the martensitic phase in DP steel," *ISIJ international,* vol. 46, no. 1, pp. 138-146, 2006 2006.
[10] R. A. Grange, C. R. Hribal, and L. F. Porter, "Hardness of tempered martensite in carbon and low-alloy steels," *Metallurgical Transactions A,* vol. 8, no. 11, pp. 1775-1785, 1977 1977.
[11] R. N. Caron and G. Krauss, "Tempering of Fe-C Lath Martensite," (in English), *Metallurgical Transactions,* vol. 3, no. 9, pp. 2381-&, 1972.
[12] E. Biro, J. R. McDermid, J. D. Embury, and Y. Zhou, "Softening Kinetics in the Subcritical Heat-Affected Zone of Dual-Phase Steel Welds," *Metallurgical and Materials Transactions A,* vol. 41, no. 9, pp. 2348-2356, 2010.
[13] V. H. Baltazar Hernandez, S. K. Panda, Y. Okita, and N. Y. Zhou, "A study on heat affected zone softening in resistance spot welded dual phase

steel by nanoindentation," *Journal of Materials Science,* vol. 45, no. 6, pp. 1638-1647, 2009.
[14] V. H. Baltazar Hernandez, S. S. Nayak, and Y. Zhou, "Tempering of Martensite in Dual-Phase Steels and Its Effects on Softening Behavior," *Metallurgical and Materials Transactions A,* vol. 42, no. 10, pp. 3115-3129, 2011.
[15] Y. Tomita, "Effect of morphology of second-phase martensite on tensile properties of Fe-0.1 C dual phase steels," *Journal of Materials science,* vol. 25, no. 12, pp. 5179-5184, 1990 1990.
[16] E. Biro, "Heat-Affected Zone Softening Kinetics in Dual-Phase and Martensitic Steels," 2014 2014.
[17] H. Rezayat, S. S. Babu, and H. Ghassemi-Armaki, "Effects of Heat Affected Zone Softening Extent on Strength of Advanced High Strength Steels Resistance Spot Weld," in *Trends in Welding Research, Proceedings of the 10th International Conference*, Tokyo, Japan, 2016.
[18] M. Xia, E. Biro, Z. Tian, and Y. N. Zhou, "Effects of heat input and martensite on HAZ softening in laser welding of dual phase steels," *ISIJ international,* vol. 48, no. 6, pp. 809-814, 2008 2008.
[19] H. Ghassemi-Armaki, E. Biro, and S. Sadagopan, "Advanced Characterization of HAZ Softening of AHSS for Crash Modeling," (in English), *Isij International,* vol. 57, no. 8, pp. 1451-1460, 2017.
[20] M. I. Khan, M. L. Kuntz, E. Biro, and Y. Zhou, "Microstructure and Mechanical Properties of Resistance Spot Welded Advanced High Strength Steels," *Materials Transactions,* vol. 49, no. 7, pp. 1629-1637, 2008.
[21] S. Dancette, V. Massardier-Jourdan, D. Fabrègue, J. Merlin, T. Dupuy, and M. Bouzekri, "HAZ microstructures and local mechanical properties of high strength steels resistance spot welds," *ISIJ international,* vol. 51, no. 1, pp. 99-107, 2011 2011.
[22] Y. Wang, S. Denis, B. Appolaire, and P. Archambault, "Modelling of precipitation of carbides during tempering of martensite," in *Journal de Physique IV (Proceedings)*, 2004, vol. 120, pp. 103-110: EDP sciences.
[23] E. Biro *et al.*, "Predicting Transient Softening in the Sub-Critical Heat-Affected Zone of Dual-Phase and Martensitic Steel Welds," *ISIJ International,* vol. 53, no. 1, pp. 110-118, 2013.
[24] G. R. Speich, "Physical metallurgy of dual-phase steels," *Fundamentals of dual-phase steels,* pp. 3-45, 1981 1981.
[25] H. K. D. H. Bhadeshia, "Martensite and Bainite in Steels : Transformation Mechanism &

Mechanical Properties," *Le Journal de Physique IV,* vol. 07, no. C5, pp. C5-367-C5-376, 1997.
[26] W. F. Smith, "Structure and properties of engineering alloys," 1993 1993.

[27] D. A. Porter, K. E. Easterling, and M. Sherif, *Phase Transformations in Metals and Alloys, (Revised Reprint)*. CRC press, 2011.
[28] D. Rosenthal, "Mathematical theory of heat distribution during welding and cutting," *Welding journal,* vol. 20, no. 5, pp. 220s-234s, 1941 1941.
[29] D. Rosenthal, "The theory of moving sources of heat and its application to metal treatments," 1946: ASME.
[30] D. C. Saha, S. S. Nayak, E. Biro, A. P. Gerlich, and Y. Zhou, "Mechanism of Secondary Hardening in Rapid Tempering of Dual-Phase Steel," *Metallurgical and Materials Transactions A,* vol. 45, no. 13, pp. 6153-6162, 2014 2014.
[31] J. W. Christian, *The theory of transformations in metals and alloys (part I+ II)*. Newnes, 2002.
[32] W. A. Johnson and R. F. Mehl, "Reaction kinetics in processes of nucleation and growth," *Trans. Aime,* vol. 135, no. 8, pp. 396-415, 1939 1939.
[33] M. Avrami, "Kinetics of phase change. I General theory," *The Journal of Chemical Physics,* vol. 7, no. 12, pp. 1103-1112, 1939 1939.
[34] M. Avrami, "Kinetics of phase change. II transformation-time relations for random distribution of nuclei," *The Journal of Chemical Physics,* vol. 8, no. 2, pp. 212-224, 1940 1940.
[35] W. S. Owen, "The effect of silicon on the kinetics of tempering," *Transactions of the American Society for Metals,* vol. 46, pp. 812-829, 1954 1954.
[36] Y. Tomita, "Evaluation of rate constants in tempering reaction of hardened steels from dilatometric data on continuous heating at controlled rates," *Materials science and technology,* vol. 4, no. 11, pp. 977-983, 1988 1988.
[37] M. Takahashi and H. Bhadeshia, "Model for transition from upper to lower bainite," *Materials Science and Technology,* vol. 6, no. 7, pp. 592-603, 1990 1990.
[38] Y. J. Chao, "Ultimate Strength and Failure Mechanism of Resistance Spot Weld Subjected to Tensile, Shear, or Combined Tensile/Shear Loads," *Journal of Engineering Materials and Technology,* vol. 125, no. 2, p. 125, 2003.
[39] Y. J. Chao, "Failure mode of spot welds: interfacial versus pullout," *Science and technology of welding and joining,* vol. 8, no. 2, pp. 133-137, 2003 2003.
[40] S. Dancette, D. Fabrègue, V. Massardier, J. Merlin, T. Dupuy, and M. Bouzekri, "Experimental and modeling investigation of the failure resistance of Advanced High Strength Steels spot welds," *Engineering Fracture Mechanics,* vol. 78, no. 10, pp. 2259-2272, 2011.
[41] S. Dancette, D. Fabrègue, V. Massardier, J. Merlin, T. Dupuy, and M. Bouzekri, "Investigation of the Tensile Shear fracture of Advanced High

Strength Steel spot welds," *Engineering Failure Analysis,* vol. 25, pp. 112-122, 2012.
[42] S. Dancette, D. Fabregue, R. Estevez, V. Massardier, T. Dupuy, and M. Bouzekri, "A finite element model for the prediction of Advanced High Strength Steel spot welds fracture," *Engineering Fracture Mechanics,* vol. 87, pp. 48-61, 2012.
[43] Y. P. Yang, S. S. Babu, F. Orth, and W. Peterson, "Integrated computational model to predict mechanical behaviour of spot weld," *Science and Technology of Welding & Joining,* vol. 13, no. 3, pp. 232-239, 2008 2008.
[44] H. Ghassemi-Armaki, P. Chen, S. Bhat, S. Sadagopan, S. Kumar, and A. Bower, "Microscale-calibrated modeling of the deformation response of low-carbon martensite," *Acta Materialia,* vol. 61, no. 10, pp. 3640-3652, 2013.
[45] P. Chen, H. Ghassemi-Armaki, S. Kumar, A. Bower, S. Bhat, and S. Sadagopan, "Microscale-calibrated modeling of the deformation response of dual-phase steels," *Acta Materialia,* vol. 65, pp. 133-149, 2014.
[46] M. Pouranvari and P. Marashi, "Failure behaviour of resistance spot welded low carbon steel in tensile-shear and coach-peel tests: A comparative study," *Metallurgical Journal of Metallurgy,* vol. 15, no. 3, pp. 149-157, 2009 2009.
[47] M. Pouranvari and S. P. H. Marashi, "Failure mode transition in AHSS resistance spot welds. Part I. Controlling factors," *Materials Science and Engineering: A,* vol. 528, no. 29, pp. 8337-8343, 2011 2011.
[48] C. M. Tamarelli, "The Evolving Use of Advanced High-Strength Steels for Automotive Applications," *Steel Market Development Institute, Michigan,* 2011 2011.
[49] J.-O. Sperle and K. Olsson, "High strength and ultra high strength steels for weight reduction in structural and safety-related applications," 1996, vol. 1, pp. 115-125.
[50] H. G. Koenigsberger, "Philip-Ii of Spain - Pierson,P," (in English), *American Historical Review,* vol. 82, no. 4, pp. 946-948, 1977.
[51] *Standard Guide for Preparation of Metallographic Specimens*, 2011.
[52] H. K. D. H. Bhadeshia, "Martensite and Bainite in Steels : Transformation Mechanism & Mechanical Properties," *Le Journal de Physique IV,* vol. 07, no. C5, pp. C5-367-C5-376, 1997.
[53] B. N. Ranganathan and H. E. Grenga, "Field-Ion Microscope Investigations of Fine Structures in as-Quenched and Tempered Ferrous Martensite," (in English), *Scripta Metallurgica,* vol. 7, no. 1, pp. 69-71, 1973.
[54] G. Krauss and W. Pitsch, "Fine Structure and Habit Planes of Martensite in an Iron-33 Wt (Nickel Single Crystal," (in English), *Journal of Metals,* vol. 17, no. 9, pp. 1060-&, 1965.

[55] G. Krauss and T. A. Balliett, "Fine structure and the early stages of tempering in the martensite of an Fe-1.22 C alloy," *Metallurgical Transactions A,* journal article vol. 7, no. 2, pp. 318-320, February 01 1976.
[56] G. R. Speich and R. L. Miller, "Tempering of Ferrite-Martensite Steels," (in English), *Journal of Metals,* vol. 32, no. 12, pp. 45-46, 1980.
[57] G. Krauss, "Tempering of Lath Martensite in Low and Medium Carbon Steels: Assessment and Challenges," (in English), *Steel Research International,* vol. 88, no. 10, Oct 2017.
[58] S. S. Babu, K. Hono, and T. Sakurai, "Atom probe field ion microscopy study of the partitioning of substitutional elements during tempering of a low-alloy steel martensite," (in English), *Metallurgical and Materials Transactions A,* vol. 25, no. 3, pp. 499-508, 1994/03/01 1994.
[59] Y. P. Yang, S. S. Babu, F. Orth, and W. Peterson, "Integrated computational model to predict mechanical behaviour of spot weld," (in English), *Science and Technology of Welding and Joining,* vol. 13, no. 3, pp. 232-239, May 2008.
[60] J. M. Vitek and S. S. Babu, "Multiscale characterisation of weldments," (in English), *Science and Technology of Welding and Joining,* vol. 16, no. 1, pp. 3-11, Jan 2011.
[61] G. R. Speich, "Tempering of Low-Carbon Martensite," (in English), *Transactions of the Metallurgical Society of Aime,* vol. 245, no. 12, pp. 2553-&, 1969.
[62] S. Morito, Y. Adachi, and T. Ohba, "Morphology and Crystallography of Sub-Blocks in Ultra-Low Carbon Lath Martensite Steel," (in English), *Materials Transactions,* vol. 50, no. 8, pp. 1919-1923, Aug 2009.
[63] E. Biro, J. R. McDermid, S. Vignier, and Y. Norman Zhou, "Decoupling of the softening processes during rapid tempering of a martensitic steel," *Materials Science and Engineering: A,* vol. 615, no. 0, pp. 395-404, 10/6/ 2014.
[64] D. C. Saha, E. Biro, A. P. Gerlich, and N. Y. Zhou, "Fusion zone microstructure evolution of fiber laser welded press-hardened steels," (in English), *Scripta Materialia,* vol. 121, pp. 18-22, Aug 2016.
[65] G. Krauss and T. A. Balliett, "Fine-Structure and Early Stages of Tempering in Martensite of an Fe 1.22 C Alloy," (in English), *Metallurgical Transactions a-Physical Metallurgy and Materials Science,* vol. 7, no. 2, pp. 318-320, 1976.
[66] J. H. Hollomon and L. D. Jaffe, "Time-Temperature Relations in Tempering Steel," (in English), *Transactions of the American Institute of Mining and Metallurgical Engineers,* vol. 162, pp. 223-249, 1945.
[67] F. Ziaebrahimi and G. Krauss, "The Evaluation of Tempered Martensite Embrittlement in 4130-Steel by Instrumented Charpy V-Notch Testing," (in

English), *Metallurgical Transactions a-Physical Metallurgy and Materials Science,* vol. 14, no. 6, pp. 1109-1119, 1983.
[68] E. J. Mittemeher, L. Cheng, P. J. Van der Schaaf, C. M. Brakman, and B. M. Korevaar, "Analysis of nonisothermal transformation kinetics; tempering of iron-carbon and iron-nitrogen martensites," *Metallurgical Transactions A,* vol. 19, no. 4, pp. 925-932, 1988 1988.
[69] L. R. C. Malheiros, E. A. P. Rodriguez, and A. Arlazarov, "Mechanical behavior of tempered martensite: Characterization and modeling," (in English), *Materials Science and Engineering a-Structural Materials Properties Microstructure and Processing,* vol. 706, pp. 38-47, Oct 26 2017.
[70] M. Li *et al.*, "Influence of material inhomogeneity on the mechanical response of a tempered martensite steel," (in English), *Proceedings of the Institution of Mechanical Engineers Part L-Journal of Materials-Design and Applications,* vol. 231, no. 1-2, pp. 14-22, Feb-Mar 2017.
[71] H. K. D. H. Bhadeshia and R. W. K. Honeycombe, "Tempering of Martensite," (in English), *Steels: Microstructure and Properties, 4th Edition,* pp. 237-270, 2017.
[72] D. C. Saha, E. Biro, A. P. Gerlich, and Y. Zhou, "Effects of tempering mode on the structural changes of martensite," (in English), *Materials Science and Engineering a-Structural Materials Properties Microstructure and Processing,* vol. 673, pp. 467-475, Sep 15 2016.
[73] Z. M. Shi *et al.*, "Study of tempering behavior of lath martensite using in situ neutron diffraction," (in English), *Materials Characterization,* vol. 107, pp. 29-32, Sep 2015.
[74] H. Li, S. Gao, Y. Tian, D. Terada, A. Shibata, and N. Tsuji, "Influence of tempering on mechanical properties of ferrite and martensite dual phase steel," (in English), *Materials Today-Proceedings,* vol. 2, pp. 667-671, 2015.
[75] K. Cvetkovski, J. Ahlstrom, and C. Persson, "Rapid thermomechanical tempering of iron-carbon martensite," (in English), *Materials Science and Technology,* vol. 30, no. 14, pp. 1832-1834, Nov 2014.
[76] S. Kang and S. J. Lee, "Prediction of Tempered Martensite Hardness Incorporating the Composition-Dependent Tempering Parameter in Low Alloy Steels," (in English), *Materials Transactions,* vol. 55, no. 7, pp. 1069-1072, Jul 2014.
[77] C. E. I. C. Ohlund, E. Schlangen, and S. E. Offerman, "The kinetics of softening and microstructure evolution of martensite in Fe-C-Mn steel during tempering at 300 degrees C," (in English), *Materials Science and Engineering a-Structural Materials Properties Microstructure and Processing,* vol. 560, pp. 351-357, Jan 10 2013.
[78] L. Sun, Z. Y. Zhao, X. Z. Yang, and R. D. Xue, "Effect of Tempering Process on Residual Stress in Hot Rolled Low Carbon Martensite High-

Strength Steel Strip," (in English), *Material Design, Processing and Applications, Parts 1-4,* vol. 690-693, pp. 222-+, 2013.
[79] A. Di Schino, L. Alleva, and M. Guagnelli, "Microstructure evolution during quenching and tempering of martensite in a medium C steel," (in English), *Recrystallization and Grain Growth Iv,* vol. 715-716, pp. 860-865, 2012.
[80] V. H. B. Hernandez, S. S. Nayak, and Y. Zhou, "Tempering of Martensite in Dual-Phase Steels and Its Effects on Softening Behavior," (in English), *Metallurgical and Materials Transactions a-Physical Metallurgy and Materials Science,* vol. 42a, no. 10, pp. 3115-3129, Oct 2011.
[81] G. R. Speich, "Tempering of Low-Carbon Martensite," (in English), *Journal of Metals,* vol. 20, no. 8, pp. A23-&, 1968.
[82] J. Mazur, "Structure of Tempered Martensite," (in English), *Nature,* vol. 164, no. 4162, pp. 230-231, 1949.
[83] W. J. Wrazej, "The Structure of Tempered Martensite," (in English), *Journal of the Iron and Steel Institute,* vol. 154, no. 2, pp. P147-&, 1946.
[84] A. Michel, "The Structure of Tempered Martensite," (in English), *Journal of the Iron and Steel Institute,* vol. 154, no. 2, pp. P152-P153, 1946.
[85] A. H. Cottrell and B. A. Bilby, "Dislocation Theory of Yielding and Strain Ageing of Iron," (in English), *Proceedings of the Physical Society of London Section A,* vol. 62, no. 349, pp. 49-62, 1949.
[86] E. Hall, *Yield point phenomena in metals and alloys*. Springer Science & Business Media, 2012.
[87] T. Waterschoot, A. K. De, S. Vandeputte, and B. C. De Cooman, "Static strain aging phenomena in cold-rolled dual-phase steels," (in English), *Metallurgical and Materials Transactions a-Physical Metallurgy and Materials Science,* vol. 34a, no. 3, pp. 781-791, Mar 2003.
[88] T. H. Ahn, C. S. Oh, K. Lee, E. P. George, and H. N. Han, "Relationship between yield point phenomena and the nanoindentation pop-in behavior of steel," (in English), *Journal of Materials Research,* vol. 27, no. 1, pp. 39-44, Jan 2012.
[89] H. Conrad and G. Schoeck, "Cottrell Locking and the Flow Stress in Iron," (in English), *Acta Metallurgica,* vol. 8, no. 11, pp. 791-796, 1960.
[90] W. W. Gerberich, S. Venkataraman, J. Nelson, H. Huang, E. Lilleodden, and W. Bonin, "Yield point phenomena and dislocation velocities underneath indentations into BCC crystals," (in English), *Thin Films: Stresses and Mechanical Properties V,* vol. 356, pp. 629-644, 1995.
[91] G. T. Hahn, "Model for Yielding with Special Reference to Yield-Point Phenomena of Iron and Related Bcc Metals," (in English), *Acta Metallurgica,* vol. 10, no. Aug, pp. 727-&, 1962.
[92] G. T. Hahn, "A model for yielding with special reference to the yield-point phenomena of iron and related bcc metals," *Acta metallurgica,* vol. 10, no. 8, pp. 727-738, 1962.

[93] N. Tsuchida, Y. Tomota, K. Nagai, and K. Fukaura, "A simple relationship between Luders elongation and work-hardening rate at lower yield stress," (in English), *Scripta Materialia,* vol. 54, no. 1, pp. 57-60, Jan 2006.
[94] T. L. Russell, D. S. Wood, and D. S. Clark, "The Influence of Grain Size on the Yield Phenomenon in Steel," (in English), *Acta Metallurgica,* vol. 9, no. 12, pp. 1054-1063, 1961.
[95] J. Winlock, "The Influence of the Rate of Deformation on the Tensile Properties of Some Plain Carbon Sheet Steels," (in English), *Transactions of the American Institute of Mining and Metallurgical Engineers,* vol. 197, no. 6, pp. 797-803, 1953.
[96] J. F. Hallai and S. Kyriakides, "Underlying material response for Luders-like instabilities," (in English), *International Journal of Plasticity,* vol. 47, pp. 1-12, Aug 2013.
[97] G. Piobert, pp. - 552.
[98] D. Johnson, M. Edwards, and P. Chard-Tuckey, "Microstructural effects on the magnitude of Lüders strains in a low alloy steel," *Materials Science and Engineering: A,* vol. 625, pp. 36-45, 2015.
[99] R. Schwab and V. Ruff, "On the nature of the yield point phenomenon," (in English), *Acta Materialia,* vol. 61, no. 5, pp. 1798-1808, Mar 2013.
[100] G. Van Rooyen, "The stress and strain distribution in a propagating Lüders front accompanying the yield-point phenomenon in iron," *Materials Science and Engineering,* vol. 3, no. 2, pp. 105-117, 1968.
[101] F. Yoshida, Y. Kaneda, and S. Yamamoto, "A plasticity model describing yield-point phenomena of steels and its application to FE simulation of temper rolling," (in English), *International Journal of Plasticity,* vol. 24, no. 10, pp. 1792-1818, Oct 2008.
[102] M. Maziere and S. Forest, "Strain gradient plasticity modeling and finite element simulation of Luders band formation and propagation," (in English), *Continuum Mechanics and Thermodynamics,* vol. 27, no. 1-2, pp. 83-104, Jan 2015.
[103] J. F. Hallai and S. Kyriakides, "On the effect of Luders bands on the bending of steel tubes. Part II: Analysis," (in English), *International Journal of Solids and Structures,* vol. 48, no. 24, pp. 3285-3298, Dec 1 2011.
[104] J. F. Hallai and S. Kyriakides, "Bending Capacity of Tubes with Luders Bands: Influence of Geometric and Material Parameters," (in English), *Proceedings of the Asme 31st International Conference on Ocean, Offshore and Artic Engineering, Vol 3,* pp. 507-512, 2012.
[105] R. Camsonne, M. A. Moulin, C. Crouzel, A. Syrota, M. Maziere, and D. Comar, "C-11 Labeling of Pk11195 and Visualization of Peripheral Receptors of Benzodiazepines by Positron-Emission Tomography," (in French), *Journal De Pharmacologie,* vol. 17, no. 3, pp. 383-383, Jul-Sep 1986.

[106] T. J. R. Hughes, *The Finite Element Method: Linear Static and Dynamic Finite Element Analysis*. Dover Publications, 2012.
[107] J. S. Sun, K. H. Lee, and H. P. Lee, "Comparison of implicit and explicit finite element methods for dynamic problems," *Journal of Materials Processing Technology,* vol. 105, no. 1, pp. 110-118, 2000/09/07/ 2000.
[108] A. M. Prior, "Applications of Implicit and Explicit Finite-Element Techniques to Metal-Forming," (in English), *Journal of Materials Processing Technology,* vol. 45, no. 1-4, pp. 649-656, Sep 1994.
[109] X. Hu, R. H. Wagoner, G. S. Daehn, and S. Ghosh, "Comparison of explicit and implicit finite element methods in the quasistatic simulation of uniaxial tension," *Communications in Numerical Methods in Engineering,* vol. 10, no. 12, pp. 993-1003, 1994.
[110] "AWS D8.9M. Test methods for evaluating the resistance spot welding behavior of automotive sheet steel materials, third ed. American Welding Society (AWS), Miami, Fl, USA, 2012."
[111] M. R. Wenman and P. R. Chard-Tuckey, "Modelling and experimental characterisation of the Luders strain in complex loaded ferritic steel compact tension specimens," (in English), *International Journal of Plasticity,* vol. 26, no. 7, pp. 1013-1028, Jul 2010.
[112] C. C. Tasan *et al.*, "Integrated experimental–simulation analysis of stress and strain partitioning in multiphase alloys," *Acta Materialia,* vol. 81, no. 0, pp. 386-400, 12// 2014.
[113] C. C. Tasan, J. P. M. Hoefnagels, M. Diehl, D. Yan, F. Roters, and D. Raabe, "Strain localization and damage in dual phase steels investigated by coupled in-situ deformation experiments and crystal plasticity simulations," *International Journal of Plasticity,* vol. 63, no. 0, pp. 198-210, 12// 2014.

Vita

Hassan Rezayat was born in Iran. He obtained his Bachelor of Science degree in Welding Engineering in 2007. After several years of work in industry as Mechanical Design Engineer and Quality Control Engineer, he decided to further and diversify his education by pursuing a Doctor of Philosophy degree in Mechanical Engineering with focus on Welding and Additive Manufacturing. He graduated with a Master of Science degree in Mechanical Engineering in 2015 and a Doctor of Philosophy degree in Mechanical Engineering in 2019 from the University of Tennessee at Knoxville.